STRUCTURAL INSIGHTS INTO THE MECHANISMS OF MEMBRANE BINDING AND OLIGOMERIZATION OF A BACTERIAL PORE-FORMING TOXIN

A Dissertation

by

RAJESH RAMACHANDRAN

Submitted to the Office of Graduate Studies of
Texas A&M University
in partial fulfillment of the requirements for the degree of

DOCTOR OF PHILOSOPHY

December 2004

Major Subject: Biochemistry

STRUCTURAL INSIGHTS INTO THE MECHANISMS OF MEMBRANE BINDING AND OLIGOMERIZATION OF A BACTERIAL PORE-FORMING TOXIN

A Dissertation

by

RAJESH RAMACHANDRAN

Submitted to Texas A&M University
in partial fulfillment of the requirements
for the degree of

DOCTOR OF PHILOSOPHY

Approved as to style and content by:

Arthur E. Johnson
(Chair of Committee)

J. Martin Scholtz
(Member)

Michael Polymenis
(Member)

James C. Sacchettini
(Member)

Gregory D. Reinhart
(Head of Department)

December 2004

Major Subject: Biochemistry

ABSTRACT

Structural Insights into the Mechanisms of Membrane Binding and Oligomerization of a Bacterial Pore-forming Toxin. (December 2004)

Rajesh Ramachandran, B.S., University of Madras;

M.S., University of Madras

Chair of Advisory Committee: Dr. Arthur E. Johnson

Perfringolysin O (PFO), a cytolytic toxin from by the pathogenic bacterium *Clostridium perfringens*, perforates mammalian cell membranes by forming large aqueous pores. Secreted as water-soluble monomers, the toxin molecules bind to cholesterol-containing membranes, form large, circular oligomeric complexes on the membrane surface and then insert into the bilayer to create pores with diameters near 300 Å. Using multiple independent fluorescence techniques as primary tools, the mechanisms of PFO membrane binding and oligomerization have been identified.

Domain 4 (D4) of the protein interacts first with the membrane and is responsible for cholesterol recognition. Remarkably, only the short hydrophobic loops at the tip of the D4 β-sandwich are exposed to the bilayer interior, while the remainder of D4 projects from the membrane surface. Thus, a very limited interaction of D4 with the bilayer core appears to be sufficient to accomplish cholesterol recognition and initial PFO binding to the membrane.

Upon PFO membrane binding, a structural element in domain 3 (D3) of the molecule moves to expose the edge of a previously-hidden β-strand that forms the monomer-monomer interface. The β-strands that form the interface each contain a single aromatic residue, and these aromatics appear to stack to align the transmembrane β-hairpins of adjacent monomers in the proper register for insertion. Membrane-dependent structural rearrangements are thus required to initiate and regulate PFO oligomerization.

Fluorescence resonance energy transfer measurements reveal that the elongated toxin monomer arrives at the membrane in an 'end-on' orientation, with its long axis oriented nearly perpendicular to the plane of the membrane bilayer. This orientation is largely retained even after monomer association to form a prepore complex. In particular, the D3 polypeptide segments that form the transmembrane β-hairpins remain far above the membrane surface both at the membrane-bound monomer and prepore stages of pore formation. However, upon pore formation, the height of the oligomeric complex above the membrane surface is significantly reduced. The major topographical changes that occur during the prepore-to-pore transition of the PFO oligomer, therefore appears to result primarily from a collapsing of the extended domain 2 (D2) conformation in the monomer.

For my Mother.

ACKNOWLEDGMENTS

First, I would like thank my mentor Dr. Arthur E. Johnson for his valuable suggestions, insightful comments, and incisive criticisms. Although a very hard act to follow, his discipline, commitment and dedication to the relentless pursuit of knowledge are truly inspirational.

Very special thanks to Dr. Alejandro P. Heuck, my teacher, guide and friend, with whom I had the privilege to work and share ideas. His scathing but well-meaning criticisms on many an occasion has spurred me on to do my best.

I would like to thank members of my advisory committee, Drs. James C. Sacchettini, J. Martin Scholtz, Michael Polymenis, and former member Dr. Hagan Bayley for their constant support and words of encouragement.

Words fail me in expressing my heartfelt thanks to my dear friend, Gayathri Kalyanaraman, who stood by me and supported me through some trying times during the last few years. You are not only a great companion but also a wonderful human being.

I would also like to thank my colleagues past and present for their friendship and support.

Last, but not least, I would like to thank my parents back home in India, and also my brother for their love, support, and faith in me. I hope that I can live up to your dreams.

TABLE OF CONTENTS

Page

ABSTRACT iii

DEDICATION v

ACKNOWLEDGMENTS vi

TABLE OF CONTENTS vii

LIST OF FIGURES x

LIST OF TABLES xii

CHAPTER

I INTRODUCTION 1

- Bacterial protein toxins 2
- Pore-forming toxins (PFTs) 5
- *S. aureus* α-HL 9
- CDCs 10
- PFO structure 17
- Membrane-interacting regions of PFO 19
- Mechanism of CDC pore formation 25
- Pathway for CDC pore formation 27
- Unresolved issues and specific goals of this study 29

II EXPERIMENTAL PROCEDURES 31

- Construction of recombinant PFO (rPFO) derivatives 31
- Overexpression and purification of rPFO derivatives 33
- Fluorescent labeling of rPFO derivatives 36
- Preparation of liposomes 39
- Assay for pore formation 40
- Steady-state fluorescence spectroscopy 41
- Collisional quenching by iodide ions 42
- Quenching by spin-labeled phospholipids 43
- Time-resolved fluorescence spectroscopy and data analysis 45

CHAPTER Page

FRET parameters, measurements and data analysis 46
Calculation of acceptor density 46
Determination of quantum yield Q_D............................ 47
Determination of R_0 47
Steady-state anisotropy 50
Energy transfer measurements 51
Calculation of the distance of closest approach L........ 52
Chemical crosslinking and SDS-AGE 52

III MEMBRANE-ANCHORING MECHANISM OF PFO................. 54

Introduction 54
Results 56
Experimental approach... 56
D4 does not span the bilayer 58
Only the tip of D4 is exposed to the membrane core ... 60
D4 orientation and contacts.. 61
D4 topography in the membrane-inserted oligomer..... 65
Discussion 65
Role of D4 in pore formation 65

IV MECHANISM OF PFO OLIGOMERIZATION AND INTERSUBUNIT β-SHEET ALIGNMENT 70

Introduction 70
Results 73
Experimental rationale 73
β4 to β5 crosslinking inhibits oligomerization............ 75
Membrane binding alters conformation near β4 79
Loop flexibility is required for oligomerization........... 86
β1 of one monomer is adjacent to β4 of its neighbor... 86
Aromatic residues align intersubunit β-strands........... 91
Discussion 100
Mechanism of PFO oligomerization and intersubunit β-sheet alignment 100

V TOPOGRAPHY OF MEMBRANE-BOUND PFO AT DIFFERENT STAGES OF PORE FORMATION 106

Introduction 106
Results 110

CHAPTER Page

Experimental rationale and design 110
PFO derivatives trapped at different stages of pore formation 113
Spectral properties of BODIPY-labeled rPFO derivatives.. 114
Topography of PFO as a membrane-bound monomer. 115
Topography of PFO in the prepore complex............... 117
Topography of PFO in the pore complex.................... 118
Dye orientation (κ^2) effects and uncertainties in L 120
Discussion 122

VI SUMMARY 130

REFERENCES 133

APPENDIX SUPPORTING FIGURES 142

VITA 148

LIST OF FIGURES

FIGURE Page

1 Crystal structure of the *S. aureus* α-HL heptamer 11

2 Comparison of the structures of LukF and α-HL................................ 12

3 Primary structures of the sequenced CDCs.. 14

4 Crystal structure of monomeric PFO 18

5 Origin of the transmembrane segments of PFO................................. 22

6 Top view of the pathway of pore formation by PFO 28

7 Structures of fluorescent reagents and phospholipid.......................... 37

8 Analysis of iodide ion quenching by the Stern-Volmer equation........ 44

9 Spectral overlap of BODIPY and Rh-PE... 49

10 D4 probe locations 57

11 D4 probe environments... 59

12 D4 topography in the membrane-inserted oligomer 66

13 PFO structural elements and mutations.. 72

14 Conformational changes in D3... 74

15 Effect of β4-β5 disulfide-locking on pore formation.......................... 76

16 Effect of β4-β5 disulfide-locking on membrane binding and TMH insertion... 78

17 Effect of β4-β5 disulfide-locking on oligomerization 80

18 D4-membrane interaction triggers a conformational change around β4 in D3.. 84

FIGURE Page

19 Effect of β4-β5 disulfide-locking on the conformational change around β4 85

20 Mutation of glycines at the end of β4 blocks oligomerization 87

21 Pyrene excimer formation detects β1 and β4 proximity in neighboring PFO 90

22 Excimer formation in the presence of the β4-β5 disulfide lock 92

23 F318A mutation blocks pore formation but not membrane binding 93

24 F318A mutation blocks TMH insertion but not prepore formation 95

25 Alignment of aromatic residues in β1 and β4 is critical for pore formation 98

26 Analysis of mutants i through iv 99

27 Mechanism of oligomerization and intermolecular β-sheet formation 102

28 PFO dimensions and locations of mutations 107

29 Conceivable orientations of PFO on the membrane surface 109

30 Dependence of energy transfer upon acceptor density 116

31 Model of FRET-detected changes in PFO topography 128

32 Pore formation by NBD-labeled D4 mutants 143

33 Pore-formation assay for rPFO(V322C-NBD) and rPFO(G324V G325V) 144

34 Trp emission intensity time traces for rPFO mutants 145

35 Characterization of pyrene-labeled rPFO mutants 146

36 Pyrene-excimer formation is dependent on the proximity of pyrenes . 147

LIST OF TABLES

TABLE Page

1 NBD exposure to the membrane interior 62

2 NBD exposure to the aqueous milieu.. 63

3 Fluorescence lifetimes of rPFO(V322C-NBD)................................... 82

4 Fluorescence lifetimes of rPFO(F318A A215C-NBD)........................ 96

5 Distance of closest approach determined by FRET 121

CHAPTER I

INTRODUCTION

Clostridium perfringens, the anaerobic bacterium that causes gas gangrene in humans, secretes an arsenal of tissue-damaging toxins into its host to elicit the various lesions and symptoms associated with the disease (Stevens and Bryant, 1999). The toxin primarily responsible is the ‘α-toxin’ that exhibits degradative enzymatic activities towards the mammalian plasma membrane leading to its disruption and permeabilization (Titball, 1999). The pore-forming perfringolysin O (PFO; also known as Θ-toxin) is another membrane-damaging toxin that plays a secondary, yet critical, role in establishing clostridial pathogenesis (Stevens and Bryant, 1999; Petit et al., 1999). In concert with the α-toxin, PFO contributes to the impairment of the host immune response by causing necrosis of the vasculature at the site of infection. PFO belongs to a large family of protein toxins called the ‘cholesterol-dependent cytolysins’ (CDCs) that form pores only in membranes that contain cholesterol (Alouf, 1999; Tweten et al., 2001).

The research in the following dissertation examines and elucidates mechanisms by which PFO anchors itself to a cholesterol-containing membrane and forms ring-like oligomeric complexes that ultimately insert into the membrane bilayer to create large aqueous pores. Beginning with an introduction, each successive chapter will address the molecular details of a specific step in the pore formation process, followed by an in

---

This dissertation follows the style and format of Cell.

depth discussion of the new findings and their impact on our current understanding of CDC pore formation.

Bacterial protein toxins

An evolutionary outcome of the host-pathogen relationship between higher eukaryotes and bacteria is the development of sophisticated virulence factors or toxins by the pathogen that give it a selective advantage over the host. These toxins are most often protein molecules that are designed specifically to either kill the host cell by lysing it or subvert host cellular processes such as cell signaling, intracellular protein sorting, and cytoskeletal assembly in order to create an ecological niche for the pathogenic bacteria to derive nutrients, effectively resist the host immune response, and thereby exert their virulence. Pathogenicity leads, in nearly all cases, to death. Thus, these molecules are, as the name implies, 'toxic' to the host. This section will provide readers a brief introduction to the rapidly expanding field of toxin biology or 'toxinology' and its impact on human disease and health. For comprehensive reviews on bacterial protein toxins, I direct the reader to the following resource – The comprehensive source book of bacterial protein toxins (Alouf and Freer, 1999).

Since the isolation of the diphtheria toxin by Roux and Yersin in 1888, microbial toxins have been recognized as the molecular effectors of infectious disease (Schmitt et al., 1999). In the 1930s, diphtheria toxin was purified to sufficient quantities and was ascertained to be a protein. However, due to the limited knowledge on the nature of proteins then, fundamental concepts regarding protein toxins and their mode of action were not firmly grounded. Not until after World War II, when basic cellular processes and their molecular bases were beginning to be unraveled, did scientific interest turn towards toxins and their role in altering host metabolism. The rapid advancement of biological sciences in the 60s and 70s saw seminal discoveries being made in toxin biology. In fact, debilitating diseases caused by *Vibrio cholerae* (cholera), *Bacillus anthracis* (anthrax), *Bordetella pertussis* (whooping cough), *Clostridium perfringens* (gas gangrene), *Clostridium botulinum* (botulism) and *Clostridium tetani* (tetanus) were all shown to be related to the protein toxins produced by these pathogenic bacteria. With these discoveries came the application of inactivated toxins (toxoids) as vaccines to battle the invasive bacteria and their disease.

With a few exceptions (e.g. *Listeria monocytogenes*), growth of pathogenic bacteria within the host is extracellular. The protein toxins elicited by these bacteria are thus often secreted as soluble, diffusible moieties into the extracellular milieu of the host and in some cases are released by lysis of the bacterial cell (e.g. pneumolysin from *Streptococcus pneumoniae*). Hence, these toxins are referred to as 'exotoxins', as opposed to 'endotoxins' that are integral components of the outer membrane of Gram-negative bacteria (e.g. lipopolysaccharides or LPS) and are usually liberated during bacterial lysis (Alouf, 1999).

Although secreted into the extracellular milieu, a vast majority of bacterial exotoxins exert their deleterious effects by targeting molecules that are located within the host cytosol. For instance, toxins such as the *Vibrio cholerae* cholera toxin and the *Bordetella pertussis* pertussis toxin catalyze the ADP-ribosylation of the G_s subunit of heterotrimeric G proteins in the host cytosol that eventually leads to the disruption of host signal transduction pathways (Hirst, 1999; Locht and Antoine, 1999). Similarly, the *Corynebacterium diphtheriae* diphtheria toxin interferes with host protein synthesis by ADP-ribosylating the EF-2 elongation factor (Choe et al., 1992).

How do toxins that act intracellularly move across the physical barrier posed by the host cell membrane? Most protein toxins that act on intracellular targets consist of two components: an 'A' or 'active' component that is responsible for the enzymatic activity of the toxin in the host cytosol, and a 'B' or 'binding' component that is involved in the binding of the toxin to a specific receptor on the host cell membrane and, by various mechanisms, in the translocation of the A moiety into the host cytosol. These toxins are referred to as 'A-B' toxins; the A and B components may or may not be encoded in a single polypeptide chain (Lacy and Stevens, 1998; Collier and Young, 2003). For example, in the case of tripartite anthrax toxin, the lethal (LF) and the edema (EF) factors are the A components, while the protective antigen (PA) moiety constitutes the B component that forms a transmembrane pore through which the noncovalently-associated A component is translocated into the host cytosol (for a review, see Collier and Young, 2003). This translocation takes place through the membrane of the acidified endocytic vesicle after internalization of the A-B complex by receptor-mediated endocytosis.

On the other hand, in the diphtheria toxin, both the A and B moieties are present in a single polypeptide chain (Choe et al., 1992). The C-terminal portion of the B moiety associates with a specific transmembrane receptor on the host cell membrane (identified to be a heparin-binding protein; Naglich et al., 1992) and triggers the internalization of the complex by receptor-mediated endocytosis. Acidification of the endocytic vesicle unfolds the toxin polypeptide and promotes the insertion of the highly hydrophobic N-terminal portion of the B moiety into the endocytic vesicle membrane. This somehow facilitates the translocation of the N-terminal A moiety to the cytosolic side. Then, disulfide-bond reduction and proteolytic cleavage release the A chain into the cytosol, where it refolds and enzymatically ADP-ribosylates elongation factor-2 (EF-2) to inhibit protein synthesis.

Thus, membrane-inserting, pore-forming toxin components constitute a portal for the entry of intracellularly-acting toxin moieties into the host cytosol. Since my study involves a pore-forming toxin, I will curtail my general description of bacterial toxins here and focus primarily on pore-forming toxins.

Pore-forming toxins (PFTs)

Among the several different classes of protein toxins produced by pathogenic bacteria, a fair number of them (~ 35% of the 325 protein toxins identified so far) act by damaging host cell membranes (Alouf, 2001). Membrane damage constitutes any process that disrupts the integrity or the permeability barrier of the membrane bilayer. These toxins were first identified and characterized by virtue of their lytic activity towards mammalian red blood cells, earning them the name ‘hemolysins’. However, later studies showed that these toxins are active on a variety of cell types. Hence, they were rechristened as ‘cytolysins’ or ‘cytolytic toxins’ to accurately represent their mode of action (Alouf, 2001).

Membrane-damaging toxins can be organized into three main types: those that exhibit enzymatic activities towards the host cell membrane such as *C. perfringens* α-toxin that exhibits metal ion-dependent phospholipase C and sphingomyelinase activities (Titball, 1999); those that solubilize the membrane via detergent- or surfactant-like activities, such as the *S. aureus* δ toxin (Dufourcq et al., 1999); and the PFTs that form sizeable holes in the host cell membrane and thereby surmount the permeability barrier conferred by it (Alouf, 2001). Action of these membrane-damaging toxins results in the rapid influx of water into the host cell, cell swelling, dissipation of electrochemical gradients, leakage of cellular contents, and ultimately, cell lysis.

PFTs are generally secreted by the bacteria as water-soluble monomers (e.g. PFO from *C. perfringens*) or in some cases, as dimers (e.g. Proaerolysin from *Aeromonas hydrophila*) (Buckley, 1999; Tweten et al., 2001). Upon encountering a target membrane, PFTs bind to high-affinity receptors and anchor themselves onto the target cell membrane surface. These receptors are highly varied and range from cholesterol molecules for cholesterol-dependent cytolysins (Alouf, 1999) to 'glycosylphosphatidylinositol-anchored proteins' (GPI-anchored proteins) that bind toxins such as *Clostridium septicum* α-toxin (Gordon et al., 1999) and *A. hydrophila* aerolysin (Fivaz et al., 2001). On stable binding, the molecules diffuse laterally on the plane of the bilayer and undergo oligomerization, a hallmark property of PFTs. Oligomerization in discrete stoichiometries is accomplished either spontaneously or by the proteolytic removal of a polypeptide segment that presumably obscures the oligomerization interface. For example, inactive *A. hydrophila* 'proaerolysin' is converted to active ‘aerolysin’ by the proteolytic removal of a peptide fragment by the host membrane-protease ‘furin’ (Fivaz et al., 2001). Oligomers formed by PFTs are essentially circular and are comprised of monomeric subunits ranging from seven (e.g. *Staphylococcus aureus* α-hemolysin (α-HL), *A. hydrophila* aerolysin) to more than forty (e.g. CDCs) (Heuck et al., 2001). Complete oligomerization into circular complexes then triggers the spontaneous insertion of these complexes into the membrane to create aqueous pores that range between 9 Å to 300 Å in diameter.

Structurally, PFTs can be classified into two types: α-PFTs that insert amphipathic α-helices into the membrane to line the aqueous pore and β-PFTs that form aqueous pores by insertion of an amphipathic β-barrel (Heuck et al., 2001). α-PFTs are best exemplified by the channel-forming ‘colicins’, a family of bacteriocidal PFTs from *Escherichia coli*. Colicin Ia is a particularly striking example of this family that forms small pores ~ 9 Å in diameter (Lakey and Slatin, 2001). A hallmark of this toxin molecule is the presence of buried hydrophobic helices in the water-soluble form of the toxin that are exposed upon target membrane binding and eventually insert into the bilayer. Other examples of α-PFTs include diphtheria toxin and the insecticidal δ-endotoxin Cry from *Bacillus thuringiensis* (Lacy and Stevens, 1998). Since my study involves a β-PFT, I direct you to the following reviews for a discussion of α-PFTs (Gouaux, 1997; Lacy and Stevens, 1998; Lakey and Slatin, 2001).

β-PFTs, unlike α-PFTs, must oligomerize on the target membrane in order to generate the oligomeric transmembrane (TM) β-barrel. β-PFTs represent a growing family of proteins that are involved in bacterial pathogenesis and classic examples include the *S. aureus* α-HL, *A. hydrophila* aerolysin, the *Bacillus anthracis* protective antigen (anthrax PA) and the CDCs of pathogenic Gram-positive bacteria (for a review, see Heuck et al., 2001).

TM β-barrels are ubiquitous from bacteria to man and are found in the outer mitochondrial and chloroplast membranes in eukaryotes and in the outer membrane of Gram-negative bacteria (Buchanan, 1999; Wimley, 2003). There, they serve as 'porins' for the passive translocation of a variety of small-molecular weight metabolites including sugars and siderophores. Recent experiments also implicate TM β-barrels in the translocation of unfolded polypeptide chains through the outer membranes of the mitochondrion and the chloroplast (Gabriel et al., 2001). Most TM β-barrels are comparatively small and contain as few as 8 (OmpA) or as many as 22 (FepA) β-strands (Schulz, 2000). In contrast, the β-barrels formed by β-PFTs vary widely in size, ranging from 14 β-strands in *S. aureus* α-HL and anthrax PA to about 200 β-strands in CDCs (Song et al., 1996; Heuck et al., 2001). Furthermore, while the β-barrels in the outer membrane of bacteria are usually formed by a single polypeptide [with the known exception of the trimeric β-barrel-forming TolC from *E. coli* (Koronakis et al., 2000)], those formed by β-PFTs are always oligomeric (Heuck et al., 2001).

TM β-barrel formation within the confines of the lipid bilayer involves the more-or-less concerted insertion of all the β-strands that constitute the β-barrel (White and Wimley, 1999). Unlike the insertion of individual α-helices of a TM α-helical bundle, the pairwise insertion of single amphipathic β-hairpins is not energetically favored because within the nonpolar core of the bilayer that lacks hydrogen-bond donors and acceptors, the transfer of non-hydrogen-bonded polar atoms of a β-hairpin-forming polypeptide is energetically costly. This cost is offset when the hydrogen bonding potential of the polypeptide is satisfied by matching backbone hydrogen-bond donors and acceptors and closing the β-sheet edges into a β-barrel. Thus, insertion of a preformed β-barrel or the formation of the β-barrel concomitant with membrane insertion is most favored as a mechanism for β-PFT pore formation (for an extensive review on TM β-barrel folding and insertion, see White and Wimley, 1999). Although no conclusive data exist for the timing of TM β-barrel formation and insertion in PFTs, it is presumed that a 'prepore' state (a complete circular oligomer poised for insertion) allows the concerted insertion of the β-hairpins from individual monomers. Furthermore, since the TM β-barrel is amphipathic, with nonpolar and polar sidechains facing the bilayer and the aqueous pore, respectively, concerted insertion of the β-hairpins to displace the lipids in the center of the pore seems most likely.

S. aureus α-HL

An important paradigm for pore formation by β-PFTs was established with the crystal structures of the detergent-solubilized *S. aureus* α-HL heptamer (Figure 1) and the water-soluble monomeric form of the homologous *S. aureus* LukF (Figure 2A) (Song et al., 1996; Olson et al., 1999). With each monomer contributing a single amphipathic TM β-hairpin, the mushroom-shaped α-HL heptamer formed a 14-stranded TM β-barrel that enclosed an aqueous pore ~ 15 Å in diameter. The structure of the water-soluble monomeric form of LukF was found to closely resemble that of a monomer in the α-HL heptamer except at two different places. First, in the water-soluble form of LukF, the polypeptide stretch that eventually forms the TM β-hairpin was folded into three short β-strands and packed against the core β-sheet in order to protect hydrophobic residues of the amphipathic β-hairpins from exposure of solvent. Second, residues 1-20 at the N-terminus of LukF form a loop and a short β-strand that in the α-HL heptamer is significantly displaced and found to interact with the core β-sheet of the neighboring subunit. This N-terminal sequence is therefore termed the 'amino-latch'. Although not experimentally demonstrated, it is presumed that membrane binding elicits these conformational changes in the α-HL monomer. Biochemical analyses also revealed two intermediate stages in the transition of the water-soluble monomer into a membrane-inserted heptamer: the membrane-bound monomer (Walker et al., 1992) and the heptameric prepore complex poised for TM β-barrel insertion (Walker et al., 1995). For recent reviews on α-HL, see Prevost et al., 2001 and Montoya and Gouaux, 2003.

CDCs

The CDCs are a family of β-PFTs that serve as virulence factors for several genera of pathogenic Gram-positive bacteria (for a review, see Tweten et al., 2001). And, as their name implies, they are active or form pores only in membranes that contain cholesterol, a molecule that is unique to the membranes of higher eukaryotes. The CDCs are widely distributed and have been identified in 23 different species from five different genera of bacteria that include *Clostridium*, *Streptococcus*, *Listeria, Bacillus* and most recently, *Arcanobacterium* (Alouf, 2000). Although all CDCs are thought to operate via

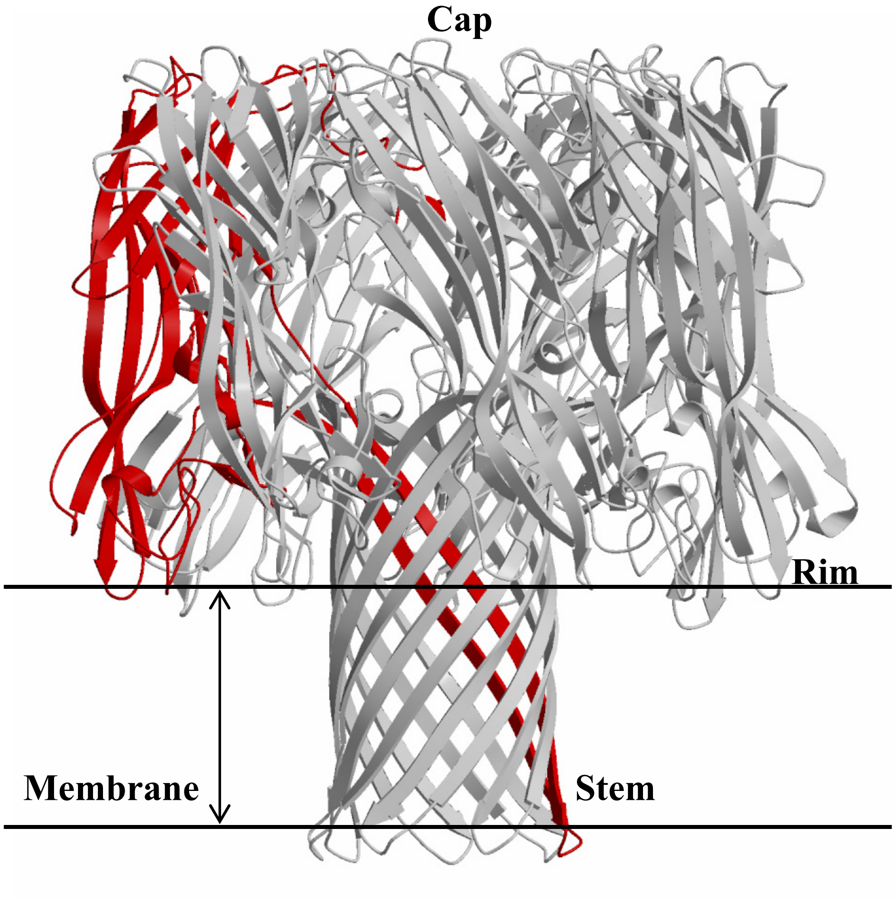

Figure 1. Crystal structure of the *S. aureus* α-HL heptamer. The cap, rim and stem domains are labeled. One monomer in the heptamer is colored. The image was generated using MOLSCRIPT (Kraulis, 1991) and rendered with Raster3D (Merritt and Bacon, 1997).

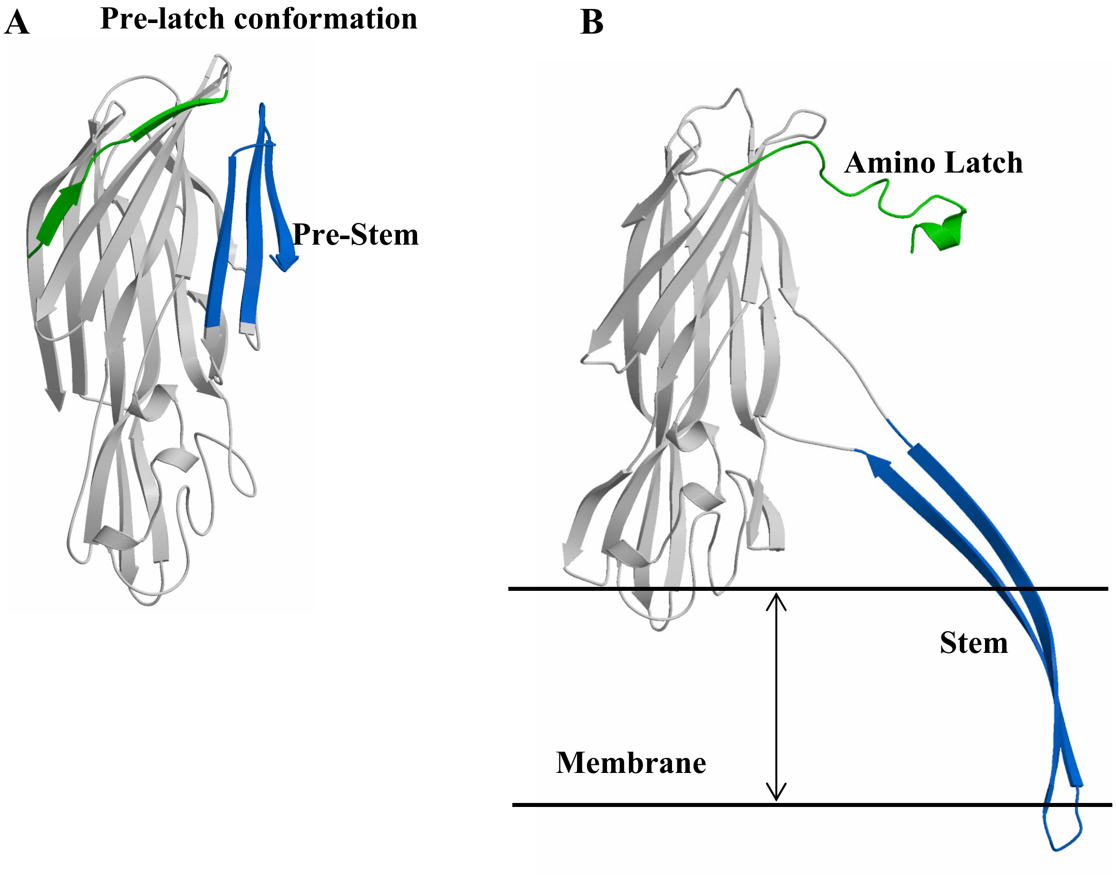
A
Pre-latch conformation
Pre-Stem
B
Amino Latch
Stem
Membrane

Figure 2. Comparison of the structures of LukF and α-HL. Comparison of the crystal structures of the LukF monomer (A) and a monomer of the homologous α-HL heptamer (B) reveals regions of the monomer that undergo appreciable conformational changes during oligomerization and membrane insertion. The pre-latch conformation, the amino-latch and the pre-stem/stem regions of the toxins are colored and labeled. The images were generated using MOLSCRIPT (Kraulis, 1991) and rendered with Raster3D (Merritt and Bacon, 1997).

a similar mechanism of action, they are known to fulfill diverse roles in establishing bacterial pathogenesis. For example, the CDC Listeriolysin O (LLO) form *L. monocytogenes* forms holes in the membranes of acidified phagocytic vesicles and, in concert with listerial phospholipases, dissolves the membrane and facilitates the escape of the phagocytosed bacteria into the host cytosol (Portnoy et al., 2002). In contrast, the CDC streptolysin O (SLO) from *Streptococcus pyogenes* is presumed to form holes in the host cell membrane that are used by the bacteria to inject enzymes and other effector molecules into the host cytosol, similar in mechanism to Type III secretion in Gram-negative bacteria (Madden et al., 2001).

At the molecular level, the CDCs are 50-70 kDa single-chain polypeptides that share 40-70% sequence identity (Figure 3) (Tweten et al., 2001). Based on the relatively high degree of sequence similarity, the CDCs are assumed to adopt similar three-dimensional structures and modes of action. A striking feature in the primary sequence of 8 of the 11 sequenced CDCs is a highly conserved 11-residue sequence, ECTGLAWEWWR, situated near the C-terminus of the polypeptide. Modification of the Cys residue within this sequence (the only Cys in the entire molecule) with thiol-specific reagents was shown to completely inactivate the toxin (Iwamoto et al., 1987). In fact, the CDCs were previously referred to as ‘thiol-activated cytolysins or TACs’, since studies involving crude extracts containing these toxins were observed to lose activity over time and the addition of thiol-containing reducing agents such as dithiothreitol or β-mercaptoethanol was found to restore activity, thereby suggesting that the loss of activity was due to the oxidation of protein Cys thiol(s) that was critical for the activity of these

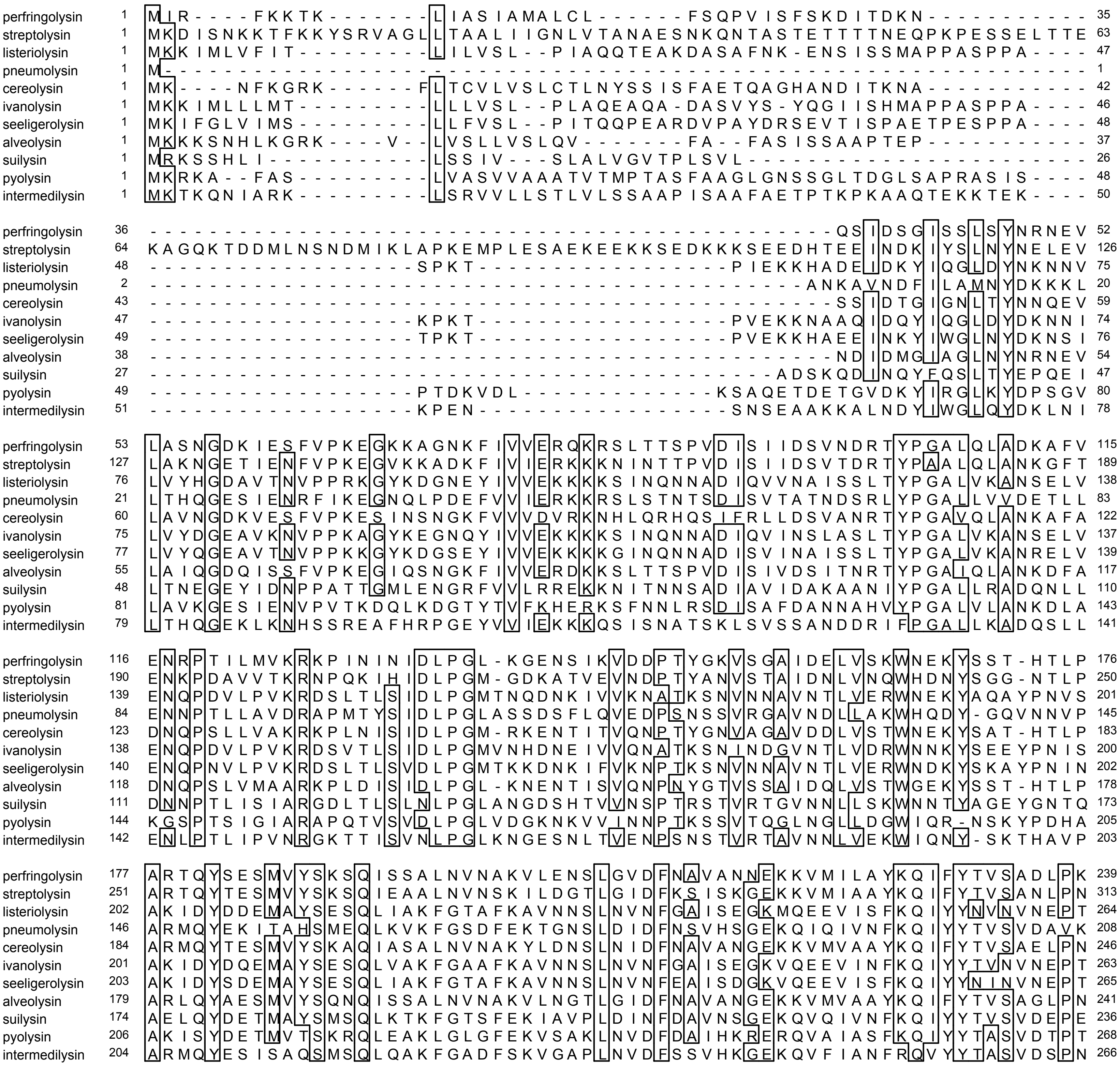
perfringolysin 1 MIR----FKKTK-------LIASIAMALCL------FSQPVISFSKDITDKN----------- 35
streptolysin 1 MKDISNKKTFKKYSRVAGLLTAALIIGNLVTANAESNKQNTASTETTTTNEQPKPESSELTTE 63
listeriolysin 1 MKKIMLVFIT---------LILVSL--PIAQQTEAKDASAFNK-ENSISSMAPPASPPA---- 47
pneumolysin 1 M-- 1
cereolysin 1 MK----NFKGRK------FLTCVLVSLCTLNYSSISFAETQAGHANDITKNA----------- 42
ivanolysin 1 MKKIMLLLMT---------LLLVSL--PLAQEAQA-DASVYS-YQGIISHMAPPASPPA---- 46
seeligerolysin 1 MKIFGLVIMS---------LLFVSL--PITQQPEARDVPAYDRSEVTISPAETPESPPA---- 48
alveolysin 1 MKKKSNHLKGRK----V--LVSLLVSLQV-------FA--FASISSAAPTEP----------- 37
suilysin 1 MRKSSHLI-----------LSSIV---SLALVGVTPLSVL----------------------- 26
pyolysin 1 MKRKA--FAS---------LVASVVAAATVTMPTASFAAGLGNSSGLTDGLSAPRASIS---- 48
intermedilysin 1 MKTKQNIARK---------LSRVVLLSTLVLSSAAPISAAFAETPTKPKAAQTEKKTEK---- 50
perfringolysin 36 --QSIDSGISSLSYNRNEV 52
streptolysin 64 KAGQKTDDMLNSNDMIKLAPKEMPLESAEKEEKKSEDKKKSEEDHTEEINDKIYSLNYNELEV 126
listeriolysin 48 -------------------SPKT----------------PIEKKHADEIDKYIQGLDYNKNNV 75
pneumolysin 2 --ANKAVNDFILAMNYDKKKL 20
cereolysin 43 --SSIDTGIGNLTYNNQEV 59
ivanolysin 47 -------------------KPKT----------------PVEKKNAAQIDQYIQGLDYDKNNI 74
seeligerolysin 49 -------------------TPKT----------------PVEKKHAEEINKYIWGLNYDKNSI 76
alveolysin 38 --NDIDMGIAGLNYNRNEV 54
suilysin 27 --ADSKQDINQYFQSLTYEPQEI 47
pyolysin 49 -------------------PTDKVDL------------KSAQETDETGVDKYIRGLKYDPSGV 80
intermedilysin 51 -------------------KPEN----------------SNSEAAKKALNDYIWGLQYDKLNI 78
perfringolysin 53 LASNGDKIESFVPKEGKKAGNKFIVVERQKRSLTTSPVDISIIDSVNDRTYPGALQLADKAFV 115
streptolysin 127 LAKNGETIENFVPKEGVKKADKFIVIERKKKNINTTPVDISIIDSVTDRTYPAALQLANKGFT 189
listeriolysin 76 LVYHGDAVTNVPPRKGYKDGNEYIVVEKKKKSINQNNADIQVVNAISSLTYPGALVKANSELV 138
pneumolysin 21 LTHQGESIENRFIKEGNQLPDEFVVIERKKRSLSTNTSDISVTATNDSRLYPGALLVVDETLL 83
cereolysin 60 LAVNGDKVESFVPKESINSNGKFVVVDVRKNHLQRHQSIFRLLDSVANRTYPGAVQLANKAFA 122
ivanolysin 75 LVYDGEAVKNVPPKAGYKEGNQYIVVEKKKKSINQNNADIQVINSLASLTYPGALVKANSELV 137
seeligerolysin 77 LVYQGEAVTNVPPKKGYKDGSEYIVVEKKKKGINQNNADISVINAISSLTYPGALVKANRELV 139
alveolysin 55 LAIQGDQISSFVPKEGIQSNGKFIVVERDKKSLTTSPVDISIVDSITNRTYPGAIQLANKDFA 117
suilysin 48 LTNEGEYIDNPPATTGMLENGRFVVLRREKKNITNNSADIAVIDAKAANIYPGALLRADQNLL 110
pyolysin 81 LAVKGESIENVPVTKDQLKDGTYTVFKHERKSFNNLRSDISAFDANNAHVYPGALVLANKDLA 143
intermedilysin 79 LTHQGEKLKNHSSREAFHRPGEYVVIEKKKQSISNATSKLSVSSANDDRIFPGALLKADQSLL 141
perfringolysin 116 ENRPTILMVKRKPININIDLPGL-KGENSIKVDDPTYGKVSGAIDELVSKWNEKYSST-HTLP 176
streptolysin 190 ENKPDAVVTKRNPQKIHIDLPGM-GDKATVEVNDPTYANVSTAIDNLVNQWHDNYSGG-NTLP 250
listeriolysin 139 ENQPDVLPVKRDSLTLSIDLPGMTNQDNKIVVKNATKSNVNNAVNTLVERWNEKYAQAYPNVS 201
pneumolysin 84 ENNPTLLAVDRAPMTYSIDLPGLASSDSFLQVEDPSNSSVRGAVNDLLAKWHQDY-GQVNNVP 145
cereolysin 123 DNQPSLLVAKRKPLNISIDLPGM-RKENTITVQNPTYGNVAGAVDDLVSTWNEKYSAT-HTLP 183
ivanolysin 138 ENQPDVLPVKRDSVTLSIDLPGMVNHDNEIVVQNATKSNINDGVNTLVDRWNNKYSEEYPNIS 200
seeligerolysin 140 ENQPNVLPVKRDSLTLSVDLPGMTKKDNKIFVKNPTKSNVNNAVNTLVERWNDKYSKAYPNIN 202
alveolysin 118 DNQPSLVMAARKPLDISIDLPGL-KNENTISVQNPNYGTVSSAIDQLVSTWGEKYSST-HTLP 178
suilysin 111 DNNPTLISIARGDLTLSLNLPGLANGDSHTVVNSPTRSTVRTGVNNLLSKWNNTYAGEYGNTQ 173
pyolysin 144 KGSPTSIGIARAPQTVSVDLPGLVDGKNKVVINNPTKSSVTQGLNGLLDGWIQR-NSKYPDHA 205
intermedilysin 142 ENLPTLIPVNRGKTTISVNLPGLKNGESNLTVENPSNSTVRTAVNNLVEKWIQNY-SKTHAVP 203
perfringolysin 177 ARTQYSESMVYSKSQISSALNVNAKVLENSLGVDFNAVANNEKKVMILAYKQIFYTVSADLPK 239
streptolysin 251 ARTQYTESMVYSKSQIEAALNVNSKILDGTLGIDFKSISKGEKKVMIAAYKQIFYTVSANLPN 313
listeriolysin 202 AKIDYDDEMAYSESQLIAKFGTAFKAVNNSLNVNFGAISEGKMQEEVISFKQIYYNVNVNEPT 264
pneumolysin 146 ARMQYEKITAHSMEQLKVKFGSDFEKTGNSLDIDFNSVHSGEKQIQIVNFKQIYYTVSVDAVK 208
cereolysin 184 ARMQYTESMVYSKAQIASALNVNAKYLDNSLNIDFNAVANGEKKVMVAAYKQIFYTVSAELPN 246
ivanolysin 201 AKIDYDQEMAYSESQLVAKFGAAFKAVNNSLNVNFGAISEGKVQEEVINFKQIYYTVNVNEPT 263
seeligerolysin 203 AKIDYSDEMAYSESQLIAKFGTAFKAVNNSLNVNFEAISDGKVQEEVISFKQIYYNINVNEPT 265
alveolysin 179 ARLQYAESMVYSQNQISSALNVNAKVLNGTLGIDFNAVANGEKKVMVAAYKQIFYTVSAGLPN 241
suilysin 174 AELQYDETMAYSMSQLKTKFGTSFEKIAVPLDINFDAVNSGEKQVQIVNFKQIYYTVSVDEPE 236
pyolysin 206 AKISYDETMVTSKRQLEAKLGLGFEKVSAKLNVDFDAIHKRERQVAIASFKQIYYTASVDTPT 268
intermedilysin 204 ARMQYESISAQSMSQLQAKFGADFSKVGAPLNVDFSSVHKGEKQVFIANFRQVYYTASVDSPN 266

Figure 3. Primary structures of the sequenced CDCs. Identical residues are boxed.

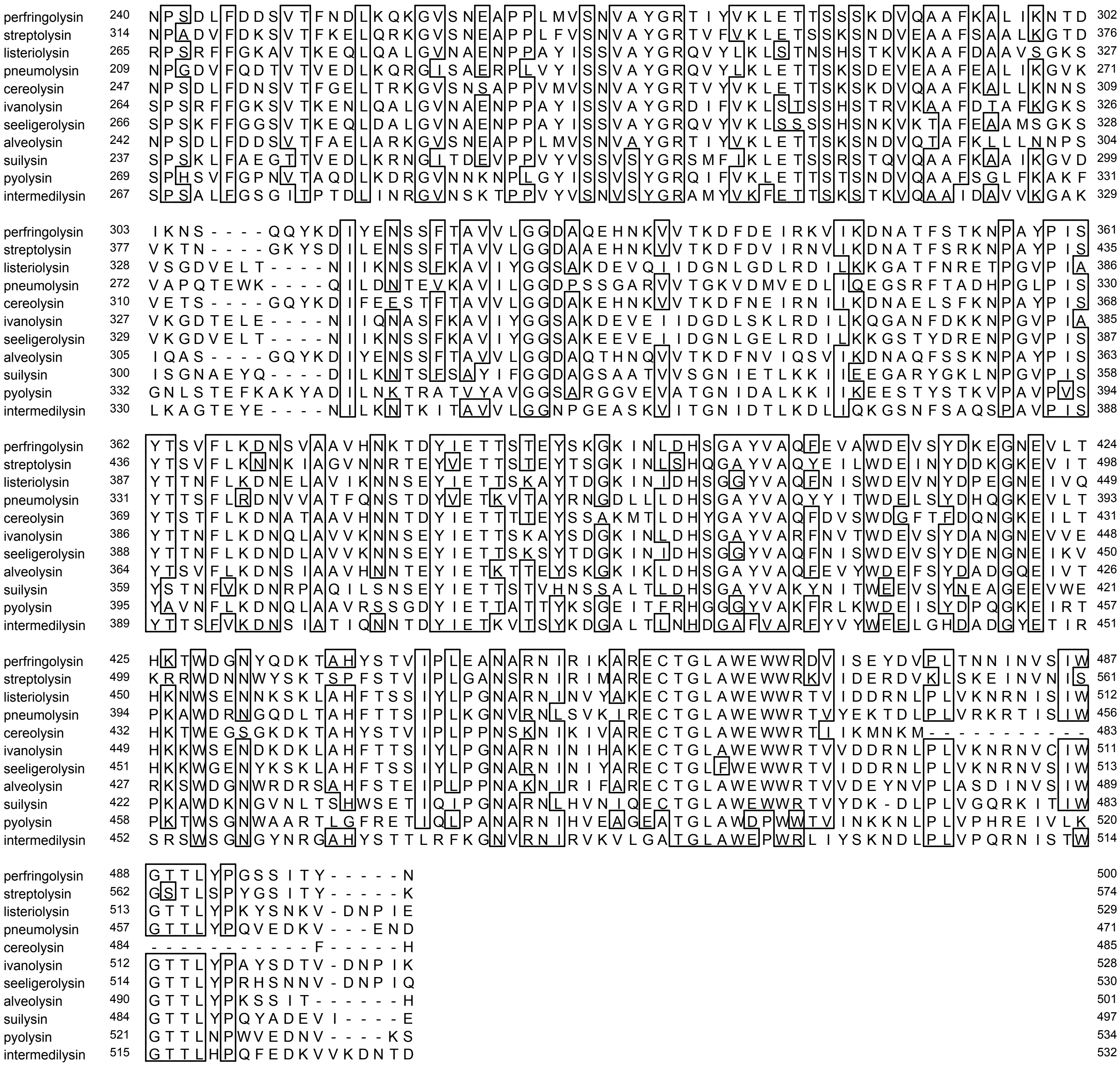

```
perfringolysin  240 NPSDLFDDSVTFNDLKQKGVSNEAPPLMVSNVAYGRTIYVKLETTSSSKDVQAAFKALIKNTD 302
streptolysin    314 NPADVFDKSVTFKELQRKGVSNEAPPLFVSNVAYGRTVFVKLETSSKSNDVEAAFSAALKGTD 376
listeriolysin   265 RPSRFFGKAVTKEQLQALGVNAENPPAYISSVAYGRQVYLKLSTNSHSTKVKAAFDAAVSGKS 327
pneumolysin     209 NPGDVFQDTVTVEDLKQRGISAERPLVYISSVAYGRQVYLKLETTSKSDEVEAAFEALIKGVK 271
cereolysin      247 NPSDLFDNSVTFGELTRKGVSNSAPPVMVSNVAYGRTVYVKLETTSKSKDVQAAFKALLKNNS 309
ivanolysin      264 SPSRFFGKSVTKENLQALGVNAENPPAYISSVAYGRDIFVKLSTSSHSTRVKAAFDTAFKGKS 326
seeligerolysin  266 SPSKFFGGSVTKEQLDALGVNAENPPAYISSVAYGRQVYVKLSSSSHSNKVKTAFEAAMSGKS 328
alveolysin      242 NPSDLFDDSVTFAELARKGVSNEAPPLMVSNVAYGRTIYVKLETTSKSNDVQTAFKLLLNNPS 304
suilysin        237 SPSKLFAEGTTVEDLKRNGITDEVPPVYVSSVSYGRSMFIKLETSSRSTQVQAAFKAAIKGVD 299
pyolysin        269 SPHSVFGPNVTAQDLKDRGVNNKNPLGYISSVSYGRQIFVKLETTSTSNDVQAAFSGLFKAKF 331
intermedilysin  267 SPSALFGSGITPTDLINRGVNSKTPPVYVSNVSYGRAMYVKFETTSKSTKVQAAIDAVVKGAK 329

perfringolysin  303 IKNS----QQYKDIYENSSFTAVVLGGDAQEHNKVVTKDFDEIRKVIKDNATFSTKNPAYPIS 361
streptolysin    377 VKTN----GKYSDILENSSFTAVVLGGDAAEHNKVVTKDFDVIRNVIKDNATFSRKNPAYPIS 435
listeriolysin   328 VSGDVELT----NIIKNSSFKAVIYGGSAKDEVQIIDGNLGDLRDILKKGATFNRETPGVPIA 386
pneumolysin     272 VAPQTEWK----QILDNTEVKAVILGGDPSSGARVVTGKVDMVEDLIQEGSRFTADHPGLPIS 330
cereolysin      310 VETS----GQYKDIFEESTFTAVVLGGDAKEHNKVVTKDFNEIRNIIKDNAELSFKNPAYPIS 368
ivanolysin      327 VKGDTELE----NIIQNASFKAVIYGGSAKDEVEIIDGDLSKLRDILKQGANFDKKNPGVPIA 385
seeligerolysin  329 VKGDVELT----NIIKNSSFKAVIYGGSAKEEVEIIDGNLGELRDILKKGSTYDRENPGVPIS 387
alveolysin      305 IQAS----GQYKDIYENSSFTAVVLGGDAQTHNQVVTKDFNVIQSVIKDNAQFSSKNPAYPIS 363
suilysin        300 ISGNAEYQ----DILKNTSFSAYIFGGDAGSAATVVSGNIETLKKIIEEGARYGKLNPGVPIS 358
pyolysin        332 GNLSTEFKAKYADILNKTRATVYAVGGSARGGVEVATGNIDALKKIIKEESTYSTKVPAVPVS 394
intermedilysin  330 LKAGTEYE----NILKNTKITAVVLGGNPGEASKVITGNIDTLKDLIQKGSNFSAQSPAVPIS 388

perfringolysin  362 YTSVFLKDNSVAAVHNKTDYIETTSTEYSKGKINLDHSGAYVAQFEVAWDEVSYDKEGNEVLT 424
streptolysin    436 YTSVFLKNNKIAGVNNRTEYVETTSTEYTSGKINLSHQGAYVAQYEILWDEINYDDKGKEVIT 498
listeriolysin   387 YTTNFLKDNELAVIKNNSEYIETTSKAYTDGKINIDHSGGYVAQFNISWDEVNYDPEGNEIVQ 449
pneumolysin     331 YTTSFLRDNVVATFQNSTDYVETKVTAYRNGDLLLDHSGAYVAQYYITWDELSYDHQGKEVLT 393
cereolysin      369 YTSTFLKDNATAAVHNNTDYIETTTTEYSSAKMTLDHYGAYVAQFDVSWDGFTFDQNGKEILT 431
ivanolysin      386 YTTNFLKDNQLAVVKNNSEYIETTSKAYSDGKINLDHSGAYVARFNVTWDEVSYDANGNEVVE 448
seeligerolysin  388 YTTNFLKDNDLAVVKNNSEYIETTSKSYTDGKINIDHSGGYVAQFNISWDEVSYDENGNEIKV 450
alveolysin      364 YTSVFLKDNSIAAVHNNTEYIETKTTEYSKGKIKLDHSGAYVAQFEVYWDEFSYDADGQEIVT 426
suilysin        359 YSTNFVKDNRPAQILSNSEYIETTSTVHNSSALTLDHSGAYVAKYNITWEEVSYNEAGEEVWE 421
pyolysin        395 YAVNFLKDNQLAAVRSSGDYIETTATTYKSGEITFRHGGGYVAKFRLKWDEISYDPQGKEIRT 457
intermedilysin  389 YTTSFVKDNSIATIQNNTDYIETKVTSYKDGALTLNHDGAFVARFYVYWEELGHDADGYETIR 451

perfringolysin  425 HKTWDGNYQDKTAHYSTVIPLEANARNIRIKARECTGLAWEWWRDVISEYDVPLTNNINVSIW 487
streptolysin    499 KRRWDNNWYSKTSPFSTVIPLGANSRNIRIMARECTGLAWEWWRKVIDERDVKLSKEINVNIS 561
listeriolysin   450 HKNWSENNKSKLAHFTSSIYLPGNARNINVYAKECTGLAWEWWRTVIDDRNLPLVKNRNISIW 512
pneumolysin     394 PKAWDRNGQDLTAHFTTSIPLKGNVRNLSVKIRECTGLAWEWWRTVYEKTDLPLVRKRTISIW 456
cereolysin      432 HKTWEGSGKDKTAHYSTVIPLPPNSKNIKIVARECTGLAWEWWRTIIKMNKM----------- 483
ivanolysin      449 HKKWSENDKDKLAHFTTSIYLPGNARNINIHAKECTGLAWEWWRTVVDDRNLPLVKNRNVCIW 511
seeligerolysin  451 HKKWGENYKSKLAHFTSSIYLPGNARNINIYARECTGLFWEWWRTVIDDRNLPLVKNRNVSIW 513
alveolysin      427 RKSWDGNWRDRSAHFSTEIPLPPNAKNIRIFARECTGLAWEWWRTVVDEYNVPLASDINVSIW 489
suilysin        422 PKAWDKNGVNLTSHWSETIQIPGNARNLHVNIQECTGLAWEWWRTVYDK-DLPLVGQRKITIW 483
pyolysin        458 PKTWSGNWAARTLGFRETIQLPANARNIHVEAGEATGLAWDPWWTVINKKNLPLVPHREIVLK 520
intermedilysin  452 SRSWSGNGYNRGAHYSTTLRFKGNVRNIRVKVLGATGLAWEPWRLIYSKNDLPLVPQRNISTW 514

perfringolysin  488 GTTLYPGSSITY-----N 500
streptolysin    562 GSTLSPYGSITY-----K 574
listeriolysin   513 GTTLYPKYSNKV-DNPIE 529
pneumolysin     457 GTTLYPQVEDKV---END 471
cereolysin      484 -----------F-----H 485
ivanolysin      512 GTTLYPAYSDTV-DNPIK 528
seeligerolysin  514 GTTLYPRHSNNV-DNPIQ 530
alveolysin      490 GTTLYPKSSIT------H 501
suilysin        484 GTTLYPQYADEVI----E 497
pyolysin        521 GTTLNPWVEDNV----KS 534
intermedilysin  515 GTTLHPQFEDKVVKDNTD 532
```

Figure 3. (continued)

toxins (Billington et al., 2000). However, later experiments clearly demonstrated that the Cys did not play a substantial role since mutation of the Cys to Ala did not greatly alter the extent of pore formation (Pinkney et al., 1989; Saunders et al., 1989; Shepard et al., 1998). These toxins have since been referred to as 'cholesterol-dependent cytolysins' because all members of the family exhibit an absolute dependence on the presence of cholesterol in the target membrane for their cytolytic activity (Tweten et al., 2001).

As with other bacterial PFTs, structural dimorphism is a characteristic hallmark of the CDC family of toxins. The CDCs are secreted as water-soluble monomers into the extracellular milieu of the host. Upon encountering a cholesterol-containing membrane, the CDCs form large, circular homo-oligomeric complexes on the membrane surface and eventually insert into the bilayer to create large aqueous pores. Based on electron microscopy images, CDC pores have been estimated to be ~ 300 Å in diameter with each oligomeric complex containing ~ 50 monomers (Oloffson et al., 1993).

The conversion of a CDC polypeptide from a stably-folded water-soluble form into an integrated membrane form is spontaneous. This property is encoded in the structure of the CDC molecule itself, since the transformation is achieved without the assistance of other protein molecules (e.g. chaperones) or an energy source after being triggered by specific interactions with the target membrane bilayer (Heuck et al., 2001). How this is accomplished remains a fundamental issue that has intrigued researchers in the field for a long time.

Inspection of the primary structures of the CDCs did not reveal any stretches of hydrophobicity that would be expected to insert into, and span, the nonpolar core of the membrane bilayer (Figure 3). However, mutagenesis data indicated that residues in the conserved 11-residue sequence at the C-terminus are critical for pore formation, suggesting that they were directly involved in membrane insertion and presumably, in cholesterol binding (Iwamoto et al., 1987; Sekino-Suzuki et al., 1996; Jacobs et al., 1999). The first speculation as to how CDCs penetrated the membrane bilayer came when the crystal structure of the water-soluble form of PFO was determined.

PFO structure

The three dimensional structure of the water-soluble monomeric form of PFO was solved at 2.2 Å resolution by X-ray crystallography and is the only high resolution structure of a CDC (Figure 4) (Rossjohn et al., 1997). The mature molecule (after signal sequence cleavage) composed of 472 residues, assumes an unusual elongated shape (115 Å × 30 Å × 55 Å) and is rich in β-sheet. Based on the arrangement of the polypeptide chain within the structure, the molecule has been divided into three discontinuous domains (designated domains 1-3 or D1-3) and a contiguous C-terminal domain (designated domain 4 or D4). Domain 1 (residues 37-53, 90-178, 229-274, 350-373) is located at one end of the molecule and has both α-helix and β-sheet content, with a long helix packed against a 7-stranded antiparallel β-sheet. Domain 2 (residues 54-89, 374-390), on the other hand, is simply a long, curved single-layer 3-stranded β-sheet that links domain 1 at one end of the molecule with domain 4 at the other. Domain 3 (residues 179-228, 275-349) which extends from the core β-sheet of domain 1, adopts a α/β/α topology with a core 5-stranded β-sheet sandwiched between two layers of three

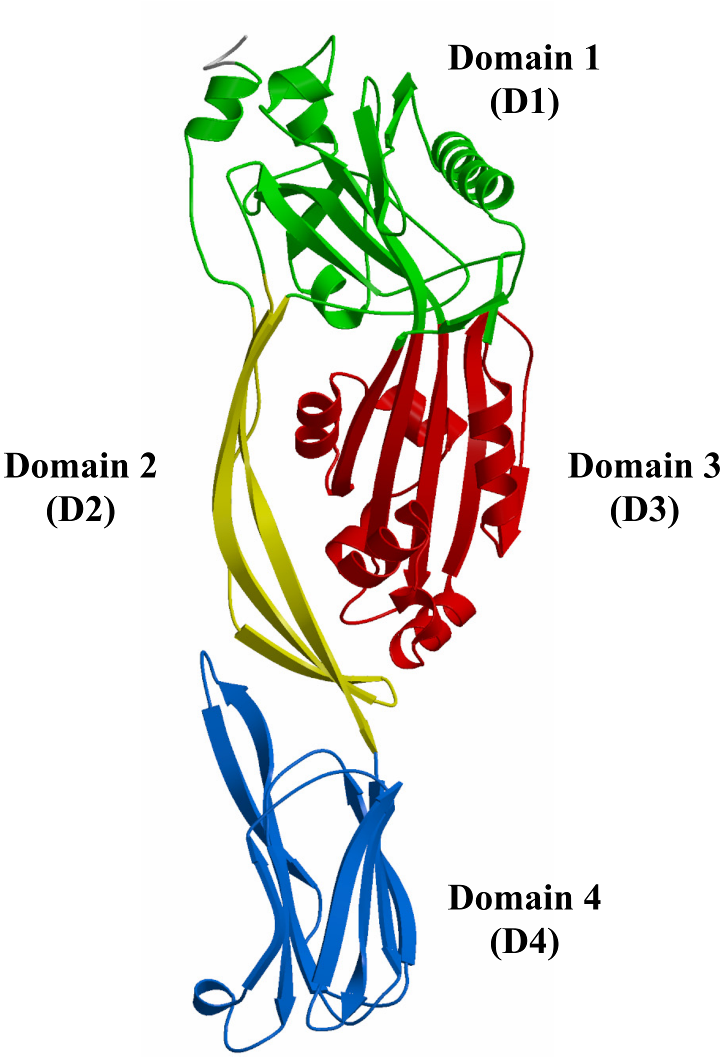
Domain 1
(D1)
Domain 2
(D2)
Domain 3
(D3)
Domain 4
(D4)

Figure 4. Crystal structure of monomeric PFO. Domains 1-4 (D1-D4) are colored and denoted. The image was generated using MOLSCRIPT (Kraulis, 1991) and rendered with Raster3D (Merritt and Bacon, 1997).

short α-helices each. Domain 4 (residues 391-500) adopts the ubiquitous β-sandwich fold comprised of two four-stranded antiparallel β-sheets. Interestingly, the highly-conserved 11-residue sequence implicated in membrane insertion was found to form an extended, solvent-accessible loop at the tip of the domain 4 β-sandwich, where it appeared poised to interact with the membrane. This loop will hereafter be referred to as the 'Trp-rich' loop.

Membrane-interacting regions of PFO

Based largely on the location of D4 in monomeric PFO and also on the mutagenesis data, Rossjohn et al. (1997) proposed an attractive model for PFO membrane insertion in which the 29 Å long D4 β-sandwich completely inserted into the membrane bilayer to form the lipid-water interface of the aqueous pore in the oligomeric form of the toxin. The crystallographers also envisioned and modeled a binding site for a single cholesterol molecule in the crystal structure of the PFO monomer. They suggested that the Trp-rich loop in D4 undergoes a conformational change and creates a binding site for cholesterol that is sandwiched between the rearranged loop and one face of the D4 β-sandwich. The Trp-rich loop bound to a cholesterol molecule was then proposed to form a 'hydrophobic dagger' that completely spanned the membrane. Their model also included cholesterol molecules on the other face of the D4 β-sandwich to protect the β-sheet's hydrophilic face from the nonpolar core of the bilayer. In essence, domain 4 of each monomer was modeled with bound cholesterol molecules on both faces of the β-sandwich while its edges were involved in intermolecular interactions with the β-sandwich edges of neighboring monomers to create a D4 'β-barrel' that interfaced the aqueous pore and the nonpolar core of the lipid bilayer. All other domains of the PFO molecule were situated far above the plane of the membrane.

This model was consistent with the following experimental observations. The PFO monomer was shown to undergo relatively modest changes in secondary structure upon membrane insertion by circular dichroism (CD) analysis (Nakamura et al., 1995). A proteolytically-derived C-terminal fragment (residues 304-500 that included D4) was able to interact with both the target membrane and intact PFO molecules on the membrane surface (Iwamoto et al., 1990; Tweten et al., 1991). Furthermore, some or all of the six Trp residues within D4 were shown to come into contact with the core of the membrane bilayer. This was determined based on the quenching of PFO Trp fluorescence by brominated lipids incorporated into cholesterol-containing liposomes (Nakamura et al., 1998).

In apparent conflict with the details of model proposed by Rossjohn et al. (1997), cysteine-scanning mutagenesis and fluorescence spectroscopy data obtained with the CDC, SLO suggested that at least a part of D3 came into contact with the core of the membrane bilayer (Palmer et al., 1996; Palmer et al., 1998). This was determined by covalently attaching acrylodan, an environmentally-sensitive fluorophore to single cysteines engineered into the SLO polypeptide, and observing the changes in the dye’s emission spectra before and after pore formation. However, these data were fragmentary rather than complete and did reveal neither the structure of the polypeptide that contacted the bilayer nor its degree of membrane penetration. These observations formed the bases of further inquiry into the protein-membrane interactions of the CDCs.

Elegant fluorescence spectroscopy experiments with PFO later unequivocally demonstrated that the transmembrane regions of the molecule that form the interface between the aqueous pore and the nonpolar core of the lipid bilayer in the membrane-inserted oligomer originate from D3 and not from D4 as previously suggested (Figure 5) (Shepard et al., 1998; Shatursky et al., 1999; reviewed in Heuck et al., 2001). In this ground-breaking series of experiments, residues 189-217 and 288-311 in D3 were substituted, one at a time, with a single Cys in a functional, Cys-free derivative of PFO (C459A). The water-sensitive fluorescent dye, NBD, was covalently attached to a single Cys at each position and the dye's spectral properties were determined prior to, and after, pore formation in liposomal membranes. Movement of the NBD dye from a polar to a nonpolar environment results in a pronounced increase in its fluorescence lifetime (Heuck and Johnson, 2002). After PFO membrane insertion, the NBD dye detected an alternating pattern of aqueous and nonpolar environments every successive residue, thereby showing that these two stretches of polypeptide are in a β-sheet conformation. Had the membrane-interacting regions been α-helical, the dye would have detected a pattern of aqueous and nonpolar environments as predicted by a helical wheel analysis, as demonstrated recently in the case of equinatoxin II (EqtII) from the sea anemone, *Actinia equina* (Malovrh et al., 2003).

Consistent with the idea that these segments in PFO formed two β-hairpins that interfaced the aqueous pore and the nonpolar core of the lipid bilayer, NBD probes exposed to a nonpolar environment were quenched by nitroxide moieties attached to the acyl chain of the phospholipids, while probes exposed to a polar environment were

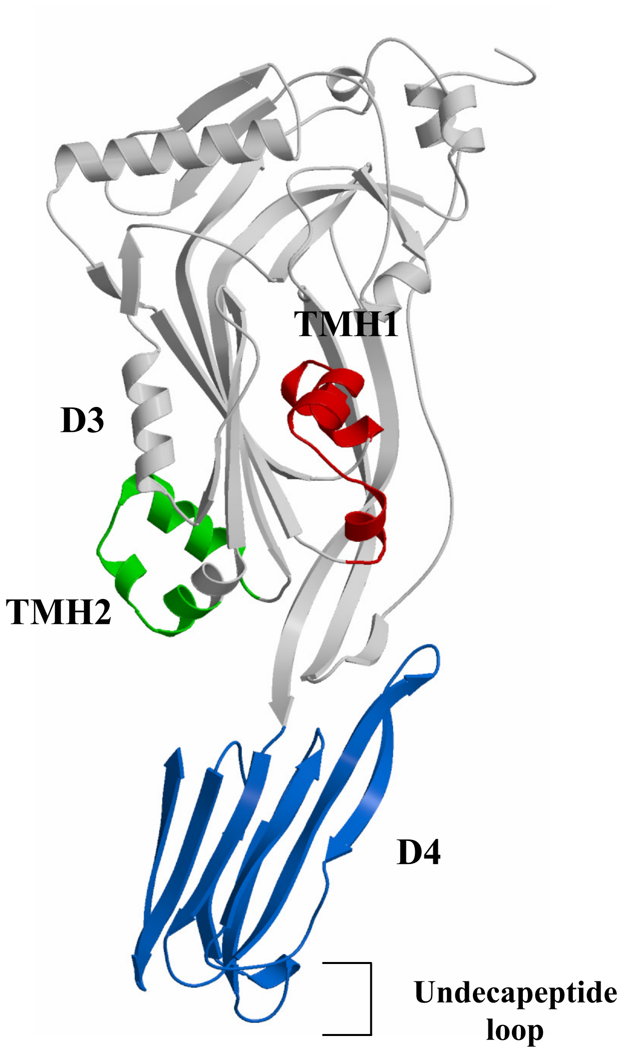

Figure 5. Origin of the transmembrane segments of PFO. Initially, D4 (shown in blue) was proposed to span the membrane bilayer (Rossjohn et al., 1997). Location of the conserved 11-residue sequence (undecapeptide) implicated in membrane insertion is shown. Later, six short α-helices in D3 were shown to unfold to form the two TM β-hairpins, TMH1 (red) and TMH2 (green), that each monomer contributes to the β-barrel (Shepard et al., 1998; Shatursky et al., 1999). The image was generated using MOLSCRIPT (Kraulis, 1991) and rendered with Raster3D (Merritt and Bacon, 1997).

quenched by hydrophilic iodide ions (Heuck and Johnson, 2002). These TM β-hairpins will hereafter be referred to as TMH1 (residues 189-217) and TMH2 (residues 288-311) (Figure 5). Interestingly, both TMHs were each folded into short α-helices in the water-soluble PFO monomer. Thus, each PFO monomer was found to undergo a helix-to-sheet transition and contribute two amphipathic β-hairpins to the large TM β-barrel formed by the membrane-inserted oligomer. These structural changes were unprecedented among bacterial pore-forming toxins and constituted a new paradigm for the insertion of CDCs into target membranes. Thus, the CDCs were shown to be β-PFTs.

Since D3 is the pore-forming domain, the model proposed by Rossjohn et al. (1997) appears to be incorrect. This result then elicits the following questions: where is D4 in the oligomeric pore complex, and how does it interact with the membrane bilayer?

As briefly mentioned earlier, six of seven highly-conserved Trp residues in PFO are located in the C-terminal D4, while a lone Trp is located in D1. Consistent with the widely-held view that the Trp-rich loop in D4 inserts into the membrane and is partly responsible for pore formation, Nakamura et al. (1998) found that the binding of PFO to cholesterol-containing vesicles is accompanied by an increase in Trp emission that can by quenched by bromine atoms attached to the acyl chain of phospholipids in the membrane bilayer. These data, coupled with the finding that the lone Trp in D1 does not contribute to the membrane-dependent change in Trp fluorescence intensity (Nakamura et al., 1998), suggested that a few or all of the surface-exposed Trps in D4 entered the bilayer during pore formation.

To determine the extent of membrane penetration by D4, Heuck et al. (2000)

used nitroxide-labeled phospholipids with the quencher moiety located at different depths within the bilayer to measure the extent of quenching of D4 Trp emission intensity. Surprisingly, the Trp emission intensity was quenched significantly only when the quencher moiety was located close to the surface of the bilayer, suggesting that D4 is not deeply inserted into the bilayer and is peripheral to the membrane. Yet these experiments provided only little information on the orientation of D4 on the membrane surface and did not reveal what regions of its β-sandwich structure, other than the perceived Trp-rich undecapeptide loop, came into contact with the membrane bilayer. Hence, in the absence of detailed structural information, the exact role of D4 in the pore formation process is unknown.

Heuck et al. (2000) also compared the kinetics of the D4-specific change in Trp emission intensity upon membrane binding and the D3-specific change in NBD-emission intensity when a probe attached to a membrane-facing TMH residue is inserted into the bilayer. These experiments demonstrated that D4-membrane interactions preceded the insertion of D3 TMHs into the membrane. They also showed that substitution of D3 TMH residues with Cys altered the rate of D4 binding to the membrane surface, even though D4 interacts first with the membrane. Furthermore, when insertion of the D3 TMHs was prevented by an engineered intramolecular disulfide bond between a TMH residue and D2, D4-membrane binding proceeded to completion. These data thereby revealed that the spatially-separated D3 and D4 are conformationally coupled. Thus, pore formation was shown to be accomplished by sequential and ordered conformational changes that extended throughout the CDC molecule.

Mechanism of CDC pore formation

A contentious issue that sparked widespread debate among researchers in the field involved the mechanism of assembly of the CDC oligomeric pore complexes in the membrane bilayer. Two conceptually different models were proposed for the mechanism of CDC pore formation.

Palmer et al. (1998), based on the extremely large size of the SLO pore, the perceived heterogeneity of the SLO oligomer, and the existence of arc-shaped pore structures in electron microscopy images of membrane-bound SLO, suggested that membrane insertion of a CDC molecule preceded its oligomerization. According to their model, CDC pore formation is triggered by the initial insertion of a dimer that serves a nucleus for oligomerization. Subsequent elongation of the inserted dimer by the insertion of individual monomers that rapidly associate yields a 'growing' arc-shaped pore that eventually becomes circular after the arc is completed. Consistent with their model, they provided evidence that the pore size could be manipulated by addition of a SLO mutant that ostensibly capped the ends of a growing oligomer and prevented further oligomerization. However, the 'growing-pore' model posed severe conceptual difficulties because it was not clear how the hydrophilic side of the two TMHs of an individual SLO monomer could be inserted into the nonpolar bilayer and retained in a stable form until pore formation was complete.

In apparent contrast to the growing-pore model, results from four independent studies suggested that the formation of a complete, circular, oligomeric ‘prepore’ complex is obligatory and occurs prior to the insertion of the CDC TM β-barrel.

First, Shepard et al. (2000) demonstrated that the membrane-inserted CDC (PFO) oligomers (~ 2.5 MDa) were resistant to the detergent SDS. They showed that the large SDS-resistant PFO oligomer could be sieved on a SDS-agarose gel (SDS-AGE) and resolved from the monomer. Under low temperature conditions that significantly retarded the rate of insertion of the TMHs, they found that nearly 80% of the PFO monomers were present in SDS-resistant oligomers. The formation of circular prepore complexes prior to TM β-barrel insertion under these conditions was confirmed by a combination of SDS-AGE, electron microscopy, fluorescence spectroscopy, and ion-conductivity measurements in planar bilayers.

Second, Hotze et al. (2001) engineered a reversible, intramolecular disulfide bond in PFO that clamped TMH1 to D2 and showed that the disulfide-trapped molecules formed circular, prepore complexes on the membrane surface in the absence of any TMH insertion.

Third, Hotze et al. (2002) discovered a point mutant of PFO in which substitution of a highly conserved Tyr in D3 (Y181) with a residue other than Phe (Y181A, Y181C) trapped PFO in the prepore state and completely abrogated pore formation. Furthermore, they also showed that the non-functional Y181A mutant could be forced to insert its TM β-hairpins into the membrane in mixed oligomers comprised of a molar excess of functional PFO, demonstrating that monomer-monomer interactions in the prepore complex are necessary to drive TM β-barrel insertion.

Fourth, Heuck et al. (2003) in a recent unprecedented comparative study showed that the CDCs PFO and SLO, when tested under the same conditions, formed only large pores. They demonstrated that the rate and extent of release of liposome-encapsulated markers of molecular dimensions ranging from small (0.6 kD) to large (670 kD) were superimposable under limiting toxin concentrations. These results are inconsistent with the notion of a smaller, rapidly-growing, arc-shaped pore that would be expected to release smaller markers at a faster rate than larger ones. Thus, the CDC pore is formed by the insertion of a large, discrete oligomer of a defined size and not by the growth of a smaller pore into a larger one by the addition of individual molecules.

Pathway for CDC pore formation

From the available data, the general pathway by which CDCs form pores in cholesterol-containing membranes can be delineated:

Water-soluble monomer → Membrane-bound monomer → Membrane-bound prepore complex → Membrane-inserted pore complex (Figure 6).

To briefly summarize each of these steps, membrane-targeting by CDCs is accomplished, presumably by the specific recognition of cholesterol in the membrane by D4. Whether cholesterol serves as a receptor for binding and/or is involved at a later stage in pore formation is still controversial. In synthetic liposomal membranes comprised of a binary mixture of phospholipids and cholesterol, a high amount of cholesterol (> 40 mol%) is absolutely required for binding (Heuck et al., 2000). In RBC membranes, near-depletion of cholesterol by methyl-β-cyclodextrin (MβCD) does not abrogate binding or prepore formation but does block TM β-barrel insertion instead

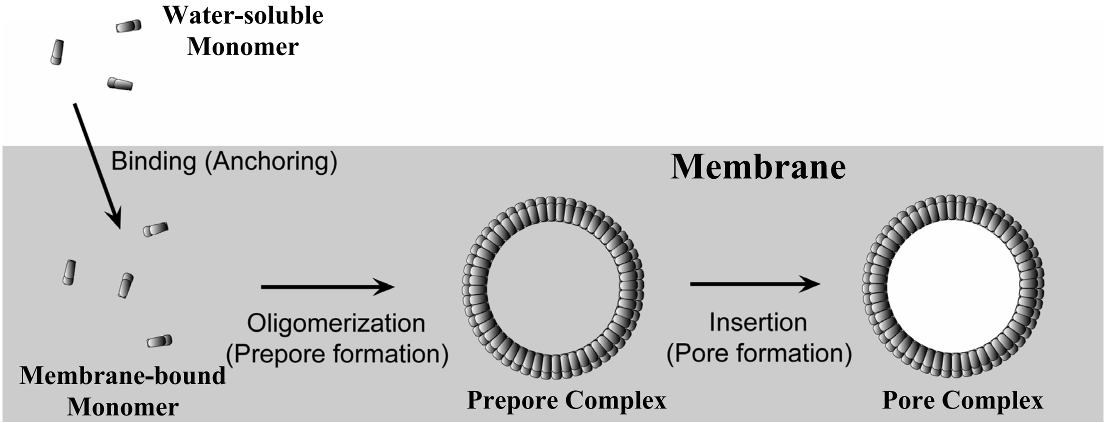
Water-soluble
Monomer
Binding (Anchoring)
Membrane
Oligomerization
(Prepore formation)
Insertion
(Pore formation)
Membrane-bound
Monomer
Prepore Complex
Pore Complex

Figure 6. Top view of the pathway of pore formation by PFO. The gray surface represents intact membrane. The plane of the membrane is the same as the plane of the paper.

(Giddings et al., 2003). Further experimentation is required to clearly resolve this issue.

Stable binding to the target membrane surface presumably triggers conformational changes in the CDC molecule that promote oligomer formation. Subsequent oligomerization of 40-50 monomers into circular, prepore complexes aligns the D3 TMH segments of adjacent monomers and triggers their concerted insertion into the membrane to form a large TM β-barrel. Concomitant with TM β-barrel insertion, by a mechanism that is still unclear, the lipid molecules in the middle of the pore are displaced to create a hole that measures ~ 300 Å in diameter.

Unresolved issues and specific goals of this study

As evident from the above narrative, our current understanding of the mechanism of CDC pore formation is fragmented rather than complete. For example, we do not yet understand the molecular details of the mechanism by which CDCs recognize a cholesterol-containing membrane. Other outstanding questions include the following: How do CDCs prevent premature oligomerization prior to target membrane binding? How does membrane binding trigger oligomerization? What conformational changes are elicited upon membrane binding? Where are the intersubunit interfaces in the CDC oligomeric complex? How are the TMHs of adjacent monomers aligned in proper register for β-barrel insertion? What are the topographical changes in the CDC molecule relative to the target membrane at different stages of pore formation?

In the case of smaller PFTs such as the *S. aureus* α-HL, high-resolution crystallographic structures have provided structural snapshots of the initial and final stages of pore formation, from which a pathway of pore formation has been delineated

(Montoya and Gouaux, 2003). Although high-resolution structures of the intermediate states in CDC pore formation are desirable, realistically speaking, with current limitations and difficulties in obtaining diffraction-quality crystals of membrane proteins, the idea of obtaining one with CDC oligomers that are heterogenous in subunit composition seems far-fetched.

Therefore, in the following studies, using PFO and synthetic lipid vesicles (liposomes) that permit pore formation as models for CDCs and the mammalian cell membrane, respectively, I have employed multiple independent fluorescence spectroscopic techniques as primary tools in answering the above-mentioned questions.

In toto, the combined data from the following studies have helped bridge many of the gaps that exist in our current knowledge of the mechanism of CDC pore formation.

CHAPTER II

EXPERIMENTAL PROCEDURES

Construction of recombinant PFO (rPFO) derivatives

The gene for PFO^{C459A} (hereafter termed rPFO), the cysteine-free, functional derivative of PFO, was subcloned in the bacterial overexpression vector, pRSETB (Invitrogen) from its original vector, pRT20 (Shepard et al., 1998) via its *Bgl* II and *EcoR* I restriction sites (Heuck et al., 2000). The pRSETB vector containing the gene for rPFO was designated pAH21. In pAH21, the ORF of *pfo*^{C459A} encoding amino acid residues 28-500 (residues 1-27 constitute the signal sequence for secretion from *C. perfringens* and are proteolytically removed) is placed under the control of the bacteriophage T7 promoter and fused in-frame to an N-terminal tag encoding 27 residues that include a 6X-polyhistidine stretch for rapid purification of the protein product. The plasmid also provides an ampicillin-resistance cassette as a selectable marker. His-tagged rPFO was found to retain activity comparable to the wild-type (Heuck et al., 2000).

This construct was used as the template for PCR-based site-directed mutagenesis using the Quikchange method (Stratagene). The basic codon replacement procedure utilizes two synthetic, complementary oligonucleotide primers (forward and reverse) containing the desired mutation(s) that anneal to their complementary sequence on opposite strands of the template plasmid except at the site of mutation. Complete extension of these annealed primers during thermal cycling by the high fidelity, thermostable DNA polymerase, *pfuTurbo*, generates a mutation-carrying plasmid with staggered nicks. After treatment of the PCR mixture with *Dpn* I, a restriction enzyme that digests the methylated and hemi-methylated parental template DNA, the reaction mixture is used to transform sub-cloning grade competent bacteria. Cells carrying the repaired, mutated DNA are then selected based on ampicillin-resistance. After isolation of plasmid DNA (QIAGEN miniprep), the presence of the desired mutation(s) and the absence of random mutations in the mutated plasmid are confirmed by automated DNA sequencing.

The mutagenic primers designed were between 25-45 nucleotides in length with melting temperatures (Tm) ranging between 60-80°C. The desired mutation(s) were typically in the middle of the primers. Primers were synthesized and purified by either Sigma-Genosys or Integrated DNA technologies, Inc. (IDT). The PCR reaction was performed in a volume of 50 μl containing 1 μl of template DNA (1 μl of a plasmid miniprep; ~ 30 ng/μl DNA), 1 μl each of forward and reverse mutagenic primers (125 ng of each primer), 1 μl of dNTP mix (50 μM final of each dNTP), 5 μl of 10X reaction buffer [200 mM Tris-HCl (pH 8.8), 100 mM KCl, 100 mM $(NH_4)_2SO_4$, 20 mM $MgSO_4$, 1% (v/v) Triton X-100, 1 mg/ml nuclease-free bovine serum albumin (BSA)], 1 μl of *pfuTurbo* DNA polymerase (2.5 U/μl), and 40 μl of ddH_2O. Thermal cycling parameters were 95°C (30 sec) for denaturation, 55°C (1 min) for annealing, and 68°C (2 min/kb of plasmid; 9 min) for extension. Typically, 16 cycles of PCR were performed for each mutagenesis.

After PCR, the reaction was maintained at 37°C and 1 μl of the restriction enzyme, *Dpn* I (10 U/μl), was added directly to 50 μl of the PCR reaction mixture. This mixture was incubated for 1 hour at 37^{o}C to digest the methylated/hemi-methylated parental template DNA strands. Later, 1 μl of this reaction mixture was transferred to a microfuge tube containing 50 μl of freshly-thawed competent cells (*Escherichia coli* TOP10F', XL-1 blue or MC1061 strains). This transformation reaction was gently mixed, incubated on ice for 30 min, and then heat-pulsed (heat shocked) for 45 sec at 42^{o}C. After the heat-pulse, the mixture was placed on ice for 5 min. Fresh SOC medium (250 μl) was then added to the bacterial suspension and the cells were grown at 37^{o}C for 1 hour with constant shaking (225-250 rpm). Later, 50-100 μl of the transformation mixture was spread on LB-Agar plates containing ampicillin (100 μg/ml) and incubated overnight at 37^{o}C. Three or four colonies of transformed bacteria were picked, grown separately in 3 ml of LB (with 50 μg/ml ampicillin), and their plasmid DNA was isolated using the QIAGEN miniprep kit. The plasmid DNA was eluted in 50 μl of TE buffer [(10 mM Tris-HCl (pH 7.5), 1 mM EDTA)]. For automated DNA sequencing, 5 μl of the plasmid miniprep, diluted two-fold in ddH2O was submitted to Gene Technologies Lab (GTL) at Texas A&M University. Forward or reverse mutagenic primers that were distant to the site of the desired mutation(s) were used as sequencing primers (50 pmol/μl final) and the presence or absence of the desired mutation was confirmed.

Overexpression and purification of rPFO derivatives

rPFO and its derivatives were overexpressed in *E. coli* BL21(DE3)pLysS or BL21(DE3) star (Invitrogen). Both these strains carry the gene for bacteriophage T7 RNA polymerase under control of the IPTG (Isopropyl-β-D-thiogalactopyranoside)–inducible *lac*UV5 promoter. Addition of IPTG induces the overexpression of T7 RNA polymerase, which in turn drives overexpression of the rPFO constructs in pRSETB that are placed under the control of the strong T7 promoter.

Growth of BL21(DE3)pLysS or BL21(DE3) star cells carrying the plasmid for rPFO or its derivatives was initiated with a pilot culture grown overnight in 100 ml sterile LB (50 μg/ml ampicillin). The saturated overnight culture was then used as a 1:20 inoculum for 2 liters of sterile LB (50 μg/ml ampicillin) in a 4-liter flask. The 2 liter-culture was incubated at 37°C with constant shaking for about 3 hours until the OD_{600} reached 0.5-0.6. Expression of rPFO constructs was then induced by the addition of IPTG to a final concentration of 1 mM. The induced culture was incubated further for another 4 hours before the cells were harvested by centrifugation in a Beckman JA-10 rotor at 5000 RPM (RCF 4400 × g) and 4°C.

The following procedures were used for the purification of rPFO derivatives. Minor modifications to the protocol were made in the case of disulfide-bonded rPFO (see note at the end of this section).

The cell pellet from the 2 liter-culture was suspended in 25 ml of buffer A [10 mM MES (pH 6.5), 150 mM NaCl] containing protease-inhibitors benzamidine (0.5 mg/ml final) and PMSF (0.1 mg/ml final). Cell lysis was achieved by two consecutive passages through a French pressure cell (Aminco) at 18,000-20,000 psi (cell pressure). Cell debris was removed by sedimentation at 15,000 RPM (RCF 31,000 × g) in a Beckman JA-17 rotor at 4°C and passage of the supernatant through a 0.45 μm-pore filter. The lysate was then loaded, via a bench-top peristaltic pump, onto a FPLC column (1.5 cm ID × 10 cm; Pharmacia) containing Chelating Sepharose Fast Flow resin (iminodiacetic acid-Sepharose; Amersham) that was preloaded with Co^{2+} and equilibrated with buffer A at room temperature. Preloading of the Chelating Sepharose with Co^{2+} was achieved by passing a 5 mg/ml $CoCl_2$ solution through the resin and washing away the excess unbound metal ions with buffer A.

At pH 6.5, the His-tagged rPFO derivatives bound to the Co^{2+}-resin chelate, while most other contaminating proteins were discarded in the flow-through. To remove unbound contaminants, the resin was washed with 50 ml of buffer A. The column was then transferred to a FPLC (Pharmacia) unit and washed further with 65 ml (2 ml/min) of buffer A. This was followed by a 20 ml (2 ml/min) linear gradient of buffer B [1 M Imidazole (pH 6.5)] from 0 to 50 mM Imidazole to remove loosely-bound contaminants. After a 15 ml (2 ml/min) passage of 50 mM Imidazole, the concentration of Imidazole was raised to 300 mM in one step and His-tagged rPFO or its derivative was eluted in about 40 ml of 300 mM imidazole. The peak fractions were pooled (~ 40 ml) and dialyzed overnight at 4°C against 4 liters of buffer C [10 mM MES (pH 6.5), 1 mM EDTA, 0.5 mM DTT]. After removal of excess imidazole and metal ions by dialysis, the protein solution was loaded directly onto a 1.5 cm ID × 15 cm column containing the cation-exchange resin, sulfopropyl (SP) Sepharose (Amersham), equilibrated with buffer C. A linear gradient (3 ml/min) from 0 to 1 M NaCl eluted purified rPFO or its derivatives in a sharp peak at about 0.7 M NaCl. The fractions containing purified rPFO or its derivatives were pooled (~16 ml) and dialyzed overnight against buffer D [50 mM Hepes (pH 7.5), 100 mM NaCl]. After addition of 5 mM DTT (final), the protein solution was made 10% (v/v) in glycerol, aliquoted into 2 ml cryovials and flash-frozen in liquid nitrogen. The quality of purification was assessed by polyacrylamide gel electrophoresis (PAGE: 12.5% gel) and the concentration of protein was determined by absorbance at 280 nm (A_{280}) using a molar absorptivity coefficient of 74,260 M^{-1} cm^{-1}.

Note: In the case of disulfide-bonded rPFO (T319C V334C) and its derivatives, the bacteria were lyzed under slightly alkaline conditions [50 mM Tris-HCl (pH 8.0), 100 mM NaCl] to promote formation of disulfide bonds. After initial purification by affinity chromatography using Co^{2+}-chelating Sepharose under the same alkaline conditions, the pH was lowered to 6.5 by dialysis against buffer C lacking DTT. Disulfide-bonded rPFO was finally purified to apparent homogeneity by cation-exchange chromatography as described above. No DTT was added to any solution used to purify a disulfide-bonded rPFO derivative. No free sulfhydryls were detected in disulfide-bonded rPFO (T319C V334C) using dithionitrobenzene (Ellman's reagent; Pierce Biotechnology protocol), thereby confirming that nearly all cysteines were engaged in disulfide bonds.

Fluorescent labeling of rPFO derivatives

NBD labeling of rPFO derivatives was done according to procedures described before (Shepard et al., 1998). Briefly, rPFO derivatives (between 5 to 10 μM) in buffer E were reacted with a 10-fold molar excess of IANBD (Molecular Probes; Figure 7), except that only in the case of rPFO(V322C), the reaction was made 3 M in guanidine hydrochloride to facilitate access of the IANBD to the partially-buried cysteine. NBD-labeled rPFO derivatives were separated from the free dye by gel filtration through a Sephadex G-50 column (1.5 cm I.D. × 25 cm) equilibrated with buffer D. The efficiency of labeling was determined spectrophotometrically to be 80-100% [except for

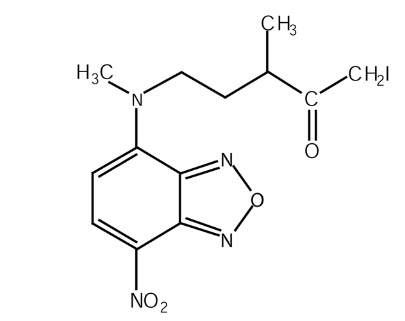
CH3
H3C
N
CH2I
C
O
N
O
N
NO2

N,N'-dimethyl-N-(iodoacetyl)-*N'*-(7-nitrobenz-2-oxa-1,3-diazol-4-yl) ethylenediamine (IANBD)

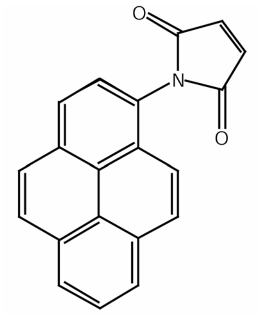

N-(1-pyrene)maleimide

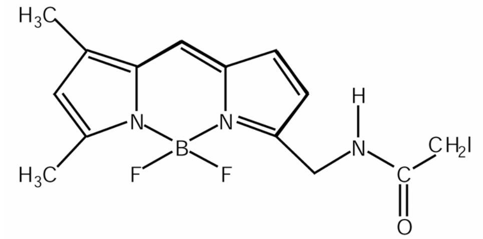
H3C
H3C
N
B
N
F
F
H
N
CH2I
C
O

N-(4,4-difluoro-5,7-dimethyl-4-bora-3a,4a-diaza-s-indacene-3-yl)methyl iodoacetamide (BODIPY FL C_1-IA)

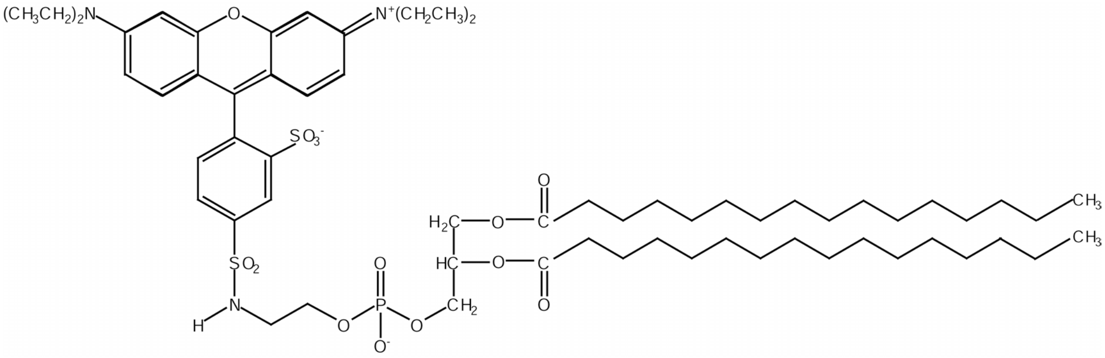
(CH3CH2)2N
O
N+(CH2CH3)2
SO3-
SO2
N
H
O
P
O
O
O-
CH2
HC
H2C
O
C
O
O
C
O
CH3
CH3

Lissamine rhodamine B 1,2-dihexadecanoyl-*sn*-glycero-3-phosphoethanolamine (Rh-PE)

Figure 7. Structures of fluorescent reagents and phospholipid. All fluorophores used in this study were obtained from Molecular Probes Inc.

rPFO(T319C V334C V322C], which was labeled to 30% in the absence of guanidine HCl), by using molar absorptivity coefficients of 74,260 $M^{-1}cm^{-1}$ at 280 nm and 25,000 M^{-1} cm^{-1} at 478 nm for PFO and NBD, respectively.

BODIPY labeling of rPFO derivatives was done similarly by using a 10-fold molar excess of BODIPY® FL C_1-IA (Molecular Probes; Figure 7). The efficiency of labeling was determined spectrophotometrically to be 25-60% by using a molar absorptivity coefficient of 76,000 M^{-1} cm^{-1} at 502 nm for BODIPY.

For pyrene labeling of rPFO(T179C), N-(1-pyrene)maleimide (Molecular Probes; Figure 7), was dissolved in DMSO and added in a four-fold molar excess to PFO in buffer E [50 mM Hepes (pH 8.0), 100 mM NaCl, 1 mM EDTA]; rPFO(V322C) was labeled in buffer B containing 3 M guanidine HCl. After incubation at room temperature for 2 hr, the reaction was quenched by the addition of DTT to a final concentration of 5 mM (except in the case of disulfide-linked derivatives). After removal of precipitated material by sedimentation, the supernatant was passed through a Sephadex G-50 column (1.5 cm I.D. x 25 cm) equilibrated with buffer D to separate pyrene-labeled PFO from the dye-DTT adduct. The efficiency of labeling, determined spectrophotometrically using a molar absorptivity coefficient of 40,000 $M^{-1}cm^{-1}$ at 338 nm for pyrene, was 60-70%, with the exception of rPFO(T319C V334C V322C) (50% labeled; no guanidine HCl in the reaction).

All fluorophore-labeled rPFO derivatives were made 10% (v/v) in glycerol, flash-frozen in small aliquots and stored at -80°C before use.

Preparation of liposomes

Synthetic liposomal membranes comprised of 1-palmitoyl-2-oleoyl-*sn*-glycero-3-phosphocholine (POPC; Avanti Polar Lipids, Inc) and cholesterol (Steraloids, Inc) at a ratio of 45:55 mol% respectively were generated using an Avestin Inc. Liposofast extruder and polycarbonate membranes (Whatman) of 100 nm pore diameter as described previously (Heuck et al., 2003). Briefly, the mixture in chloroform was dried and spread uniformly as a thin layer on the walls of a glass test tube by placing the solution under a stream of N_2 gas at 37^{o}C. To remove any traces of chloroform, the lipid mixture was further dried under vacuum at 37^{o}C for an additional 3 hours. The thoroughly dried lipid mixture was then resuspended in pre-warmed (37^{o}C) buffer D for 30 min and vortexed thoroughly to remove lipids from the test tube wall and ensure their complete hydration. The volume of buffer D added to the dried lipid mixture was adjusted to yield a final lipid concentration of 5 mM (2.25 mM POPC; 2.75 mM cholesterol). The resuspended lipid mixture was subjected to 3 consecutive freeze/thaw cycles, and passed 21 times through a 100 nm polycarbonate membrane in a liposome extruder to generate large unilamellar liposomes. The liposomes were stored at 4^{o}C and used within a week of production.

Liposomes used in lipophilic quenching experiments were prepared using POPC and cholesterol in the same way, except that 10 mol% of the POPC was substituted with a nitroxide-labeled (spin-labeled) phospholipid, 1-palmitoyl-2-stearoyl-(12-doxyl)-sn-glycero-3-phosphocholine (12-doxyl-PC; Avanti polar lipids, Inc), where the nitroxide moiety is covalently attached to the 12th carbon in the acyl chain of the phospholipid.

Similarly, in liposomes used in FRET experiments, 1, 1.5 or 2 mol% of the total lipid was replaced with Rh-PE (Molecular Probes; Figure 7).

Assay for pore formation

Cholesterol-containing liposomes were prepared as above except that the dried lipid mixture was resuspended in buffer D containing 3 mM $TbCl_3$ and 9 mM dipicolinic acid (DPA). Tb^{3+} (a lanthanide metal ion) and DPA together form a highly-fluorescent $[Tb(DPA)_3]^{3-}$ complex. Free $[Tb(DPA)_3]^{3-}$ was separated from liposome-encapsulated $[Tb(DPA)_3]^{3-}$ by passing the mixture over a Sephadex G-50 column (1.5 cm ID x 25 cm) in buffer D at room temperature. The ability of unlabeled and fluorophore-labeled rPFO derivatives to form pores in cholesterol-containing liposomes was determined by measuring the release of the encapsulated $[Tb(DPA)_3]^{3-}$ complex into an external solvent containing 5 mM EDTA. EDTA binds tightly to Tb^{3+} and quenches its fluorescence by displacing DPA from the $[Tb(DPA)_3]^{3-}$ complex. Briefly, cholesterol-containing liposomes (50 μM total lipid) encapsulating the $[Tb(DPA)_3]^{3-}$ complex were resuspended in buffer D containing 5 mM EDTA (pH 7.5) and placed in a temperature-controlled (25°C or 37°C as noted) cuvette (1 cm x 1 cm quartz) under constant stirring using a magnetic stir bar (1.5 mm X 8 mm). After thermal stabilization and complete mixing of the sample (5 min), the initial intensity (F_0; zero time point) was determined. Then, the ability of rPFO derivatives (50 nM final) to form pores in these vesicles was determined by measuring the decrease in terbium emission intensity as a function of time, starting 15 sec after toxin addition. The samples were excited at 278 nm (2 nm bandpass) and emission was monitored at 544 nm (2 or 4 nm bandpass) every 30 sec for the entire time course of the experiment. Emission was monitored through an Oriel 5215 filter (0% transmittance below 350 nm) to remove second-order excitation light.

Steady-state fluorescence spectroscopy

Steady-state fluorescence measurements were made using an SLM 8100 photon-counting spectrofluorometer with a 450 W xenon lamp light source, a double monochromator in the excitation light path, a single emission monochromator, and a Peltier-cooled PMT housing. Either 4 mm × 4 mm or 1 cm × 1 cm stoppered quartz cuvettes (Starna Cells, Inc) were used to house the samples for fluorescence measurements.

For single-wavelength fluorescence measurements, the following excitation and emission wavelengths were used for the various fluorophores used in this study: Trp (λ_{ex} = 295 nm, λ_{em} = 348 nm), pyrene excimer (λ_{ex} = 345 nm, λ_{em} = 470 nm), NBD (λ_{ex} = 470 nm, λ_{em} = 530 nm), BODIPY (λ_{ex} = 490 nm, λ_{em} = 510 nm); the band-pass was either 2 or 4 nm for both excitation and emission. Typically, five 5-second integrations of emission intensity at a particular wavelength were taken in sequence and averaged to yield the recorded intensity measurement.

For the acquisition of time-dependent emission intensity profiles for Trp and NBD, a sample containing rPFO or a derivative (final concentration 50 nM) in buffer D was stirred and temperature-equilibrated in a cuvette (1 cm x 1 cm quartz) before its initial intensity (F_0; zero time point) was determined. Cholesterol-containing liposomes (50 μM total lipid) were then added to the sample, and data collection begun 15 sec later as above. Blank measurements were made using an otherwise identical sample that lacked the fluorophore. The blank data were subtracted from the corresponding sample data, and F_0 was corrected for dilution.

Fluorescence emission spectra for NBD and pyrene-labeled rPFO derivatives were recorded in either 4 mm x 4 mm or 1 cm × 1 cm quartz cuvettes under the same conditions described above. NBD was excited at 470 nm (4 nm bandpass) and emission intensity was measured between 500 nm and 600 nm (4 nm bandpass) at 1 nm intervals, while pyrene was excited at 345 nm (2 nm bandpass) and emission intensity was monitored between 360 nm and 550 nm (4 nm bandpass) at 1 nm intervals.

To prevent photodegradation of the fluorescent probes, samples were stored in the dark prior to use. In the fluorometer, shutters in the light path were kept closed until data collection began.

Collisional quenching by iodide ions

The extent of collisional quenching of NBD emission intensity by iodide ions was determined using the titration method as described before (Shepard et al., 1998). In this method, two equivalent samples containing NBD-labeled rPFO in buffer D at 25^{o}C were titrated in parallel under constant stirring, one with 1 M KI and 1 mM $Na_2S_2O_3$ and the other with 1 M KCl and 1 mM $Na_2S_2O_3$ to yield final KI and KCl concentrations between 20 and 100 mM (5 points; 20, 40, 60, 80 and 100 mM) in the sample solution. Two equivalent control samples that lacked the NBD dye were also titrated in parallel with the same solutions and served as blanks in the experiment. The initial net fluorescence intensity for each sample (F_0) was obtained prior to the addition of any KI or KCl by subtracting the background signal and light scattering of a corresponding blank sample from its corresponding NBD-containing sample. After each addition of KI or KCl to a sample and its control, the emission intensities were measured and dilution-corrected to obtain the net emission intensity (F). The net change in fluorescence due to quenching at each iodide ion concentration was then normalized using the equation:

$F_0 / F = [(F_0 / F)_{KI} / (F_0 / F)_{KCl}]$

The resultant data were then analyzed according to the Stern-Volmer law for collisional quenching of fluorescence, which is mathematically stated as:

$F_0 / F = 1 + K_{sv} [Q] = 1 + k_q \tau_0 [Q]$,

where K_{sv} is the Stern-Volmer quenching constant and Q is the concentration of the quencher. K_{sv} is equal to $k_q\tau_0$, where k_q is the bimolecular quenching constant and τ_0 is the fluorescence lifetime in the absence of quencher. k_q was determined by a linear least-squares analysis of $(F_0/F-1)/\tau_0$ values at five different $[I^-]$ from at least three independent experiments. The slope of the plot yields k_q. An example Stern-Volmer plot is shown in Figure 8.

Quenching by spin-labeled phospholipids

The emission intensities of two equivalent samples of monomeric NBD-labeled rPFO (50 nM) in buffer D were measured at 10°C (F_{buff}), and then excess cholesterol-containing liposomes (50 µM total lipid) with or without nitroxide-labeled phospholipids were added to the sample. After incubation of the mixture at 37°C for 30 min to allow pore formation, the samples were brought back to 10°C, and the NBD emission intensities were redetermined (F_{memb}). The blank-subtracted, dilution-corrected intensities were normalized (F_{memb}/F_{buff}) to account for the differences in the NBD

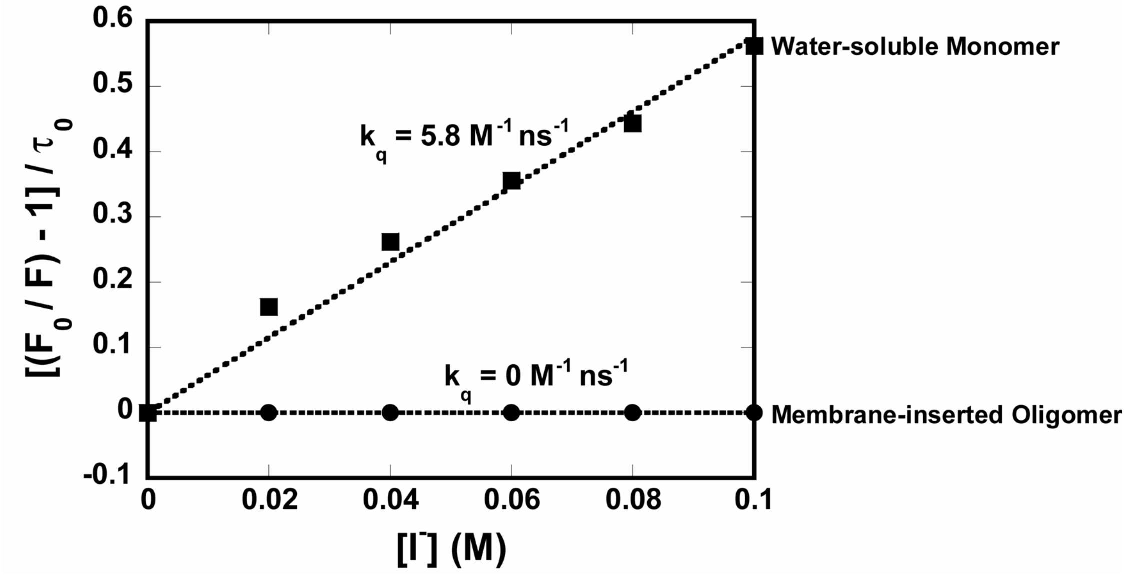

Figure 8. Analysis of iodide ion quenching by the Stern-Volmer equation. Iodide ion quenching of water-soluble (■) or membrane-inserted rPFO(V403C-NBD) (●) was analyzed according to the Stern-Volmer equation: $F_0/F = 1 + k_q\tau_0\ [Q]$, where F_0 is the emission intensity in the absence of quencher and F is the emission intensity in the presence of iodide ions at concentration [Q]. k_q is the bimolecular quenching constant and τ_0 is the fluorescence lifetime in the absence of quencher. A linear least-squares analysis of $(F_0/F\text{-}1)/\tau_0$ values at five different $[I^-]$ yielded the value of k_q (slope).

content of each sample. From these data, F/F_0 was calculated, where F_0 was the normalized NBD emission intensity in the nitroxide-lacking sample and F was the normalized NBD emission intensity in the nitroxide-containing sample. In the absence of quenching, F/F_0 equals ~ 1, while in the presence of quenching, $F/F_0 <1$.

Time-resolved fluorescence spectroscopy and data analysis

Fluorescence lifetime measurements were made using an ISS (Urbana, IL) K2-002 multi-frequency cross-correlation phase and modulation spectrofluorometer (Spencer and Weber, 1969). Samples were excited in 1 cm × 1 cm quartz cuvettes using the 457 nm or the 488 nm line of a Coherent (Santa Clara, CA) Innova 400-15/3 argon ion laser, and fluorescence emission was monitored through an Oriel OG-515 filter (0% transmittance of light with wavelengths less than 515 nm). To eliminate polarization artifacts (due to the effects of anisotropy on the intensity decay), magic-angle conditions were used in which the excitation light was passed through a vertically-oriented (0^o) Glan-Taylor polarizer and emitted light collected through a Glan-Thompson polarizer oriented at 54.7^o relative to the vertical axis (Spencer and Weber, 1970). No blank subtraction was done since scatter due to the presence of liposomes (both Raman and Rayleigh) was always less than 10% of the signal. For NBD lifetime measurements, disodium fluorescein (reference grade; Molecular Probes) in 0.1 M NaOH (τ = 4.05 ns) was used as the reference standard.

Typically, samples containing 50-500 nM NBD-labeled rPFO derivatives in buffer D were incubated, either with or without an excess of cholesterol-containing liposomes (PFO/lipid molar ratio, 1/1000), at 37°C for 45 min and then cooled to 25°C for 10 min before measuring the NBD lifetimes.

The phase and modulation data were analyzed using the computer program, GLOBALS UNLIMITED (University of Illinois, Urbana, IL) to compute the lifetime and mole fraction of dyes in each sample. Data were best fit (had the lowest χ^2) to intensity decay models comprised of two components, either two discrete exponentials or one discrete exponential and one Lorentzian distribution. The latter adds an additional parameter corresponding to the half-width of the distribution. Fitting the data to three component models did not significantly improve the fit. Fractional contributions of each computed lifetime, expressed as pre-exponential factors, were interpreted to equal the relative mole fractions of NBD probes in the two environments (Crowley et al., 1993).

FRET parameters, measurements and data analysis

Calculation of acceptor density

The surface density of Rh-PE molecules in acceptors per square angstrom, σ, was calculated by assuming that each cholesterol molecule occupies 37 Å^2 of surface area, and each phospholipid molecule 48 Å^2 of surface area in the presence of an equimolar ratio of cholesterol (Lecuyer and Dervichian, 1969). Thus,

$\sigma = [\text{Rh-PE}] / \{([\text{Phospholipid}] \times 48 \text{ Å}^2) + ([\text{Cholesterol}] \times 37 \text{ Å}^2)\}$.

Rh-PE concentrations of 1, 1.5 and 2 mol% yielded σ values of 2.4×10^{-4}, 3.6×10^{-4}, and 4.8×10^{-4} per Å^2, respectively.

Determination of quantum yield Q_D

The quantum yields of water-soluble and oxidized rPFO(T319C V334C E167C-BODIPY) and rPFO(T319C V334C A215C-BODIPY), hereafter abbreviated as rPFO^{DS}(E167C-BODIPY) and rPFO^{DS}(A215C-BODIPY) to denote the intramolecular disulfide bond, were determined using the relationship:

$$Q_1 / Q_2 = (F_1 / F_2)\ (A_2 / A_1) \qquad \text{(Eq. 1)}$$

where Q_1 is the quantum yield of unreduced rPFO^{DS}(E167C-BODIPY) or rPFO^{DS}(A215C-BODIPY) in buffer D and Q_2 is 0.92, the quantum yield of disodium fluorescein (Molecular Probes reference grade) in 0.1 M NaOH (Weber and Teale, 1957). F_1 and F_2 are the integrated areas of the corrected emission spectra of the rPFO^{DS}(E167C-BODIPY) or rPFO^{DS}(A215C-BODIPY) and disodium fluorescein samples, respectively, recorded between 470-700 nm while A_1 and A_2 are the respective absorbances of the samples in their corresponding solvents at the exciting wavelength of 460 nm.

Determination of R_0

R_0, the distance between a donor dye (D) and an acceptor (A) dye that yields a FRET efficiency of 50% was determined for BODIPY-labeled rPFO and Rh-PE in cholesterol-containing membranes using the equation:

$$R_0^6 = (8.79 \times 10^{-5})\ \kappa^2 n^{-4} Q_D J_{DA} \qquad \text{(Eq. 2)}$$

where R_0^6 is in Å^6, J_{DA} is the spectral overlap integral in M^{-1} cm^{-1} nm^4, Q_D is the quantum yield of unreduced rPFO^{DS}(E167C-BODIPY) or rPFO^{DS}(A215C-BODIPY) in the absence of energy transfer, n is the refractive index of the medium between the D and A dyes, and κ^2 is a geometric factor that depends upon the relative orientation of the D and A dyes (discussed in Results). The absorbance spectrum of Rh-PE in cholesterol-containing membranes and the corrected emission spectrum of the BODIPY dye in rPFO^{DS}(A215C-BODIPY) were recorded in buffer D at 1-nm intervals. J_{DA} was then determined using

$$J_{DA} = \int F_D(\lambda)\, \varepsilon_A(\lambda)\, \lambda^4\, d\lambda \,/ \int F_D(\lambda)\, d\lambda\,, \qquad \text{(Eq. 3)}$$

where $F_D(\lambda)$ is the corrected net emission intensity of rPFO^{DS}(A215C-BODIPY) at a given wavelength and $\varepsilon_A(\lambda)$ is the molar extinction coefficient of Rh-PE at the same wavelength. Using a molar extinction coefficient of 80,000 M^{-1} cm^{-1} at 567 nm for Rh-PE, J_{DA} was determined to be 2.05×10^{15} M^{-1} cm^{-1} nm^4. The emission spectra of all BODIPY-labeled rPFO derivatives had the same shape (λ_{max} = 511 nm) and yielded the same J_{DA} values at all stages of pore formation. The spectral overlap of rPFO^{DS}(A215C-BODIPY) and Rh-PE in cholesterol-containing membranes is shown in Figure 9.

Assuming values of 1.4 and 2/3 for n and κ^2, respectively (Johnson et al., 1982; Mutucumarana et al., 1992; Yegneswaran et al., 1997), R_0 for FRET between rPFO derivatives labeled with BODIPY at position 167 and Rh-PE in cholesterol-containing membranes was determined to be 52.2 Å, while that R_0 for FRET between rPFO derivatives labeled with BODIPY at position 215 and Rh-PE was 53.4 Å. As discussed below and in Woolhead et al. (2004), it is reasonable to use κ^2=2/3 to calculate R_0.

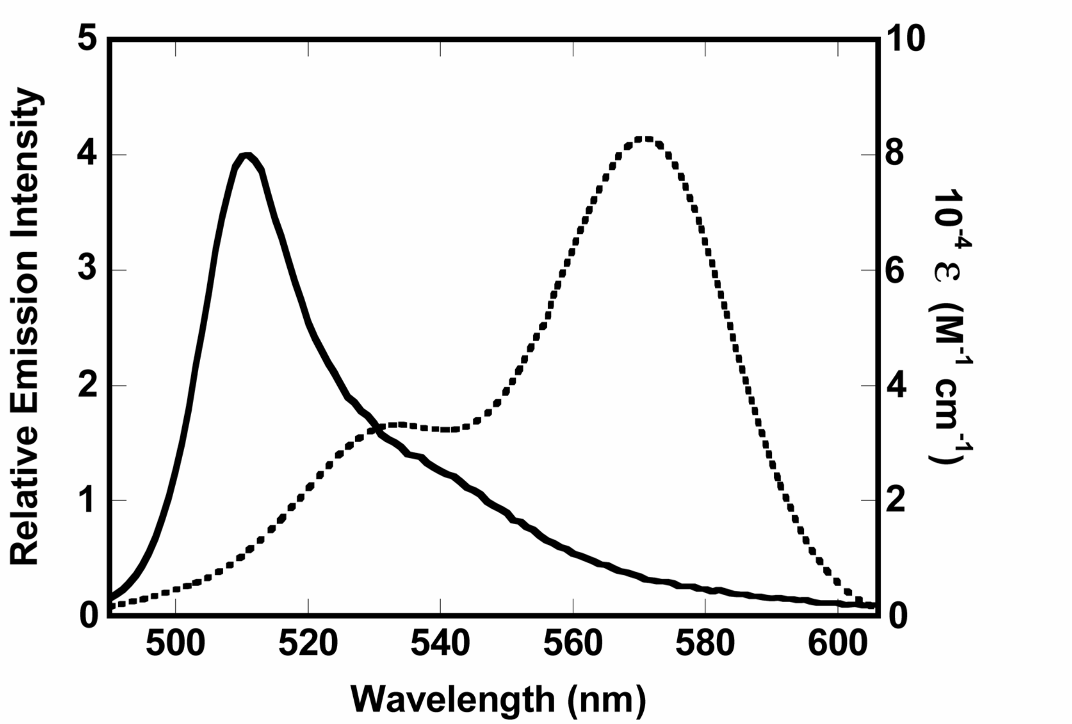

Figure 9. Spectral overlap of BODIPY and Rh-PE. The corrected emission spectrum of 6 nM rPFO^{DS}(A215C-BODIPY) (solid line) and the absorbance spectrum of Rh-PE (2 mol%) (dotted line) incorporated into cholesterol-containing membranes (0.5 mM total lipid), both in buffer D were recorded at 1 nm-intervals. The molar extinction coefficient for Rh-PE is 80,000 M^{-1} cm^{-1} at 567 nm. The spectral overlap integral J_{DA} was determined to be 2.05×10^{15} M^{-1} cm^{-1} nm^4.

Steady-state anisotropy

Steady-state anisotropies of BODIPY and rhodamine were measured in buffer D at 25°C using BODIPY-labeled rPFO derivatives bound to vesicles lacking Rh-PE and unmodified rPFO derivatives bound to Rh-PE-containing vesicles, respectively. The L-format was used with Glan-Thompson prism polarizers in both the excitation and emission beams as described previously (Mutucumarana et al., 1992). The emission intensity measured when a sample was excited by vertical plane-polarized light, and the emission detected through a horizontal polarizer was designated as I_{VH}. I_{VV}, I_{HV}, and I_{HH} were defined analogously. The component intensities of a dye-free blank sample containing the same concentrations of unmodified rPFO bound to vesicles that lacked Rh-PE were subtracted from the corresponding component intensities of the sample to obtain the net emission intensities of BODIPY-labeled rPFO derivatives and Rh-PE.

The fluorescence anisotropy (r) was then calculated using the equation:

$$r = (I_{VV} - GI_{VH}) / (I_{VV} + 2GI_{VH}), \qquad \text{(Eq. 4)}$$

where the grating factor $G = I_{HV} / I_{HH}$. λ_{ex} and λ_{em} were 490 nm and 510 nm for BODIPY-labeled rPFO and 570 nm and 590 nm for Rh-PE.

To eliminate homo-FRET between closely-spaced BODIPY-labeled rPFO in a membrane-bound oligomer that would reduce the fluorescence anisotropy, a mixture containing 6 nM of BODIPY-labeled rPFO and 94 nM of the corresponding unlabeled species (as in the FRET measurements) was incubated with cholesterol-containing membranes to spatially separate the labeled rPFO molecules in the oligomer. In experiments not shown, we determined that the anisotropy values do not change when the ratio of unlabeled-to-labeled PFO is increased above 12:1. Similarly, to avoid homo-FRET effects, we measured the anisotropy of Rh-PE using a σ of 0.6×10^{-4}/Å^2 (0.25 mol%), a surface density considerably lower than that used in the FRET measurements.

Energy transfer measurements

Four biochemically-equivalent samples were prepared in parallel for each energy transfer measurement: sample D (donor only) contained 6 nM of a BODIPY-labeled rPFO mutant and 94 nM of the corresponding unlabeled rPFO incubated with membranes lacking Rh-PE; sample DA (donor + acceptor) contained the same protein mixture incubated with cholesterol-containing membranes containing Rh-PE; sample A (acceptor only) contained 100 nM of the unlabeled rPFO mutant and Rh-PE-containing membranes; and sample B (blank) contained 100 nM of the same unlabeled rPFO derivative with membranes that lacked Rh-PE. In all four samples, the total lipid concentration of the cholesterol-containing membranes was 100 μM, and the concentration of Rh-PE was the same in DA and A. All samples were incubated at 37^{o}C for 15 min to permit complete binding of rPFO derivatives to, and in some cases insertion into, the cholesterol-containing membranes.

The net intensity of D, DA, or A (F_D, F_{DA}, and F_A, respectively) was obtained by subtracting the blank signal (F_B). The blank signal never exceeded 1% of the emission intensity of the D or DA samples. To correct for any signal in the DA sample caused by direct excitation of the acceptor, the net blank-corrected F_A was subtracted from F_{DA}. Making the reasonable assumption that the presence of the donor dye does not perturb the absorptivity of the distant acceptor dyes, the ratio of the donor quantum yields in the absence and presence of the acceptor is then given by:

$$Q_D / Q_{DA} = F_D / (F_{DA} - F_A). \qquad \text{(Eq. 5)}$$

Calculation of the distance of closest approach L

When the extent of energy transfer between randomly and uniformly distributed D dyes in one infinite plane and randomly and uniformly distributed A dyes in a parallel infinite plane is small, the first term in the approximate series solution of Dewey and Hammes can be used for calculating the distance of closest approach between the D and A dyes (i.e., the distance between the two infinite planes) (Dewey and Hammes, 1980). The measured Q_D/Q_{DA} values were therefore used to calculate L between BODIPY attached to rPFO mutants and Rh-PE dyes located at the membrane surface using:

$$Q_D / Q_{DA} = 1 + (\pi\, \sigma\, R_0^2 / 2)\, (R_0 / L)^4. \qquad \text{(Eq. 6)}$$

Q_D/Q_{DA} values from multiple independent experiments were plotted as a function of the product of σ and R_0^2. These combined data were analyzed using linear least-squares regression analysis and from the slope of the plot, which is equivalent to $\pi R_0^4/2L^4$, L was determined. Use of eq. 6 is justified only when $L > R_0$ (Baird and Holowka, 1985). In those instances, the extent of energy transfer to the acceptor dyes at the inner surface of the 50-Å-thick phospholipid bilayer is negligible and has not been included in our calculations.

Chemical crosslinking and SDS-AGE

Chemical crosslinking of rPFO derivatives with the homobifunctional amine-crosslinker glutaraldehyde (Sigma) and denaturing agarose gel electrophoresis in the presence of SDS (SDS-AGE) were performed as described previously (Shepard et al., 2000), except that agarose (GeneMate) was used at a final concentration of 2% (w/v). Briefly, samples containing 0.4 to 2 μM NBD-labeled rPFO were incubated with an excess of liposomes (PFO/lipid molar ratio 1/1000) at 37^{o}C for 30 min in buffer D. After the incubation, one-half of each sample received 5 mM glutaraldehyde for 2 min at room temperature before the reaction was quenched by the addition of 1 M urea (final), whereas the other half received no glutaraldehyde. The samples were then solubilized with SDS-sample buffer [50 mM Tris.HCl (pH 6.8), 0.6% (w/v) SDS, and 15% (v/v) glycerol (all concentrations final)**,** with a trace of bromophenol blue] and resolved in a 2% (w/v) SDS-agarose gel in SDS-gel reservoir buffer [50 mM Trizma Base, 400 mM glycine, 0.125% (w/v) SDS]. The gel was run at 100 V for 30 min and the resolved protein bands were visualized either by Coomassie blue staining or by NBD emission (for NBD-labeled rPFO) by exciting and scanning the gel with the 488 nm laser line of the Bio-Rad Molecular Imager FX.

CHAPTER III

MEMBRANE-ANCHORING MECHANISM OF PFO*

Introduction

A fundamental issue associated with the mechanism of action of any pore-forming protein is the identity and structure of the polypeptide that inserts into the membrane and forms the interface between the aqueous pore and the nonpolar lipid bilayer. Early studies with PFO showed that a proteolytically-derived C-terminal fragment (residues 304-500) is able to interact with both the target membrane and intact PFO molecules on the membrane surface (Iwamoto et al., 1990; Tweten et al., 1991). In addition, some of the six Trp residues within this fragment come into contact with the core of the membrane bilayer (Nakamura et al., 1995; Nakamura et al., 1998). Also, amino acid substitutions in a highly-conserved 11-residue sequence (residues 458-468) dramatically inhibit PFO pore formation (Sekino-Suzuki et al., 1996). The three-dimensional structure of the water-soluble PFO monomer was subsequently determined, and the C-terminal portion of PFO (residues 391-500, designated D4) was found to fold into a separate β-sandwich domain comprised of two four-stranded β-sheets at one end of the elongated protein (Rossjohn et al., 1997) (Figure 5).

Based largely on the location of D4 in monomeric PFO and on the above biochemical and genetic data, Rossjohn *et al.* (1997) proposed that D4 undergoes a conformational change and inserts completely into the bilayer to form the lipid-water

---

*Reprinted with permission from Ramachandran, R., Heuck, A.P., Tweten, R.K., and Johnson, A.E. (2002). Structural insights into the membrane-anchoring mechanism of a cholesterol-dependent cytolysin. Nat. Struct. Biol. *9*, 823-827.

interface of the aqueous pore in the membrane-inserted oligomer.

However, recent studies have unequivocally demonstrated that six short α-helices in D3 unfold to form two TM β-hairpins, designated TMH1 and TMH2 (Figure 5). These TMHs then join with those of other PFO molecules in the oligomer to create the TM β-barrel that defines the pore. Although D4 does not contribute to this β-barrel, other studies have shown that D4 interacts directly with the membrane (Iwamoto et al., 1990; Tweten et al., 1991; Nakamura et al., 1995; Heuck et al., 2000). Thus, there has been great interest in the nature of the interactions of D4 with the membrane and with neighboring monomers in the oligomeric complex.

We have recently shown that pore formation requires the sequential and coupled interaction of D4 and the spatially-separated D3 (residues 179-228 and 275-349) of PFO with the target membrane. Kinetics experiments using domain-specific fluorescent probes showed that D4 at one end of the elongated PFO monomer (Figure 5) interacts first with the membrane, yet mutations in D3 can alter the rate of the D4-membrane interaction (Heuck et al., 2000). This discovery raises important structural issues. Since D4 binds first to the membrane, how does the molecule reorient to allow the TMHs to insert into the bilayer during pore formation (Figure 5)? Does D4 also insert into the membrane? Is PFO oriented parallel to the membrane in the complex, with D4 lying along the membrane surface, to position the TMHs in D3 at the membrane surface? Is D4 involved in monomer-monomer interactions during the highly cooperative pore formation process (Hotze et al., 2002)?

As a first step toward addressing the above questions, we have determined the topography of D4, the domain responsible for PFO recognition of cholesterol at a membrane surface, using multiple independent fluorescence techniques. Our data reveal that: D4 does not span the membrane; only the tip of the D4 β-sandwich is exposed to the nonpolar core of the bilayer; D4 projects out of the surface instead of lying along it; and contact areas between D4 and adjacent monomers, if any, are small.

Results

Experimental approach

Site-specific fluorescence labeling and various fluorescence spectroscopic techniques have been used successfully to identify regions of the PFO polypeptide that span the membrane bilayer (Shepard et al., 1998; Shatursky et al., 1999). In this approach, a single amino acid residue in a cysteine-free protein is replaced with a cysteine and its sulfhydryl moiety is covalently modified with the water-sensitive fluorophore, NBD (Figure 7). After ensuring that the function of the protein is not compromised by mutagenesis and/or modification, the spectral properties of the fluorescent dye are monitored before and after association of the labeled protein with the target membrane. Movement of the NBD dye from an aqueous milieu to a hydrophobic environment, such as the core of a membrane bilayer, is characterized by a dramatic increase in NBD fluorescence lifetime (τ) from about 1 ns in water to more than 7 ns in the interior of the membrane (Crowley et al., 1993). This spectroscopic technique therefore allows one to ascertain the environment of the residue to which the dye is attached, both before and after pore formation (Heuck and Johnson, 2002).

Here, a single cysteine was introduced, one at a time, at 12 different locations on

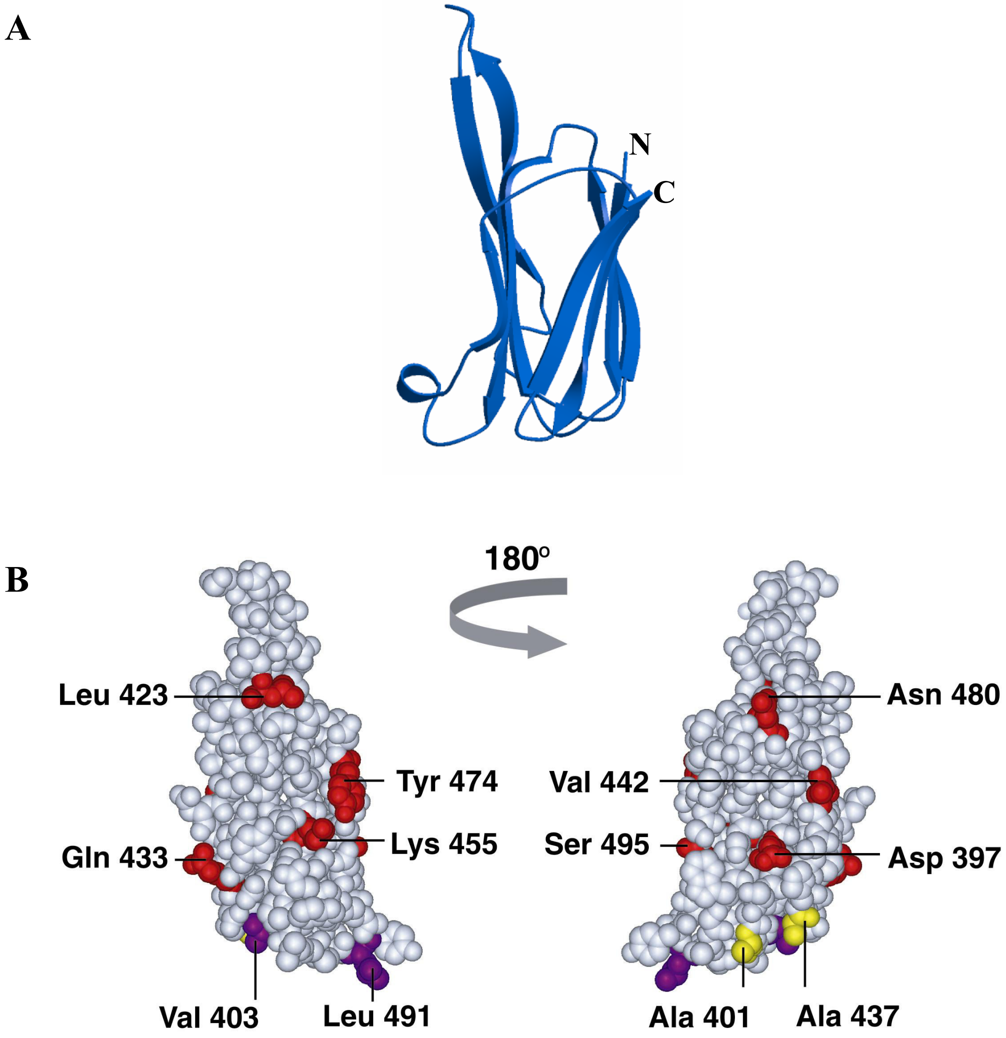
A
N
C
B
180°
Leu 423
Tyr 474
Gln 433
Lys 455
Val 403
Leu 491
Asn 480
Val 442
Ser 495
Asp 397
Ala 401
Ala 437

Figure 10. D4 probe locations. D4 is shown in a ribbon representation (A) and two space-filled representations rotated 180° relative to each other (B). Residues substituted with Cys to attach the NBD fluorophore are highlighted in (B): 397, 423, 433, 442, 455, 474, 480, and 495 in red; 403 and 491 in purple; and 401 and 437 in yellow. Probe position corresponds to the residue number in the polypeptide chain. The images were generated using InsightII (Accelrys).

the surface of D4 (Figure 10) in a derivative of PFO that lacks the single natural cysteine, PFO (C459A), hereafter termed rPFO. The single cysteine in each rPFO mutant was then covalently modified with NBD. The pore-forming activities of NBD-labeled forms of each of the rPFO mutants, assayed by monitoring the leakage of liposome-encapsulated $[Tb(DPA)_3]^{3-}$ (see Experimental Procedures), were comparable to that of the parent toxin, rPFO, with the exception of rPFO(L491C) that formed pores slowly with or without the NBD modification (Appendix, Figure 32).

D4 does not span the bilayer

Time-resolved fluorescence measurements revealed the environments of NBD dyes at various locations on the surface of D4 both before and after pore formation (Figure 11). We observed that the fluorescence lifetime of probes located at positions 401, 403, 437 and 491 of PFO, each located in a loop at the tip of the molecule (Figure 10, yellow and violet), were short (0.5-0.8 ns) in the water-soluble monomer, but were long (> 7 ns) in the membrane-inserted oligomer. Thus, these probes moved from an aqueous milieu into a hydrophobic environment during pore formation in cholesterol-containing liposomes. In contrast, the short fluorescence lifetimes of probes placed at eight other positions on the D4 surface (397, 423, 433, 442, 455, 474, 480 and 495) did not change significantly (Figure 10, red). Hence, these probes were still in an aqueous milieu following pore assembly. However, since a nonpolar environment could be provided either by the hydrophobic core of the membrane bilayer or within a hydrophobic monomer-monomer interface of the oligomeric complex, further experiments were necessary to ascertain the exact location of the probes.

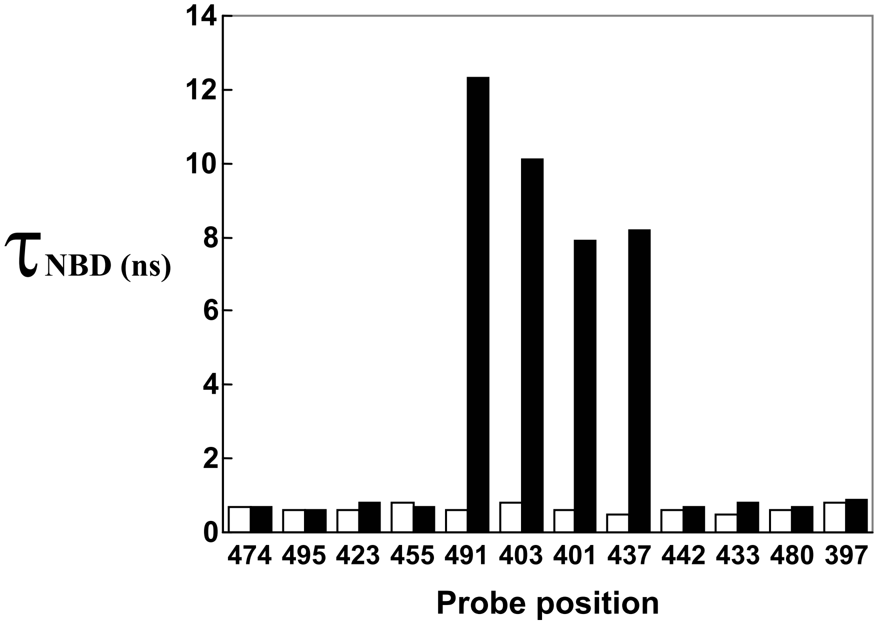

Figure 11. D4 Probe environments. Fluorescence lifetimes of NBD probes in water-soluble monomeric PFO (□) and membrane-inserted oligomeric PFO (■) were measured and analyzed as described in Experimental Procedures. In the case of the water-soluble monomer, the data were best fit (i.e., had the lowest χ^2) to two discrete lifetimes. For the membrane-inserted oligomer, the data were best fit to two lifetimes consisting either of two discrete exponentials or of a Lorentzian distribution and a discrete exponential. Only the major lifetime component (mole fraction > 80%) is shown here for both the monomer and the oligomer. A minor lifetime component that ranged between 1.7-4.3ns represents probes that are dynamically exposed to different environments within the protein. The half-widths of the Lorentzian distributions in the analyses (only for probe positions 401, 403, 437 and 491) were less than 2.4 ns.

Only the tip of D4 is exposed to the membrane core

Collisional quenching of fluorescence is a direct method for determining whether the fluorophore and the quencher are co-localized because no quenching will be observed if the quencher cannot access and collide with the fluorophore (Crowley et al., 1994; Hamman et al., 1998; Heuck and Johnson, 2002). For example, an NBD probe that is embedded in the hydrophobic core of the bilayer will be accessible to membrane-restricted quenchers, such as an uncharged nitroxide moiety attached to the acyl chain of a phospholipid molecule, but will not be quenched by hydrophilic quenching agents such as iodide ions (I^-) that are restricted to an aqueous solvent. We therefore used 12-doxyl-PC, a phospholipid derivative with a nitroxide positioned near the center of the bilayer, to examine the location of each NBD probe in our mutants.

We observed that only the probes exposed to a nonpolar environment (positions 401, 403, 437 and 491) were quenched by membrane-restricted nitroxide moieties (Table 1). Hence, it is clear that the loops at the tip of D4 are embedded in or exposed to the nonpolar membrane interior, and are not located at a nonpolar interface between two PFO monomers.

To estimate the depth of D4 penetration into the membrane, we compared the extents of 12-doxyl-PC quenching of D4 probes with the quenching of two residues whose location in the bilayer is fixed and known. In the TM β-barrel formed by the oligomeric complex, residue 202 is located near the membrane surface in TMH1 and residue 303 is located near the center of the membrane in TMH2 (Shatursky et al., 1999). Since the extent of quenching at positions 401, 403, 437 and 491 was similar to that at position 202 (Table 1), and since we previously showed that the Trp residues in the highly-conserved 11-residue sequence of D4 were quenched by 5-doxyl-PC, but not by 12-doxyl-PC (Heuck et al., 2000), we conclude that the membrane-exposed probes in the loops at the tip of D4 are located close to the membrane surface.

But the bulk of D4 is surrounded by water because probes with short lifetimes were strongly quenched by iodide ions (Table 2) and not by 12-doxyl-PC (Table 1). Interestingly, while two of the nitroxide-quenched probes (403 and 491) were not quenched by iodide ions, the other two (401 and 437) were weakly quenched by iodide ions (Table 2). The latter two NBD dyes are therefore most likely positioned near the interfacial region of the bilayer where they are dynamically and transiently exposed to iodide ions. Thus, both the 12-doxyl-PC and iodide ion quenching data show that the tip of D4 is located at or near the lipid-aqueous interface.

D4 orientation and contacts

If D4 were to lie along the membrane surface or were to contact adjacent PFO monomers in the oligomeric complex, a probe positioned at a protein-membrane or protein-protein interface would be completely or largely inaccessible to aqueous collisional quenchers such as iodide ions (Heuck and Johnson, 2002). We therefore examined iodide ion quenching of probes at six water-exposed positions (397, 423, 433, 442, 474 and 495) located all around the surface of the D4 β-sandwich (Figure 10) in the membrane-inserted oligomer. In each case, the NBD fluorescence was efficiently quenched (Table 2). Furthermore, since the probes on different D4 surfaces were quenched at similar rates (similar k_q), the sizeable hydrated iodide ions (9 Å diameter)

Table 1. NBD exposure to the membrane interior

Probe position	F / F_0
491	0.74 ± 0.07
403	0.73 ± 0.05
401	0.77 ± 0.02
437	0.78 ± 0.03
495	1.00 ± 0.01
433	1.05 ± 0.02
455	1.00 ± 0.01
397	1.08 ± 0.04
202 (near surface)	0.74 ± 0.06
303 (near center)	0.12 ± 0.02

Quenching of NBD fluorescence by 12-doxyl-PC was measured and calculated as described under Experimental Procedures. The F/F_0 values reported are an average of 4-8 independent experiments with the standard deviation indicated. F_0 is the emission intensity of PFO inserted into a membrane lacking 12-doxyl-PC and F is the emission intensity of an equivalent amount of PFO inserted into a membrane containing 12-doxyl-PC. To correlate the observed extents of D4 probe quenching with the depth of the probe in the bilayer under our experimental conditions, the quenching by 12-doxyl-PC of NBD probes located near the membrane surface (position 202 in TMH1) and the bilayer center (position 303 in TMH2) in the inserted PFO β-barrel are shown for comparison.

Table 2. NBD exposure to the aqueous milieu

Probe position	k_q (M^{-1} ns^{-1})	
	Water-soluble monomer	Membrane-inserted oligomer
397	7.1 ± 0.2	4.4 ± 0.1
423	3.2 ± 0.6	5.3 ± 0.1
433	6.7 ± 0.7	3.0 ± 0.1
442	12.0 ± 0.3	2.7 ± 0.2
474	7.0 ± 0.6	3.3 ± 0.1
495	5.3 ± 0.5	4.1 ± 0.1
491	9.8 ± 0.5	0
403	5.8 ± 0.2	0
401	9.5 ± 1.0	0.4 ± 0.1
437	12.3 ± 0.8	0.3 ± 0.1

Collisional quenching of NBD fluorescence by iodide ions was measured as described under Experimental Procedures. The data were analyzed according to the Stern-Volmer equation: $F_0/F = 1 + k_q\tau_0 [Q]$, where F_0 is the emission intensity of water-soluble or membrane-inserted PFO in the absence of quencher and F is the emission intensity in the presence of iodide ions at concentration [Q]. k_q is the bimolecular quenching constant and τ_0 is the primary fluorescence lifetime in the absence of quencher. k_q was determined by a linear least-squares analysis of $[(F_0/F)-1]/\tau_0$ at five different $[I^-]$ from at least three independent experiments as described under Experimental Procedures.

had similar access to all sides of D4. These data rule out the possibility that D4 lies at a small angle along the surface of the membrane in the oligomeric complex because iodide ions would not be able to move between a closely-juxtaposed D4 surface and the membrane to collide with dyes positioned at this interface. Instead, D4 must project out of the membrane surface.

The iodide ion quenching data also show that D4 does not make extensive contact with adjacent monomers in the membrane-inserted oligomer because no probe is covered up and inaccessible to iodide ions. Since we have not placed probes over the entire surface of D4, and since each dye can be displaced slightly because of its short flexible tether, some small areas of contact between D4 and adjacent monomers may exist. However, the probe distribution in our experiments is sufficient to rule out major protein-protein interfaces involving D4.

Each D4 probe is accessible to iodide ions in the water-soluble monomer, and the probes exposed to water in the membrane-inserted oligomer are also quenched by iodide ions as expected (Table 2). However, not surprisingly, the extents of NBD accessibility to iodide ions vary for the different probe locations. The reduction in quenching observed for all but one of the probes upon membrane insertion is expected because the presence of the membrane eliminates up to 50% of the routes by which iodide ions can approach and collide with each probe. But the monomeric k_q values are differentially altered when PFO inserts into the membrane. These differences indicate that the conformation of D4 changes during pore formation.

D4 topography in the membrane-inserted oligomer

The spectroscopic data reported here show directly and unambiguously that D4 is not embedded in and does not span the membrane in the fully-assembled and membrane-inserted oligomer. Instead, only the hydrophobic loops at the tip of the D4 are exposed to the nonpolar interior of the bilayer (Figure 12). This includes the conserved undecapeptide loop at the tip of D4 that cannot be labeled with an extrinsic probe, but contains intrinsic Trp fluorophores. Three of the six D4 tryptophans are located in this loop, and we have previously shown that the Trps exposed to the membrane core are located near the surface (Heuck et al., 2000). Since the other three Trps are located near the middle of D4 and cannot reach the membrane surface, only the Trps in the undecapeptide loop are exposed to the membrane interior in the oligomeric complex. Furthermore, since all sides of the D4 surface are exposed both to water and to iodide ions, D4 projects out of the membrane surface and does not appear to be involved in extensive monomer-monomer interactions. These unexpected discoveries not only establish important aspects of D4 structure in the membrane-inserted oligomer, they also provide important insights into the mechanisms of membrane recognition and pore formation by PFO.

Discussion

Role of D4 in pore formation

Since D4 is the first portion of the molecule observed to contact the membrane during pore formation (Heuck et al., 2000), and since CDCs do not function on membranes that lack cholesterol, D4 plays a critical role in PFO recognition of, and

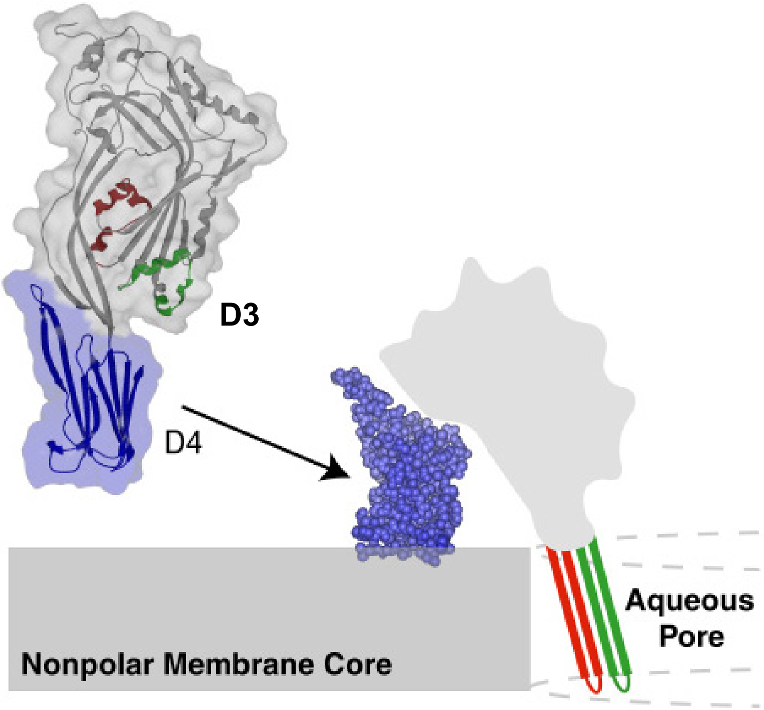

Figure 12. D4 topography in the membrane-inserted oligomer. The combined fluorescence data position D4 on the bilayer surface as shown. Only the hydrophobic loops at the tip of D4 are exposed to the nonpolar membrane interior, while the bulk of D4 is exposed to the aqueous solvent and projects from the membrane surface. In this figure, only one monomer of the membrane-inserted oligomer is shown. As indicated in the figure, PFO undergoes a major conformational rearrangement during pore formation. However, the specifics of these conformational changes have yet to be determined, and hence much of PFO is shown here as an undefined gray cartoon.

targeting to, a cholesterol-containing membrane, presumably by mediating the cholesterol interaction required for toxin activity. The high proportion of solvent-exposed hydrophobic residues in the loops at the tip of D4 in the water-soluble PFO monomer is consistent with such a role (Rossjohn et al., 1997), and our results strongly indicate that D4 interactions with the membrane are limited to those loops. Although cholesterol has been proposed to bind to sites on the D4 surface (Rossjohn et al., 1997), the nature of the putative interaction between PFO and cholesterol has yet to be defined experimentally. But our experimental data suggest that only a few residues of PFO are responsible for cholesterol, and hence membrane, recognition. Moreover, since the loops at the tip of D4 (Figure 10) represent some of the most conserved regions of CDC polypeptides, it seems likely that other CDCs recognize cholesterol in the same way.

After binding to the membrane surface, PFO oligomerizes to form a pre-pore complex (Heuck et al., 2000; Shepard et al., 2000; Hotze et al., 2001). Previous studies have suggested that D4 is a key participant in the oligomerization of different CDC molecules on the membrane surface (Iwamoto et al., 1990; Tweten et al., 1991; Gilbert et al., 1998; Weis and Palmer, 2001). If this were the case, then one would expect D4 to contact the surface(s) of adjacent CDC molecules and thereby create monomer-monomer interfaces that are inaccessible to solvent. Yet our data show that all sides of D4 except its tip are exposed to solvent and iodide ions in the membrane-inserted PFO oligomer (Table 2). Furthermore, the presence of a probe at these sites on the surface of D4 did not inhibit either oligomerization or pore formation by the toxin. The functional data therefore also indicate that monomer-monomer interactions do not include extensive coverage of D4 surfaces. Although the data presented here do not rule out a transient contact of D4 with adjacent PFO monomers during oligomer assembly, it appears that D4 does not participate directly in the interactions that stabilize the toxin complex. Instead, D4 of PFO is conformationally coupled to D3 during membrane recognition and pore formation (Heuck et al., 2000). Thus, the interaction of D4 with the membrane initiates a cascade of conformational changes within PFO that ultimately leads to pore formation.

It is clear from Figure 12 that each PFO molecule undergoes major structural rearrangements during pore formation because D3 in the middle of the elongated monomeric protein must rotate its core β-sheet relative to D4 and then move to the membrane surface to insert both TMHs. Since D3 is linked to the top of D4 via domains 1 and 2, and since the top of D4 is positioned above the membrane surface (Figure 12), a substantial amount of rotational and translational movement is required to bring the TMHs of D3 to the membrane surface. It therefore appears that D4 plays an additional role during pore formation by acting as a fulcrum or fixed axis of rotation around which the rest of the molecule can rotate and undergo the major conformational changes that are required during pore formation. Furthermore, the hydrophobic interactions between D4 and the nonpolar core of the membrane must provide sufficient stability to serve as a fixed foundation that can support the mechanical forces necessary for such structural changes, as well as facilitate the cooperative monomer-monomer interactions that enable the TMHs to penetrate the bilayer in a concerted fashion (Hotze et al., 2002).

D4 therefore performs multiple key functions during PFO pore formation, including its regulatory role in initiating the conversion of PFO from a water-soluble monomer to a membrane-inserted oligomer. All of these functions are accomplished with a minimal exposure of D4 to the membrane. Many other bacterial toxins generate pores of different types (β-sheets or α-helices) and sizes in membranes, but each faces the same mechanical problem: the regulated insertion of polypeptide into the bilayer. The data reported here therefore suggest a potential common principle for the mechanism of cytolytic action: only limited protein-membrane surface interactions are required to provide a base for the conformational changes required for pore formation.

CHAPTER IV

MECHANISM OF PFO OLIGOMERIZATION AND INTERSUBUNIT β-SHEET ALIGNMENT*

Introduction

To date, PFO from *C. perfringens* is the only member of the CDC family to have its water-soluble structure solved at atomic resolution (Rossjohn et al., 1997), and no crystal structure of a membrane-inserted CDC oligomer has yet been determined. However, by covalently attaching a fluorescent probe to monitor the environment of various sites in the molecule and by using multiple independent fluorescence techniques to examine PFO structure, we have been able to identify several unique features of the CDC during its transition from a water-soluble monomer to a membrane-inserted oligomer (Heuck et al., 2001; Heuck and Johnson, 2002). Most notably, each monomer contributes two TMHs to the β-barrel formed by the oligomer (Shepard et al., 1998; Shatursky et al., 1999). In the monomer, these TMH sequences are each folded into three short α-helices, presumably to minimize premature entanglement of the two amphipathic sequences. Furthermore, the domain located at one end of the elongated PFO monomer, D4 (Figure 12), is responsible for the initial membrane recognition and binding, but only the tip of this domain is exposed to the nonpolar interior of the bilayer in the membrane-inserted oligomer (Chapter III). Since D4 extends out of the membrane surface instead of being embedded in the bilayer, it is clear that major conformational changes are

---

*Reprinted with permission from Ramachandran, R., Tweten, R.K., and Johnson, A.E. (2004). Membrane-dependent conformational changes initiate cholesterol-dependent cytolysin oligomerization and intersubunit β-strand alignment. Nat. Struct. Mol. Biol. *11*, 697-705.

required to bring the TMHs in D3 of PFO to the membrane surface and then insert them into the membrane.

We have recently shown that oligomerization precedes pore formation, and that the formation of an oligomeric prepore complex on the membrane surface is an obligatory precursor to the concerted insertion of the D3 TMHs into the membrane (Shepard et al., 2000; Hotze et al., 2001; Hotze et al., 2002; Heuck et al., 2003). The major structural transitions in PFO that accomplish pore formation are therefore regulated by oligomerization. What then controls oligomerization? Since PFO does not associate into multimeric aggregates even at high concentrations (10 mg ml^{-1}) in aqueous solution, it would appear that whatever blocks PFO association disappears upon its stable binding to the target membrane. Furthermore, since no other proteins are involved in the spontaneous oligomerization and insertion of PFO into cholesterol-containing membranes, the regulation of oligomerization is an intrinsic property of the PFO molecule itself. In addition, oligomerization must involve a mechanism for orienting adjacent monomers and ensuring that their TMHs are correctly aligned and in proper register with those of their neighbors to effect pore formation.

To examine these control mechanisms, we have focused on four questions: What features in the three-dimensional structure of the monomer prevent its premature oligomerization in aqueous solution? How does membrane binding expose intermolecular interaction surfaces? What regions of the PFO molecule form the monomer-monomer interface in the oligomeric complex? How are the hydrogen-bonding partners between neighboring monomers aligned to generate the oligomeric

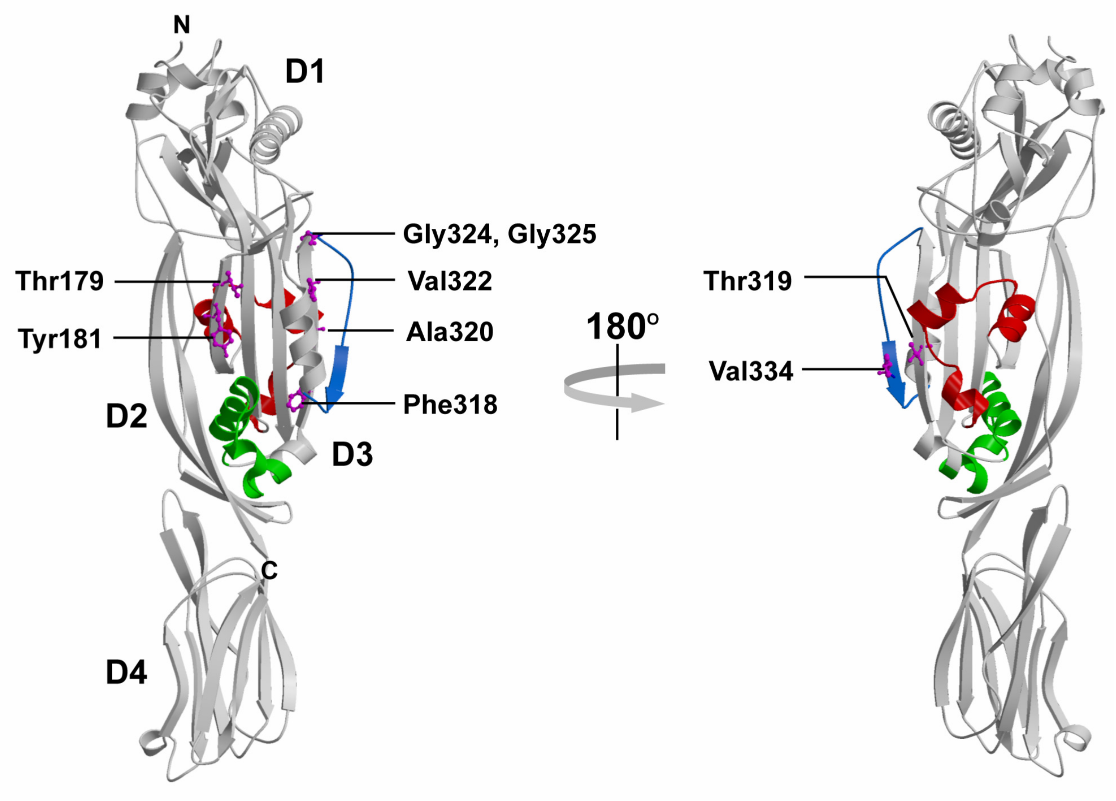
N
D1
Gly324, Gly325
Thr179
Val322
Ala320
Tyr181
Phe318
D2
D3
C
D4
180°
Thr319
Val334

Figure 13. PFO structural elements and mutations. Ribbon representation of the crystal structure of the water-soluble PFO monomer is shown in two orientations rotated 180^{o} relative to each other. Polypeptide segments in D3 comprising the six short helices that unfold to form the two TM β-hairpins are labeled TMH1 (red) and TMH2 (green). The D3 segment comprising the loop and β5 (residues 325-337) that covers the edge of β4 in the monomer is shown in blue. Residues that were mutated in this study are shown in ball-and-stick representation and labeled accordingly. Tyr 181 mutants were characterized in a previous study (Hotze et al., 2002).

TM β-barrel? By using a combination of experimental approaches, we have identified the molecular changes in PFO conformation that occur upon membrane binding and show that these changes expose an otherwise-hidden interface required for monomer-monomer interactions. These studies also suggest the mechanism by which β-strands in adjacent subunits are positioned correctly relative to each other during oligomerization.

Results

Experimental rationale

As noted above, the polypeptide sequences destined to form the TMHs are each folded into three short α-helices (Figure 13). But equally intriguing, the TMH sequences that ultimately contribute four β-strands to the β-barrel constitute extensions of an antiparallel β-sheet that forms the core of the folded protein (Shepard et al., 1998; Shatursky et al., 1999) (Figure 14). This observation led us to suggest that monomer-monomer interactions in the oligomer may involve a backbone hydrogen bonding interaction between β-strands that extends from the TMHs into the core β-sheets of PFO (Shatursky et al., 1999). It would then be reasonable to assume that oligomerization could be prevented by blocking access of one edge of the core β-sheet in a monomer (these β-strands are designated β1, β2, β3, and β4 to differentiate the core sequences from the TMH sequences that form the ends of these β-hairpins in the inserted oligomer; Figure 14) to the opposite edge of the core β-sheet in the neighboring monomer.

An examination of the crystal structure of the PFO monomer revealed that β1 in D3 is exposed to solvent and accessible for protein-protein interactions. However, β4 is

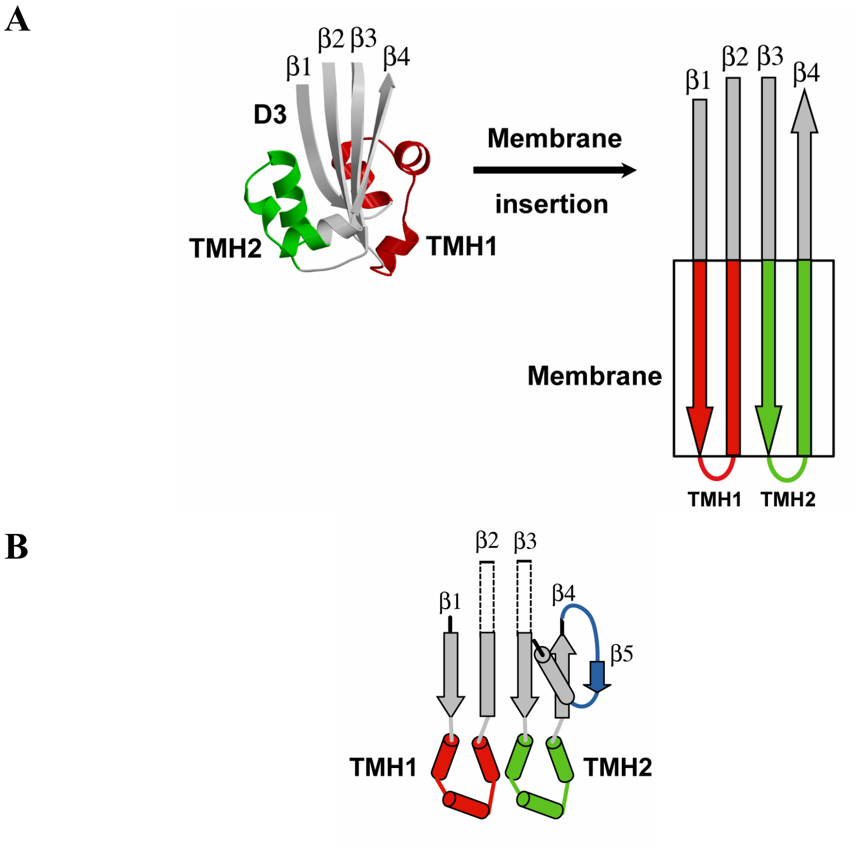
A
β1
β2
β3
β4
D3
TMH2
TMH1
Membrane
insertion
β1
β2
β3
β4
Membrane
TMH1
TMH2
B
β2
β3
β1
β4
β5
TMH1
TMH2

Figure 14. Conformational changes in D3. (A) Structure of the monomeric D3 core β-sheet is shown on the left and a cartoon representation of its extension to form the aqueous-lipid interface in the oligomeric pore is depicted on the right (view from the pore center). The segment comprising the loop, β5 and the helix (residues 325-347) that covers β4 in the monomer has been deleted to allow visualization. All ribbon representations of the crystal structure were generated using MOLSCRIPT (Kraulis, 1991) and rendered with Raster3D (Merritt and Bacon, 1997). (B) A schematic diagram of the arrangement of β-strands and α-helices in monomeric D3 with β-strands labeled β1-5 and segments color coded as above.

almost completely shielded from solvent by a stretch of polypeptide (residues 325–347) that is comprised of a loop, a short β-strand (termed β5) that hydrogen bonds to β4, and an amphipathic helix that packs across β4's hydrophobic face (Figures 13, 14). This arrangement suggested that these structural elements evolved to cover β4 and thereby prevent its premature interaction with other PFO monomers in solution. We therefore initially focused our attention on these segments to ascertain whether they indeed played a role in controlling β4 exposure.

β4 to β5 crosslinking inhibits oligomerization

To determine whether a conformational rearrangement involving β5 is required for oligomerization and/or TM β-barrel insertion, we engineered a reversible disulfide bridge between β4 and β5. In earlier studies, we successfully employed this strategy to arrest PFO in the prepore complex by disulfide crosslinking TMH1 to D2 (Heuck et al., 2000; Hotze et al., 2001). Thr319 in β4 and Val334 in β5 were replaced with cysteines based on the close proximity of their Cα atoms (Cα-Cα distance 4.5 Å) and their relatively high solvent accessibility. The double cysteine-substituted mutant was purified in the absence of reducing agent and tested for its ability to form pores in cholesterol-containing membranes. In the absence of reducing agent, the toxin was unable to form pores in cholesterol-containing membranes. However, upon reduction of the disulfide bond with DTT, pore formation ensued, thereby indicating that β5 must move relative to β4 to achieve β-barrel insertion (Figure 15).

To determine what stage of pore formation was blocked by the β4-β5 disulfide

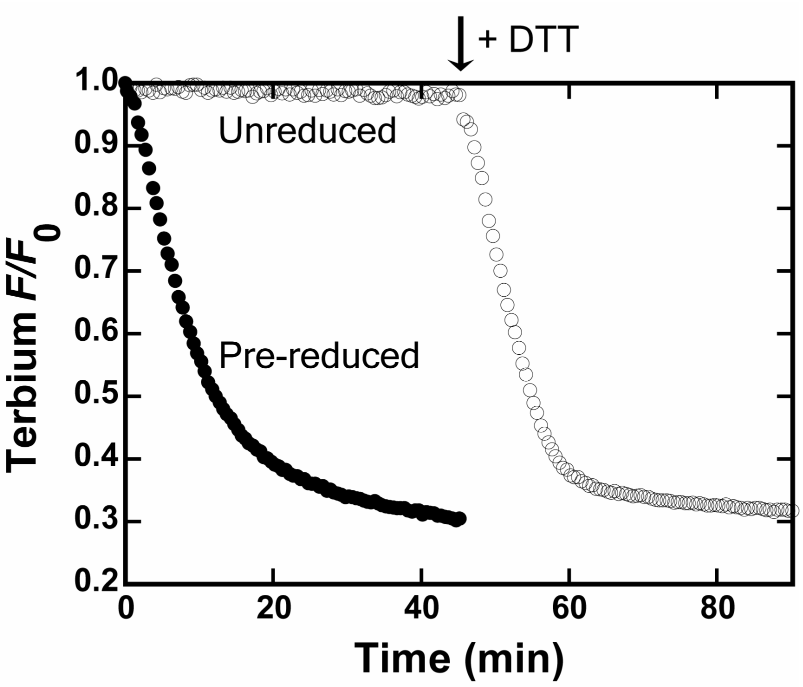

Figure 15. Effect of β4-β5 disulfide-locking on pore formation. Time-dependent emission intensity profiles for liposome-encapsulated $[Tb(DPA)_3]^{3-}$ (50 μM total lipid) when incubated with 50 nM of either pre-reduced (●) or unreduced (○) rPFO(T319C V334C) at 25°C in buffer D containing 5 mM EDTA. The release of liposome-encapsulated $[Tb(DPA)_3]^{3-}$ was monitored as described in Experimental Procedures. In the sample containing unreduced rPFO(T319C V334C), DTT was added to a final concentration of 3 mM 45 min after liposome addition (arrow). F_0 is the initial intensity prior to toxin addition and F the intensity at time 't'.

bond, we systematically tested the ability of this disulfide-trapped PFO to bind, oligomerize and insert its TM β-sheet into the target membrane. As before (Heuck et al., 2000), we monitored binding of the toxin molecule to the membrane surface by an increase in intrinsic D4 Trp fluorescence (Figure 16A) and D3 TMH insertion by the increase in emission intensity that accompanies the exposure of NBD, covalently attached to a single Cys substituted for Ala 215 in TMH1, to the hydrophobic interior of the membrane (Shepard et al., 1998) (Figure 16B). Quite remarkably, the β4-β5 disulfide-locked PFO molecule retained its ability to bind to cholesterol-containing membranes at a rate nearly identical to that of the pre-reduced toxin (Figure 16A), thereby showing that the introduction of the disulfide bond in D3 did not detectably affect either the structure or the function of D4. However, the disulfide-locked mutant lacked the ability to insert into the membrane in the absence of reducing agent because no TMH1 insertion occurred under oxidizing conditions (Figure 16B).

The ability of the disulfide-locked β4-β5 toxin to oligomerize in the absence of reducing agent was examined using agarose gel electrophoresis in the presence of SDS (SDS-AGE). We have previously demonstrated that both the prepore and the pore complexes of PFO are stable to SDS exposure, though the prepore complex is slightly more susceptible to subunit dissociation than is the fully-inserted oligomer (Shepard et al., 2000). However, the prepore complex can be stabilized by the addition of glutaraldehyde, an amine-to-amine crosslinking reagent, prior to SDS addition. The crosslinked prepore species exhibits mobility in SDS-AGE similar to that of the SDS-resistant and fully-inserted pore complex.

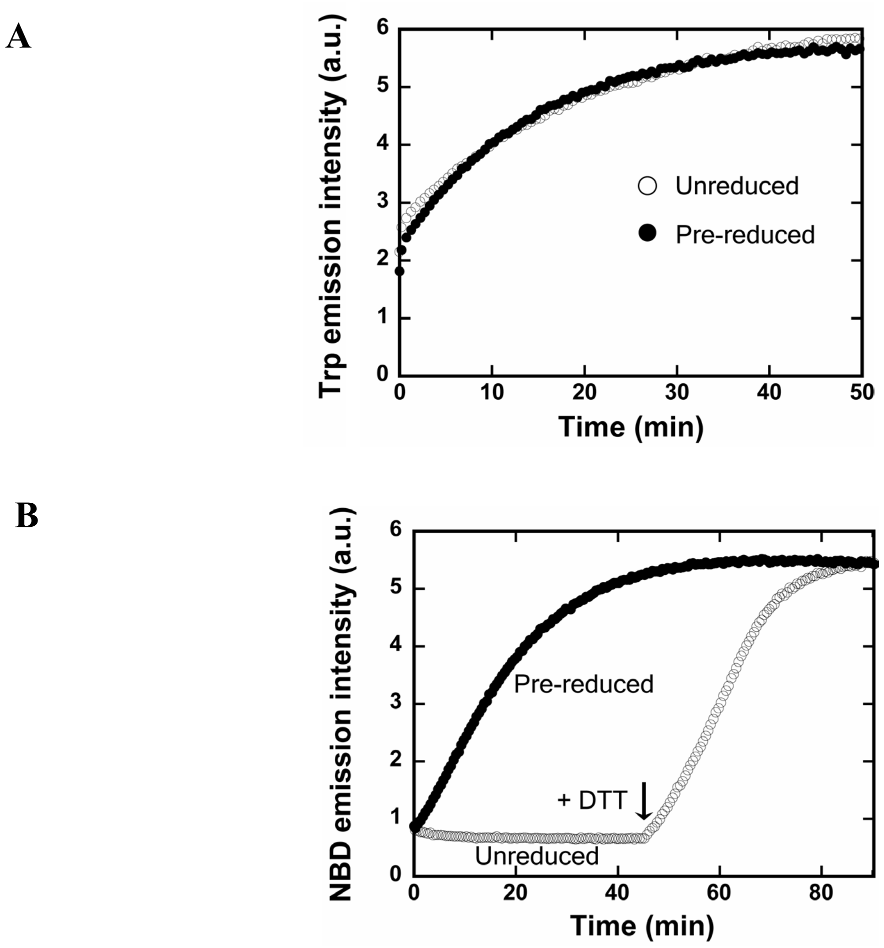

Figure 16. Effect of β4-β5 disulfide-locking on membrane binding and TMH insertion. (A) Time-dependent Trp emission intensity for either pre-reduced (●) or unreduced (○) rPFO(T319C V334C) after addition of cholesterol-containing liposomes as described in Experimental Procedures. No DTT was added during the course of the experiment. (B) Time-dependent emission intensity for NBD attached to a membrane-facing cysteine residue at position 215 (A215C) in TMH1 was measured for either pre-reduced (●) or unreduced (○) rPFO(T319C V334C A215C-NBD) after addition of cholesterol-containing liposomes as described in Methods. In the sample containing oxidized rPFO(T319C V334C A215C-NBD), DTT was added to a final concentration of 3 mM 45 min after liposome addition (arrow).

The disulfide-locked β4-β5 PFO derivative was therefore examined to determine whether it formed a prepore complex under oxidizing conditions. In the absence of the crosslinker, no band other than the monomer band was detected, even after incubating the toxin with cholesterol-containing membranes at 37°C for 30 min or more (Figure 17, lane 3). When 5 mM glutaraldehyde was added 2 min prior to the addition of SDS, small higher-molecular-mass species, presumably dimers and trimers, were observed in the gel (Figure 17, lane 4). However, none of these species corresponded to the much larger size of the prepore complex, thereby indicating that the disulfide-trapped β4-β5 mutant is unable to form a prepore complex. As expected, pre-reduction of the disulfide bond before addition of target membranes resulted in the mutant behaving very similarly to functional PFO by forming a large, SDS-resistant oligomer (Figure 17, lane 7). Thus, the presence of a disulfide-bond between β4 and β5 apparently prevents the structural rearrangement that exposes β4 for intermolecular interactions. Hence, we conclude that the disulfide-locked β4-β5 PFO derivative is trapped at the membrane-bound monomer stage of pore formation.

Membrane binding alters PFO conformation near β4

We previously showed the existence of a highly-coordinated interdomain communication network between D3 and D4 in PFO in which mutations in D3 dramatically altered the kinetics of D4 binding to the membrane, even though D4 binds first to the membrane and the D3 mutation sites were spatially distant from D4 (Heuck et al., 2000). However, the extent and location of the conformational changes that occur upon D4 binding to the membrane were unknown. We therefore explored the possibility

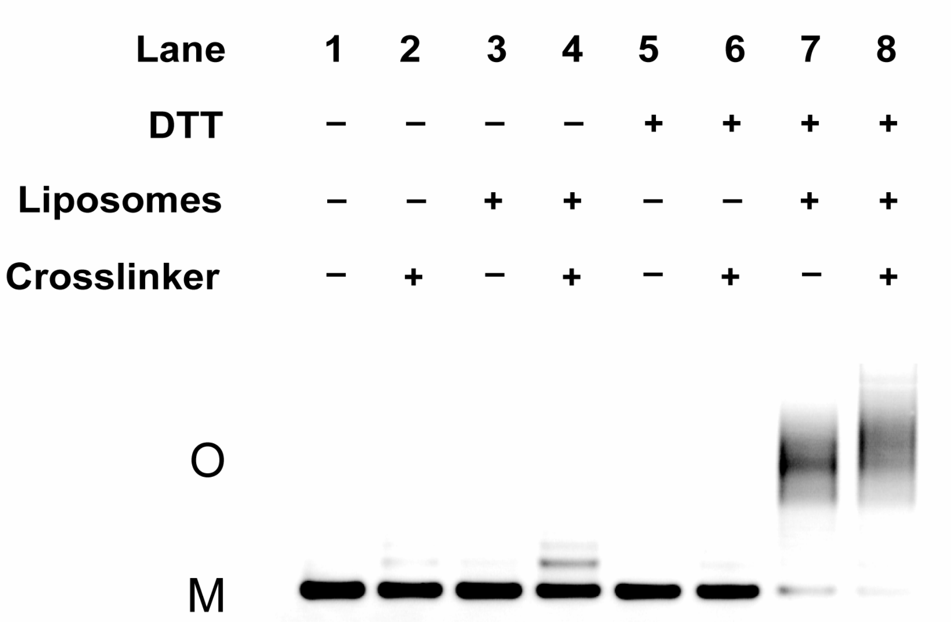

Figure 17. Effect of β4-β5 disulfide-locking on oligomerization. Samples containing either unreduced (- DTT) or pre-reduced (+ DTT) rPFO(T319C V334C A215C-NBD) (1 μM final) were incubated in the absence or presence of cholesterol-containing liposomes (1 mM total lipid) in buffer D for 30 min at 37°C as indicated. After the incubation, each sample was divided into two equal aliquots. One aliquot received 5 mM glutaraldehyde for 2 min at room temperature before the addition of urea (1 M final), while the other aliquot received buffer D instead of the crosslinker prior to urea addition. All samples were then dissolved in SDS sample buffer and electrophoresed as described in Experimental Procedures before visualization by NBD emission. M represents the monomer and O the oligomer.

that the membrane-dependent conformational changes in D3 involved β4.

In the PFO monomer structure, residues 325–347 comprise the loop, β5 and the helix that form the ridges of a highly hydrophobic groove whose base consists primarily of residues from β4 (Figure 13). A conformational rearrangement to expose β4 would presumably also expose this base to solvent. Thus, to ascertain whether this putative rearrangement occurs, a fluorescent NBD probe was covalently attached to a single Cys substituted at position 322 in β4. This NBD-labeled PFO derivative exhibited pore-forming activity comparable to the wild-type toxin (Appendix, Figure 33).

NBD is an environmentally-sensitive fluorophore whose emission lifetime and intensity are highly sensitive to the presence of water (Crowley et al., 1993; Shepard et al., 1998; Heuck and Johnson, 2002). In a non-aqueous milieu, NBD has a fluorescence lifetime $\tau > 7$ ns, while its lifetime in an aqueous environment is ~ 1 ns. As expected, the NBD dye at position 322 exhibited a high fluorescence lifetime (> 9 ns) in the monomeric form of the toxin, thereby demonstrating the dye's burial in a hydrophobic environment. However, in the membrane-inserted form of the toxin, the NBD at position 322 was in an aqueous environment ($\tau \sim 1$ ns) (Table 3). These data clearly show that a major change in conformation occurs near β4 during pore formation.

To gain temporal insight into this change in protein conformation, the rate of PFO binding to membranes was monitored by the increase in intrinsic D4 Trp emission intensity upon liposome addition and then compared to the rate of NBD emission intensity decrease when liposomes were added to rPFO(V322C-NBD). We have previously used similar kinetic measurements to demonstrate that the binding of D4 to

Table 3. Fluorescence lifetimes of rPFO(V322C-NBD)

Species	τ_1 (ns)	width (ns)	mol%	τ_2 (ns)	mol%
monomer	9.1	1.4	80	0.9	20
oligomer	0.6		93	5.7	7

The phase and modulation data were collected as described in Experimental Procedures and analyzed using GLOBALS UNLIMITED (University of Illinois) to compute the mole fraction of dyes in each environment. For the water-soluble monomer, the data were best fit (had the lowest χ^2) to a Lorentzian distribution of long lifetimes and a discrete short lifetime, while the membrane-inserted oligomer data were best fit to two discrete lifetimes. In both cases, the major lifetime component (mole fraction > 80%) indicated that the probes were predominantly in either a hydrophobic (lifetime > 7 ns) or an aqueous environment (lifetime ~ 1 ns). The minor lifetime component presumably represents probes that are dynamically exposed to different environments.

the membrane surface precedes the insertion of NBD-labeled D3 TMHs into the bilayer (Heuck et al., 2000). But in this case, the rates of Trp and NBD intensity changes were nearly superimposable for rPFO(V322C-NBD) (Figure 18). This result demonstrates that the NBD-detected conformational rearrangement around β4 essentially coincides with PFO binding to the membrane surface and precedes TMH insertion into the bilayer.

To determine directly whether the conformational change detected by the NBD probe in β4 is coupled to the movement of β5 relative to β4, a V322C mutation was introduced into the derivative that forms the β4-β5 disulfide bond, rPFO(T319C V334C), to yield rPFO(T319C V334C V322C). This protein was purified under non-reducing conditions and then labeled with NBD to form rPFO(T319C V334C V322C-NBD). When liposomes were added to a sample of this protein, the NBD emission intensity decreased by about 20% (Figure 19), much less than the 95% decrease observed with rPFO(V322C-NBD) (Figure 18). However, when DTT was then added to the disulfide-trapped sample, a dramatic decrease in NBD intensity was observed (Figure 19), similar to that seen in Figure 18. The origin of the initial 20% decrease may be due to a partial rotation of β5 relative to β4 and/or to a fraction of the rPFO(T319C V334C V322C-NBD) proteins that lacked disulfide bonds. Most important, the large fluorescence change observed upon addition of DTT demonstrates that the conformational change that exposes β4 requires β5 to move relative to β4, and hence that the membrane-dependent conformational change in D3 involves the rearrangement of β5 around β4.

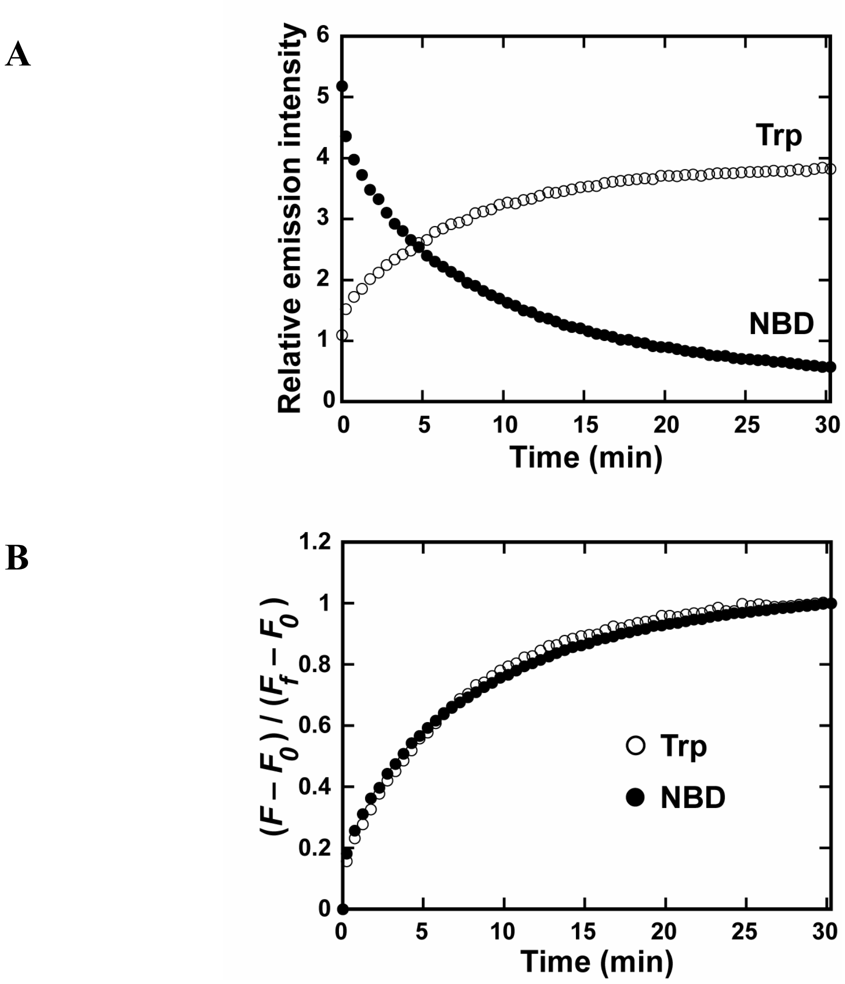

Figure 18. D4-membrane interaction triggers a conformational change around β4 in D3. (A) Time-dependent emission intensities for Trp (○) and NBD (●) in rPFO(V322C-NBD) (50 nM) were measured upon addition of 50 μM liposomes (55 mol% cholesterol, 45 mol% POPC) as described in Experimental Procedures. (B) To allow direct comparison of the rate of change in Trp (○) and NBD (●) fluorescence, each intensity profile was normalized and plotted as the total fractional intensity change as a function of time. F_0 represents the initial emission intensity before the addition of liposomes, F the intensity at time 't', and F_f the intensity when t = 30 min.

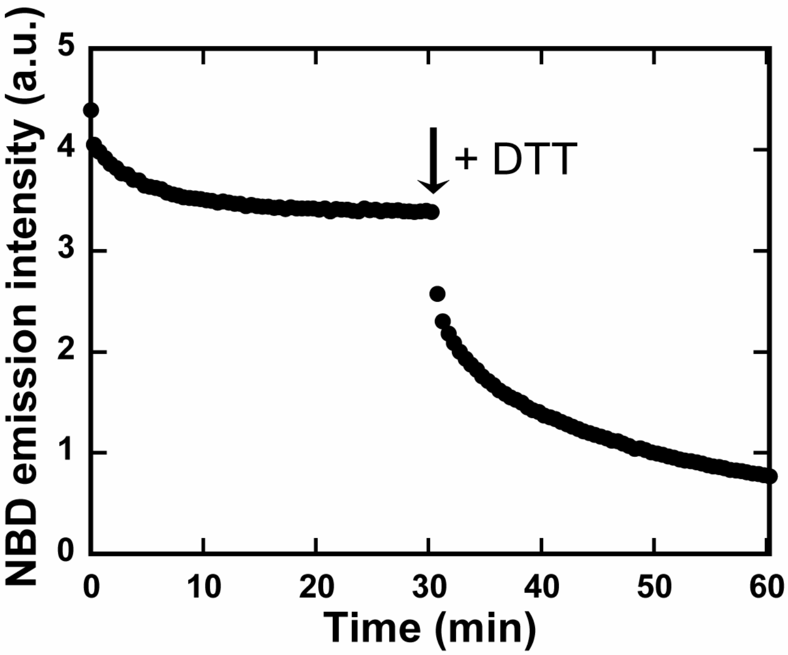

Figure 19. Effect of β4-β5 disulfide-locking on the conformational change around β4. Time-dependent emission intensity for NBD in rPFO(T319C V334C V322C-NBD) (50 nM) was measured upon addition of 50 μM liposomes as described in Experimental Procedures. DTT was added to a final concentration of 3 mM 30 min after liposome addition (arrow).

Loop flexibility is required for oligomerization

Examination of the monomeric crystal structure revealed the presence of two glycines (Gly324, Gly325) at the junction of β4 and the loop leading to β5 (Figure 13). Interestingly, these glycines are conserved throughout the CDC family. To ascertain whether these glycines play an important functional/structural role in pore formation, we mutated both of these residues to valines. Valine, a bulky β-branched residue, restricts extensive movement around its peptide bond and hence may restrict any conformational rearrangement of the loop and movement of β5. The twin glycine mutant rPFO(G324V G325V) did not exhibit any pore-forming activity (Appendix, Figure 33), though it retained the ability to bind to cholesterol-containing membranes as detected by the increase in intrinsic tryptophan emission intensity (Appendix, Figure 34A).

The absence of a prepore-sized oligomer after SDS-AGE analysis of rPFO(G324V G325V A215C-NBD) and visualization of bands by NBD fluorescence revealed that this mutant lacked the ability to form large oligomers on the membrane surface (Figure 20). Thus, valines at positions 324 and 325 apparently hinder the conformational rearrangement of the loop to β5 that is required to expose β4 for intermolecular interactions, consistent with the two glycines at the junction of β4 and the loop serving as a hinge around which to rotate the loop and β5 to expose β4.

β1 of one monomer is adjacent to β4 of its neighbor

As noted above, it was previously suggested that monomer-monomer association would involve the hydrogen-bonding of β1 from one PFO molecule to β4 of the adjacent molecule in the oligomer (Shatursky et al., 1999). However, the monomer-monomer

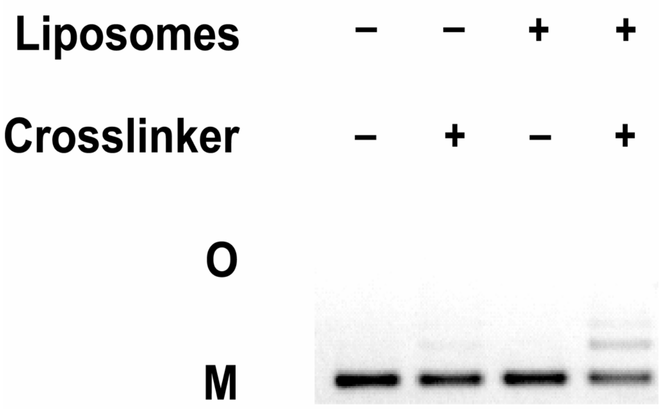

Figure 20. Mutation of glycines at the end of β4 blocks oligomerization. SDS-AGE analysis of 2 μM rPFO(G324V G325V A215C-NBD) was carried out as described in Figure 17. Cholesterol-containing liposomes were added to a final concentration of 2 mM.

interfacial surfaces have not been identified experimentally. To determine whether β1 in D3 of each monomer is in close proximity to, and therefore can interact with, β4 in D3 of the neighboring monomer to generate an extended β-sheet in the oligomer (Figure 13), we exploited the spectral properties of the fluorophore pyrene. The emission scan of monomeric pyrene reveals two peaks at 375 nm and 395 nm (λ_{ex} = 345 nm), while a broad emission peak centered near 470 nm is observed when two pyrene dyes stack to form an ‘excited-state dimer’ or ‘excimer’ (Lehrer, 1997). Pyrene excimer formation is therefore only seen when two pyrene dyes are positioned adjacent to each other and are able to stack. As a result, this experimental approach constitutes an excellent method for detecting the close proximity of two sites labeled with pyrene dyes. For example, pyrene attached to a cysteine in β1 of one molecule can stack and form an excimer with a pyrene attached to a cysteine in β4 of another molecule only if the loop and β5 in the latter are rearranged from their original positions in the water-soluble monomer and if the β1 and β4 strands of neighboring monomers move adjacent to each other during oligomer formation.

Two separate PFO derivatives were prepared by attaching a pyrene moiety to a single cysteine positioned either at residue 179 in β1 or, alternatively, residue 322 in β4 (Figure 13). Pyrene labeling at position 322 did not affect pore formation, while modification of the Cys at position 179 with any fluorophore blocked membrane insertion (Appendix, Figure 35A). Equimolar mixtures of rPFO(T179C-Pyr) and either rPFO or rPFO(V322C-Pyr) exhibited pore formation (Appendix, Figure 35A) but we could not unambiguously determine the extent of rPFO(T179C-Pyr) incorporation into the inserted oligomers. However, rPFO(T179C-Pyr) formed pyrene fluorescence-detected oligomers when mixed with an equivalent amount of rPFO, thereby demonstrating that rPFO(T179C-Pyr) was able to associate with functional PFO molecules into prepore complexes (Appendix, Figure 35B). Since rPFO(T179C-Pyr) associated with other PFO molecules to form oligomers, we were able to assess whether or not β1 and β4 were adjacent to each other in the prepore complex using excimer fluoresence.

When an equimolar mixture of rPFO(T179C-Pyr) and rPFO(V322C-Pyr) was incubated with cholesterol-containing membranes, a strong pyrene excimer band was observed, thereby showing directly the close proximity of β1 in one monomer with β4 in the neighboring monomer in the oligomer (Figure 21). No excimer formation was observed when the mixture was incubated either in the absence of membranes or in the presence of cholesterol-free membranes (Figure 21A). In control experiments, no excimer fluorescence was seen in oligomers generated with only one of the two Pyr-labeled mutants, indicating that pyrenes attached to the same position on adjacent PFO molecules are not close enough to stack (Figure 21B). Furthermore, no excimer formation was observed when rPFO(V322C-Pyr) was mixed with rPFO(Y181C-Pyr), thereby showing the expected strong dependency on the proximity of the pyrenes (Appendix, Figure 36).

To determine whether the close proximity of β1 and β4 in neighboring monomers requires the membrane-dependent rearrangement of β5, the T179C and V322C mutations were introduced into derivatives that form the β4-β5 disulfide bond

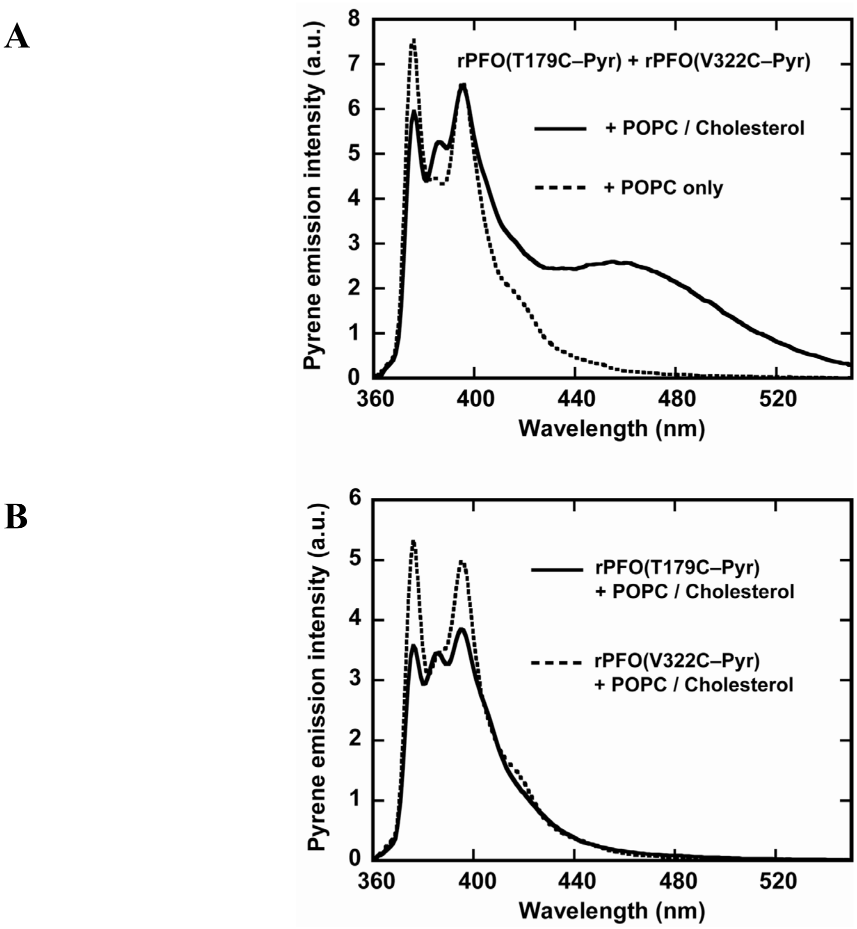

Figure 21. Pyrene excimer formation detects β1 and β4 proximity in neighboring PFO. (A) Pyrene emission spectra for an equimolar mixture of rPFO(T179C-Pyr) and rPFO(V322C-Pyr) (100 nM total) in the presence of 100 μM lipid in cholesterol-containing (solid line) or cholesterol-free POPC (dotted line) liposomes. (B) Pyrene emission spectra for rPFO(T179C-Pyr) (solid line) and rPFO(V322C-Pyr) (dotted line) (100 nM each) in the presence of cholesterol-containing liposomes (100 μM lipid).

and then the free Cys was labeled with pyrene to yield rPFO(T319C V334C T179C-Pyr) and rPFO(T319C V334C V322C-Pyr). Although the efficiency of Cys labeling at position 322 was reduced by the presence of the β4-β5 disulfide bond (see Experimental Procedures), these samples were sufficiently labeled to clearly resolve the issue. No excimer formation was observed when an equimolar mixture of rPFO(T319C V334C T179C-Pyr) and rPFO(T319C V334C V322C-Pyr) was incubated with cholesterol-containing membranes under non-reducing conditions (Figure 22). However, upon reduction of the disulfide bond, excimer formation was observed (Figure 22), which indicates that the membrane binding-dependent rearrangement of β5 exposes β4 and allows the close juxtaposition of β1 and β4 in neighboring monomers. (Less excimer formation was seen in Figure 22A than in Figure 21A because of the lower pyrene content in the disulfide-linked sample.) These data therefore show that β1 in one monomer is in close proximity to β4 in the neighboring monomer where they can participate in hydrogen-bonding interactions to generate the oligomeric β-sheet (Figures 14, 21, 22). The β1 and β4 edges of the core PFO β-sheet therefore constitute important interfacial surfaces between two monomers in the oligomeric complex.

Aromatic residues align intersubunit β-strands

A previous study showed that the mutation of Tyr181 in β1 to a residue other than Phe dramatically inhibited the pore-forming activity of the toxin by preventing the insertion of the TM β-barrel and reducing the stability of the prepore complex (Hotze et al., 2002). The strict requirement for an aromatic residue at position 181 suggests that it is involved in a π-stacking interaction with an aromatic residue of the neighboring

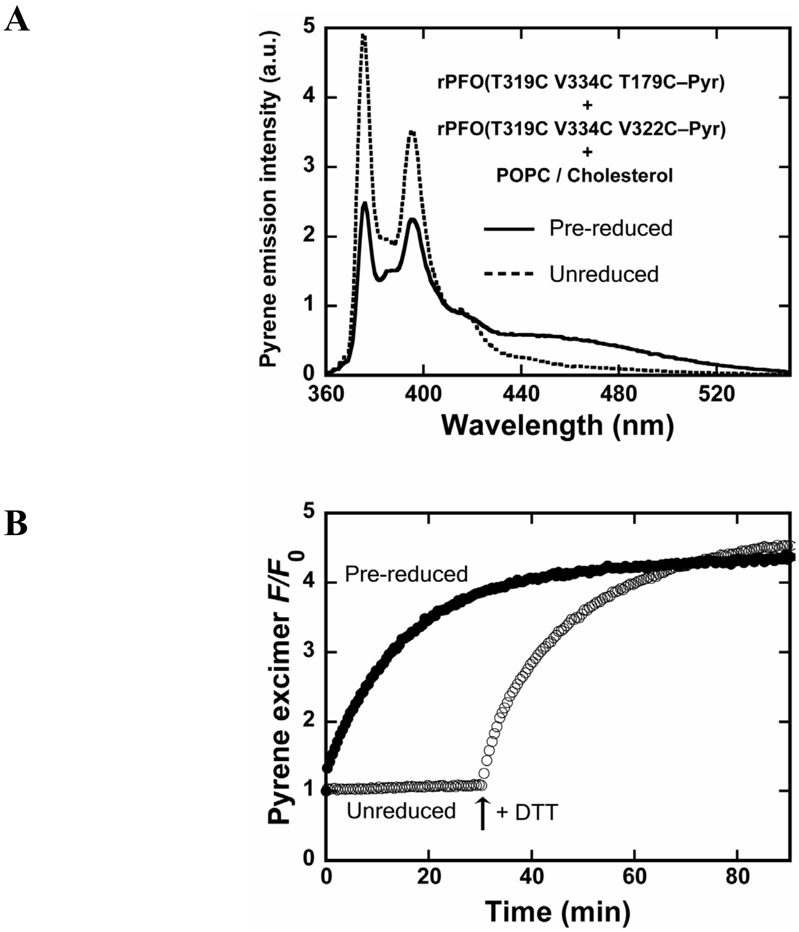

Figure 22. Excimer formation in the presence of the β4-β5 disulfide lock. (A) Pyrene emission spectra for an equimolar mixture of rPFO(T319C V334C T179C-Pyr) and rPFO(T319C V334C V322C-Pyr) (100 nM total) incubated with cholesterol-containing liposomes (100 μM lipid) in the presence (solid line) and absence (dotted line) of 3 mM DTT. (B) Time-dependent pyrene excimer emission intensity for an equimolar mixture of rPFO(T319C V334C T179C-Pyr) and rPFO(T319C V334C V322C-Pyr) was measured as described in Experimental Procedures for either a pre-reduced (●) or an unreduced (○) sample. In the sample containing the oxidized protein, DTT was added to a final concentration of 3 mM 30 min after liposome addition (arrow).

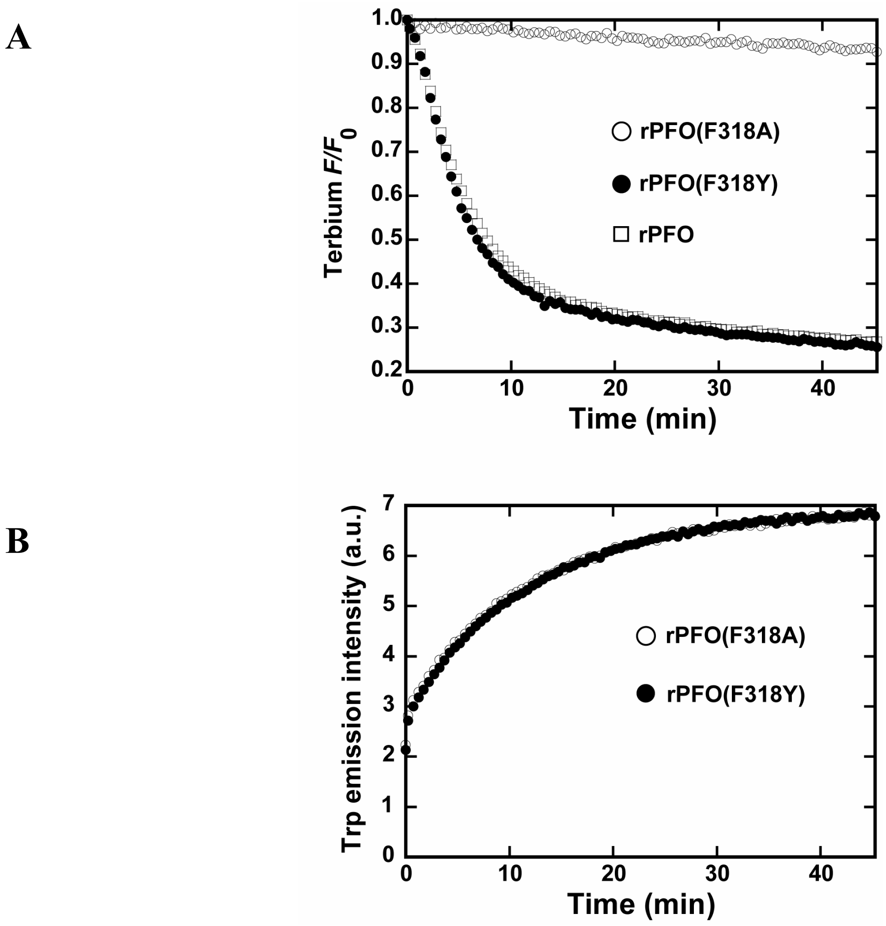

Figure 23. F318A mutation blocks pore formation but not membrane binding. (A) Time-dependent emission intensities for liposome-encapsulated $[Tb(DPA)_3]^{3-}$ (50 μM total lipid) were measured at 25°C as described in Experimental Procedures after the addition of 50 nM rPFO(F318A) (○), rPFO(F318Y) (●), or rPFO (□). (B) Time-dependent Trp emission intensity was measured after addition of cholesterol-containing liposomes (50 μM) to 50 nM rPFO(F318A) (○) and rPFO(F318Y) (●) as described in Experimental Procedures.

monomer to stabilize the intersubunit β-strand association in the prepore complex and/or promote the insertion of the β-barrel into the membrane bilayer. Examination of the PFO structure revealed that β1 and β4 each contained only a single aromatic residue: Tyr181 and Phe318, respectively (Rossjohn et al., 1997). Furthermore, each of the 11 sequenced CDCs has a Tyr at the equivalent of position 181, while 8 of the 11 have a Phe at 318.

Substitution of Phe318 with Ala, Cys or Trp prevented pore formation, while a F318Y substitution did not alter pore formation (Figure 23A; data for F318C and F318W not shown). However, the F318A mutant was able to bind cholesterol-containing membranes at a rate similar to that of the F318Y mutant, as determined by the increase in intrinsic Trp fluorescence (Figure 23B). Moreover, like the Y181A mutant (Hotze et al., 2002), the F318A mutant was able to form a prepore complex on the membrane surface (Figure 24A). But little insertion of the TM β-sheet of rPFO(F318A A215C-NBD) was observed by increases in either NBD lifetime (Table 4) or intensity (Figure 24B), as expected by the lack of pore formation. When a 4-fold excess of unmodified and functional rPFO was mixed with rPFO(F318A A215C-NBD), the mutant toxin molecules were able to insert their TMHs into the bilayer (Table 4, Figure 24B). This effect is similar to that observed earlier with the Y181A mutant (Hotze et al., 2002), where the cooperative nature of the pore formation process allows wild-type PFO molecules to overcome whatever barrier is created by the F318A mutation. Thus, the comparable mutations at Tyr181 and Phe318 were phenotypically identical in terms of disrupting late stages of PFO pore formation.

The fact that pore formation occurred only if the small aromatic side chains of

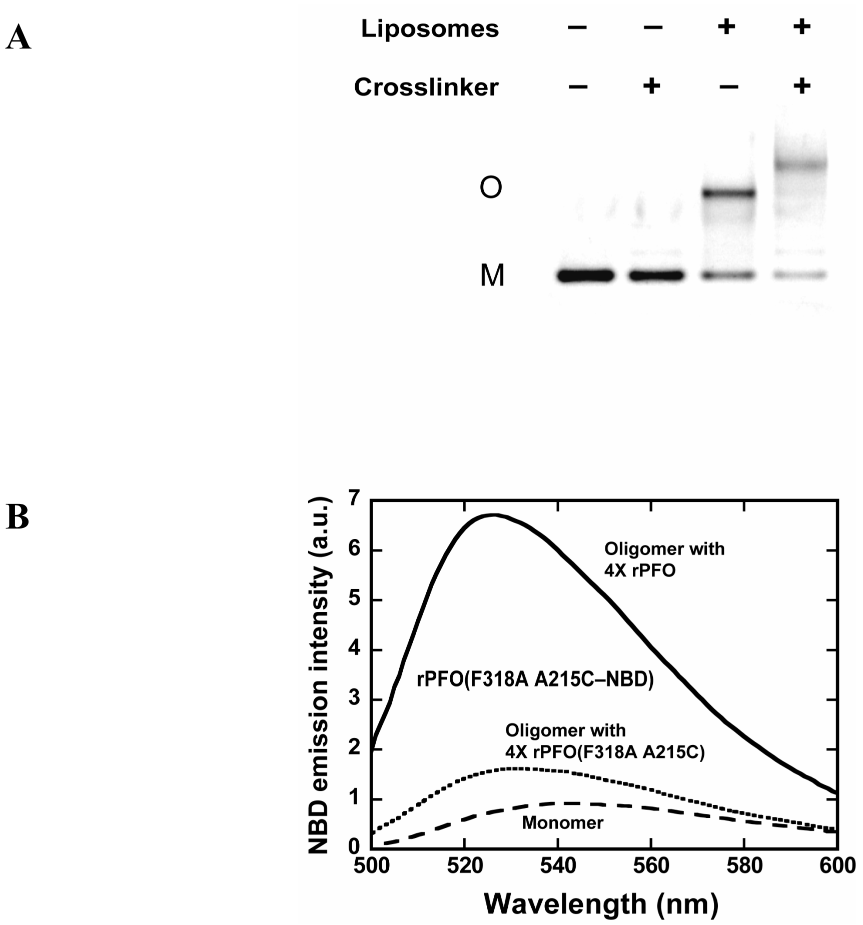

Figure 24. F318A mutation blocks TMH insertion but not prepore formation. (A) SDS-AGE analysis of rPFO(F318A, A215C-NBD) in the presence or absence of liposomes and in the presence or absence of glutaraldehyde as indicated. (B) NBD emission spectra for 20 nM rPFO(F318A, A215C-NBD) in the absence of liposomes (dashed line), in the presence of 80 nM unlabeled rPFO(F318A, A215C) and cholesterol-containing liposomes (dotted line), and in the presence of 80 nM rPFO and cholesterol-containing liposomes (solid line). The toxin was incubated with liposomes (100 μM total lipid) in buffer D at 37°C for 30 min before cooling to 25°C for spectral measurements as described in Experimental Procedures.

Table 4. Fluorescence lifetimes of rPFO(F318A A215C-NBD)

Species	τ_1 (ns)	mol%	τ_2 (ns)	mol%
monomer	1.2	87	4.2	13
oligomer	1.3	85	7.7	15
oligomer formed with 4X rPFO	8.7	69	0.9	31

Lifetimes were measured and the data analyzed as described in Table 3. In all cases, the data were best fit to two discrete lifetimes.

Tyr or Phe were located at positions 181 and 318 is consistent with the idea that a sterically-restricted π-stacking interaction between the two residues is required for PFO oligomer insertion into the bilayer. One way to address this possibility experimentally is to shift each aromatic residue two positions along its β-strand so that the side chains would be on the same side of the β-sheet as in wild-type PFO. If the stacking of the aromatic rings is important for function, then it is possible that this derivative would be active because the locations of the rings relative to each other would be unchanged.

We therefore prepared a quadruple mutant of rPFO(Y181A F318A T179Y A320F) (iv in Figure 25), as well as mutants that contained only one altered aromatic or no aromatics as controls (i, ii, and iii in Figure 25). All of these derivatives were able to form large oligomeric complexes on cholesterol-containing membranes (Figure 26A). However, only one, the quadruple mutant iv, was functionally active. While the control samples were not active or were barely active in pore formation, iv formed pores at a rate faster than that of unmodified rPFO (Figure 26B). The increased rate of pore formation by iv is explained by the fact that iv binds to membranes at a much higher rate than does its parent toxin, rPFO (Appendix, Figure 34B). This result shows that the relative positioning of the two aromatic rings in β1 and β4 is critical for PFO pore formation. Thus, it appears that the stacking of Tyr181 and Phe318 between neighboring monomers not only helps to stabilize the prepore complex, but also serves to align the adjacent β1 and β4 strands in the proper register to effect insertion of the TM β-barrel. A similar stacking phenomenon has been proposed to stabilize the assembly of β-sheet-rich amyloid fibrils containing short aromatic-containing peptides (Gazit, 2002).

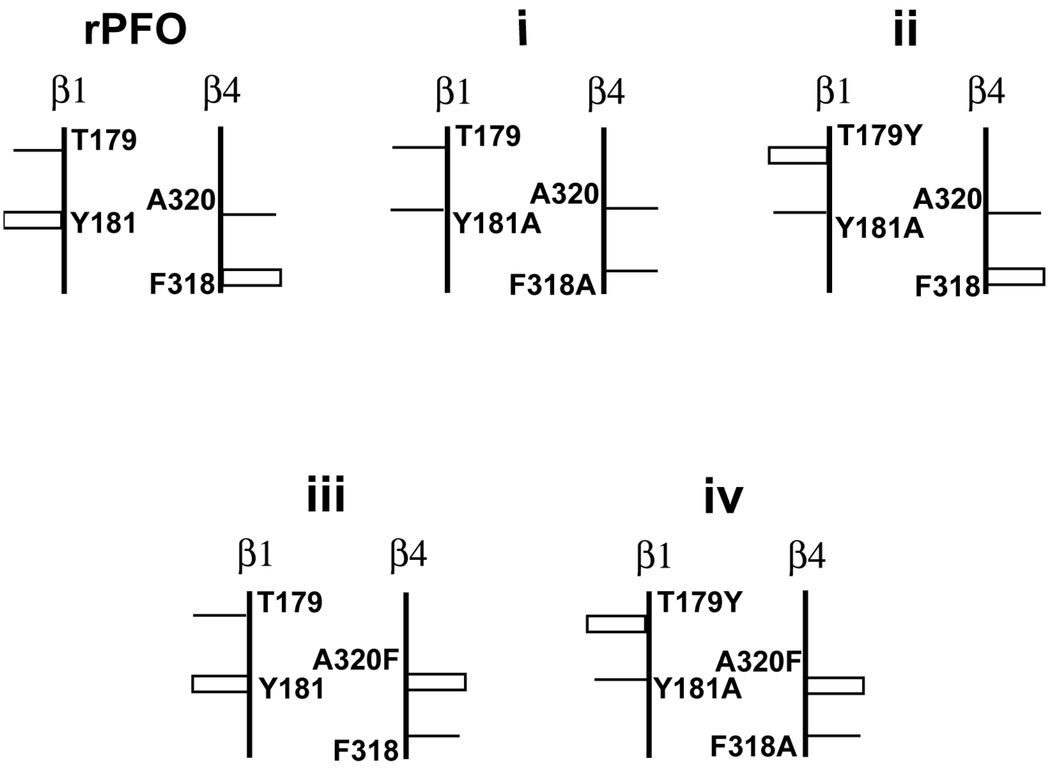
rPFO
β1
β4
T179
Y181
A320
F318
i
β1
β4
T179
Y181A
A320
F318A
ii
β1
β4
T179Y
Y181A
A320
F318
iii
β1
β4
T179
Y181
A320F
F318
iv
β1
β4
T179Y
Y181A
A320F
F318A

Figure 25. Alignment of aromatic residues in β1 and β4 is critical for pore formation. Aromatic residue positioning in β1 and β4 of rPFO and mutants labeled **i** through **iv**.

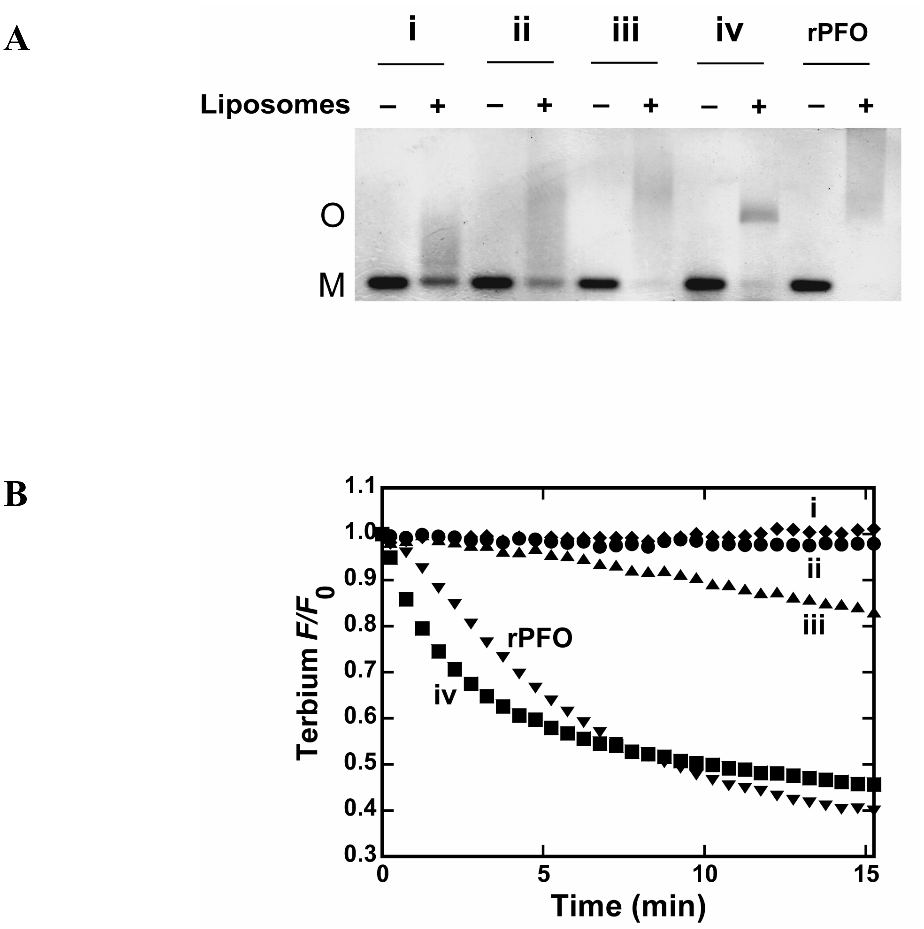

Figure 26. Analysis of mutants i through iv. (A) SDS-AGE analysis of oligomer formation by rPFO and i–iv as in Figure 25. All samples received glutaraldehyde and oligomers were detected using Coomassie Blue staining. (B) Time-dependent detection of pore formation by rPFO and i–iv as in Figure 25.

Discussion

Mechanism of PFO oligomerization and intersubunit β-sheet alignment

Four questions critical to our understanding of how PFO oligomerizes and forms pores were posed, and the answers to these questions have here been determined experimentally using a wide variety of approaches and techniques. The monomer-monomer interface in the PFO oligomer is formed when the β1 strand in one subunit associates, presumably via hydrogen bonding, with the β4 strand in a second subunit (Figures 21, 22). Premature association of PFO molecules (i.e., prior to their binding to an appropriate membrane surface) is prevented by the presence of β5, a short stretch of polypeptide that hydrogen bonds to β4 in the monomer and thereby prevents its interaction with the β1 strand of a second subunit (Figures 15-17). The binding of PFO D4 to the membrane surface elicits a conformational change in D3 that rotates β5 away from β4 and thereby exposes β4 to the aqueous medium where it can associate with the always-exposed β1 strand of another PFO molecule to initiate or promote oligomerization (Figures 18, 19). The β-strands of neighboring monomers then appear to be aligned in the proper register relative to each other by the aromatic π-electron stacking of the Tyr and Phe residues in β1 and β4. Since no pore formation is observed with mutants lacking Phe or Tyr at positions 181 and 318, this previously-unrecognized stacking interaction is an essential step in the mechanism of PFO pore formation (Figures 23-26). The data obtained here with various spectroscopic approaches have therefore provided significant insight into the molecular mechanisms that regulate the oligomerization of PFO (and probably other CDCs) and the initiation of pore formation.

When these results are combined with those of our previous studies, the sequence of events that control and/or effect the transition of PFO from one functional state to the next are, for the most part, clearly delineated. Upon secretion from *C. perfringens,* PFO folds into a stable tertiary structure that avoids or minimizes the potential entanglement of the two amphipathic TMHs prior to membrane binding by having each adopt a stable α-helical secondary structure in the monomer (Rossjohn et al., 1997; Shepard et al., 1998; Shatursky et al., 1999). The premature association of PFO monomers in solution is prevented by the hydrogen bonding of β5 to β4 that obscures the subunit-subunit interface (Figure 27A). When D4 recognizes a cholesterol-containing membrane surface (Heuck et al., 2000), only the polypeptide loops at the tip of D4 are inserted into the nonpolar core of the bilayer (Ramachandran et al., 2002) and a conformational change is triggered that extends more than 70 Å through the elongated PFO monomer to rotate the loop containing β5 around the Gly-Gly swivel at the end of β4 (Figure 20) and thereby expose the edge of β4 to the solvent (Figure 27B). Two-dimensional diffusion on the membrane surface then leads to productive collisions between PFO monomers that result in β1 in one monomer hydrogen bonding to the now-exposed β4 in a second PFO molecule (Figure 27C). Continued association of monomers with the original PFO dimer results in an oligomer (Heuck et al., 2000; Shepard et al., 2000; Hotze et al., 2001) containing up to 50 PFO molecules in a circular prepore complex (Oloffson et al., 1993; Hotze et al., 2001). Upon association, β1 and β4 in neighboring subunits move parallel to each other until Tyr181 in β1 of one subunit stacks on Phe318 of β4 in the adjacent

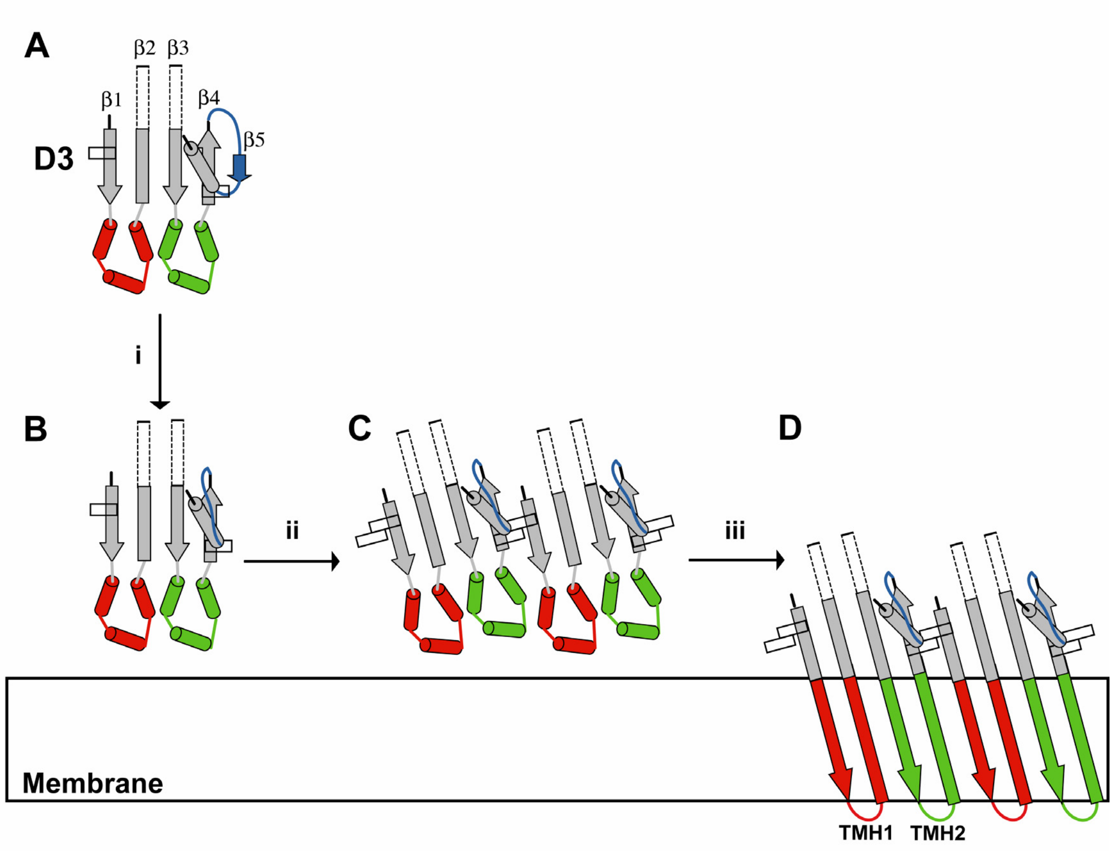

Figure 27. Mechanism of oligomerization and intermolecular β-sheet formation. (A-D) A schematic model of the conformational changes required for monomer-monomer interactions and β-barrel formation in D3 of PFO is depicted and described in the text. Stage i represents the binding of PFO to the membrane surface via D4 (not shown in the figure), stage ii the oligomerization of PFO monomers on the membrane surface, and stage iii the insertion of the oligomer TMHs into the membrane. Aromatic residues in β1 and β4 of neighboring monomers are represented by clear rectangles in a and b; in c and d, these rectangles indicate stacked aromatic residues. In (D), the view is from the center of the aqueous pore. The polypeptide segments are color-coded as in Figure 13.

subunit to fix the position of the two β-strands in the proper register and at the proper angle relative to the plane of the membrane (Figure 27C). The hydrogen bonding between the now-aligned β1 and β4 strands in adjacent monomers in the prepore complex then causes the unfolding of the TMH helices in each subunit and nucleates the edgewise association of the elongated β-hairpins into an extended β-sheet, followed by (or coincident with) the cooperative (Hotze et al., 2002) insertion of the hydrogen-bonded TMHs into the membrane to form the pore (Heuck et al., 2003) (Figure 27D).

The order of the steps involved in β1-β4 alignment and TMH unfolding (Figure 27D) has not been determined experimentally, and may actually be reversed. We arbitrarily placed alignment ahead of unfolding above only because β1 and β4 seem more likely to orient themselves relative to each other when there are fewer opportunities to form hydrogen bonds between the strands. However, the TMHs are not exposed to the nonpolar interior of the bilayer in the membrane-bound prepore complex (Heuck et al., 2003).

The data of Figures 18 and 19 provide compelling evidence for the coupling of the conformation of D4 with that of D3 to coordinate PFO binding to the membrane with PFO oligomerization. We had previously shown that the spatially-distant D3 and D4 conformations were coupled (Heuck et al., 2000), but the functional ramifications of that structural linkage were not clear until now. The conformational changes elicited by PFO binding to the membrane extend throughout most, if not all, of the PFO molecule and thereby demonstrate the delicate balance of forces that maintain PFO in its water-soluble monomeric conformation, poised to initiate the above structural changes that lead to the stable SDS-resistant membrane-inserted oligomer.

A very effective and efficient mechanism appears to have evolved to ensure that a peptide bond hydrogen in the extended β1 strand of one PFO molecule makes a hydrogen bond with the correct peptide bond carbonyl oxygen in the extended β4 strand of the adjacent PFO in the oligomer, thereby ensuring that the TMHs are aligned at the proper angle to insert into the membrane (Figures 23-26). The association of aromatic π-electron systems provides sufficient free energy to stably bind Y181 to F318, and thereby position β1 and β4 next to each other in the proper register. The same stacking phenomenon led to the stable association of pyrene dyes attached to β1 and β4 (Figures 21, 22), and also stabilizes RNA and DNA structures, and the assembly of β-sheet-rich amyloid fibrils containing short aromatic-containing peptides (Gazit, 2002).

The coupling of membrane binding to the unmasking of the oligomerization site on PFO may be common to all or most cytolysins. A comparison of the crystal structures of membrane-embedded *S. aureus* α-HL (Song et al., 1996) and the water-soluble monomer of its LukF homologue (Olson et al., 1999) suggests that the N-terminus of the αHL is folded into an interface surface in the monomer and interacts with the core β-sheet in the neighboring subunit in the heptamer (Montoya and Gouaux, 2003). Although the kinetics of membrane binding and N-terminus rearrangement have not been measured for αHL, it is reasonable to presume that αHL binding to the membrane surface elicits a conformational change that promotes heptamer formation and stabilization.

The strategy used by PFO, and presumably by all other CDCs, to prevent premature oligomerization in solution is not uncommon among β-sheet-containing proteins. A recent study of β-sheet structures in native proteins found that edge-to-edge association of β-strands of individual protein molecules was frequently prevented either by sterically covering a β-strand edge or by hydrogen-bonding a short stretch of polypeptide to the exposed β-strand edge similar to that seen with β5 in PFO (Richardson and Richardson, 2002). Interestingly, PFO employs both of these approaches to prevent premature oligomerization (Figure 13).

CHAPTER V

TOPOGRAPHY OF MEMBRANE-BOUND PFO AT DIFFERENT STAGES OF PORE FORMATION

Introduction

The transition of the water-soluble PFO monomer into a membrane-inserted oligomer involves extensive changes in protein conformation that have been the focal point of research among investigators during the past few years. Using the crystal structure of the PFO monomer (Rossjohn et al., 1997), a repertoire of site-specifically mutagenized PFO derivatives, and multiple independent fluorescence techniques, several structural states and rearrangements have been identified along with various protein-lipid and protein-protein interactions that mediate the conformational changes. D4, located at one end of the elongated PFO monomer (Figure 28), is responsible for membrane recognition and initial binding (Heuck et al., 2000), but only the tip of this domain is embedded in the nonpolar interior of the bilayer (Ramachandran et al., 2002). D4-lipid interactions trigger conformational changes in the spatially-distant D3 that expose a previously-hidden interface for oligomerization and hence prepore complex formation (Ramachandran et al., 2004). Two sets of three short α-helices in D3 then undergo an α-helix-to-β-sheet transition to create two TM β-hairpins, TMH1 and TMH2, per monomer that are then inserted into the bilayer (Shepard et al., 1998; Shatursky et al., 1999). This insertion also occurs in stages since the TMHs are not exposed to the nonpolar core of the bilayer in the prepore complex (Heuck et al., 2003). The conversion of PFO from a

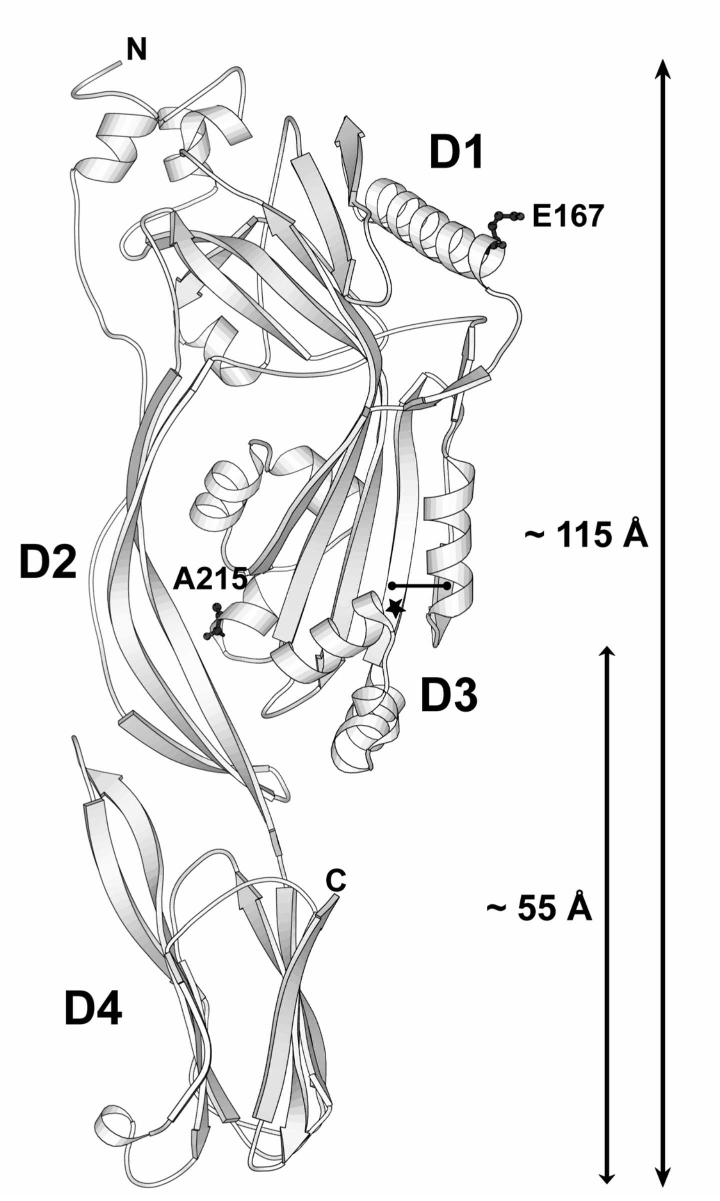

Figure 28. PFO dimensions and locations of mutations. Ribbon representation of the crystal structure of monomeric water-soluble PFO (Rossjohn et al., 1997) is shown. Either E167 in D1 or A215 in D3 was substituted with a Cys for BODIPY-labeling. Locations of the two residues substituted with Cys that introduce an intramolecular disulfide bond are shown by a "cross-bar", while the location of the F318A mutation is represented by a "star". The image was generated using MOLSCRIPT (Kraulis, 1991).

water-soluble monomer to a membrane-inserted oligomer therefore involves the structural coupling of D3 and D4 (Heuck et al., 2000; Ramachandran et al., 2004).

The crystallized PFO monomer is elongated in shape and measures about 115 Å in its longest dimension (Rossjohn et al., 1997) (Figure 28). Since D4 remains peripheral to the bilayer throughout pore formation and is oriented with its long axis nearly perpendicular to it (Ramachandran et al., 2002), PFO may bind to the target membrane surface in an 'end-on' orientation (Figure 29i) and interact with the membrane only via the hydrophobic loops of D4. If this were true, the polypeptide stretches in D3 that eventually form TMHs 1 and 2 would be located > 40 Å above the membrane surface prior to insertion (Figure 28). Major conformational changes would then be necessary to bring the TMHs in D3 to the bilayer surface for insertion.

Consistent with the above idea, a recent atomic force microscopy (AFM) study reported a significant difference in the height above the membrane surface of the prepore complex (113 ± 5 Å) and the inserted pore complex (73 ± 5 Å) (Czajkowsky et al., 2004). This study also indicated, consistent with earlier work (Heuck et al., 2003), that the polypeptide segments destined to form the TMHs are not in contact with the bilayer at the prepore stage of pore formation. The AFM data therefore suggest that the PFO molecule undergoes a 'vertical collapse' on the membrane surface during the prepore-to-pore transition as the TMHs are inserted into the membrane bilayer.

While the AFM study revealed the existence of a major structural reorganization of PFO during the prepore-to-pore transition, the domain specificity of the rearrangement was not addressed. Moreover, the AFM study did not examine the initial

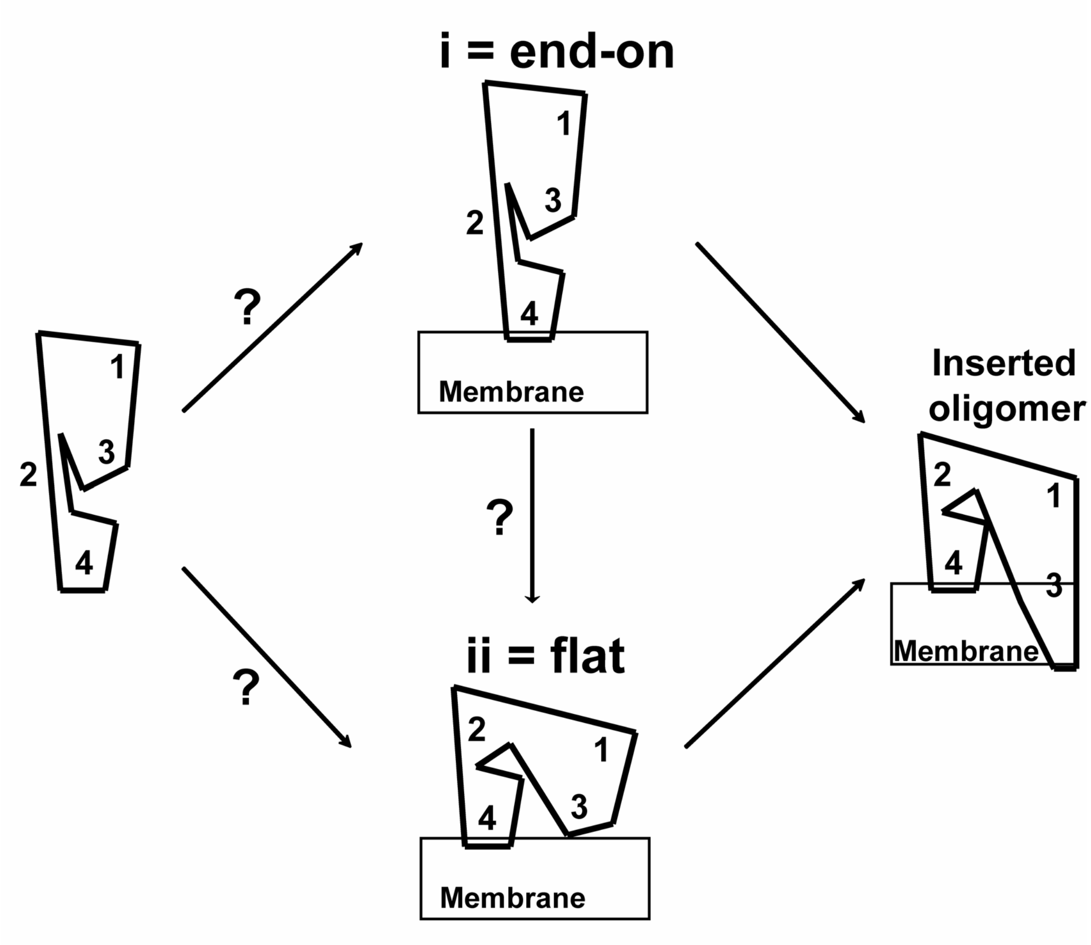
i = end-on
1
2
3
4
Membrane
?
?
?
1
2
3
4
Inserted
oligomer
2
1
4
3
Membrane
ii = flat
2
1
4
3
Membrane

Figure 29. Conceivable orientations of PFO on the membrane surface. Cartoons of potential domain rearrangements as PFO first binds to the membrane and then oligomerizes before forming the inserted pore complex. i represents an 'end-on' orientation of the membrane-bound PFO monomer, while ii represents a 'flat' orientation.

topography of PFO immediately after binding to the membrane, prior to oligomerization. Hence, in this study, we sought to provide specific information about the nature of the PFO-membrane complex before oligomerization, as well as to monitor the topography of two PFO domains above the membrane surface at every step of the pore formation process. Specifically, what is the orientation of the PFO molecule when it first binds to the membrane surface? Does it bind to the membrane surface in an "end-on" or a "flat" orientation (Figure 29i or 29ii)? What domain-specific conformational changes occur during the transition between the membrane-bound monomer and the membrane-bound oligomer? How far from the membrane surface are the D3 TMHs prior to insertion?

Fluorescence resonance energy transfer (FRET) measurements between the membrane surface and different domains of the PFO molecule at each stage of pore formation reveal that the PFO molecule is initially anchored in an 'end-on' orientation, with the long axis of the molecule nearly perpendicular to the plane of the bilayer. Monomer-monomer association and subsequent prepore complex formation does not greatly alter the height of the molecule relative to the membrane surface. Also, the D3 TMHs are located are far above the membrane surface prior to insertion. But while major changes in the overall topography of the PFO molecule occur during the prepore-to-pore transition of the oligomer, D1 still is located farthest from the membrane surface.

Results

Experimental rationale and design

D4 is responsible for membrane recognition and the initial binding of PFO to the membrane bilayer (Heuck et al., 2000). Furthermore, D4 projects nearly perpendicularly from the bilayer surface in the membrane-inserted PFO oligomer (Ramachandran et al., 2002). These results are consistent with the notion that the water-soluble monomer arrives ‘end-on’ at the membrane surface and is initially anchored by D4 to the membrane with its long axis perpendicular to the plane of the membrane bilayer as depicted in Figure 29i. However, since the TMHs of PFO originate from the spatially-distant D3, it is also possible that PFO might bind to the membrane so that D3 is positioned close to the membrane surface as depicted in Figure 29ii. Moreover, these models are not mutually exclusive because there is a distinct possibility that PFO initially anchors itself to the membrane in an ‘end-on’ orientation and then relatively quickly undergoes conformational changes that bring D3 into close proximity with the membrane surface for TMH insertion. Hence, to identify the conformational changes associated with pore formation into a membrane, we have directly determined the locations of D1 and D3 relative to the membrane surface at different stages of pore formation using FRET.

FRET is an excellent method for identifying conformations and detecting conformational changes, as well as for measuring the magnitude of a conformational change within a distance range of 20-100 Å (Stryer, 1978). The typical FRET experiment requires two fluorescent molecules, a ‘donor’ (D) and an ‘acceptor’ (A), that are each located at a specific site in the same or different molecule(s). After excitation by the absorption of a photon, an excited D can non-radiatively transfer its excited-state energy to an appropriate A under certain circumstances. The efficiency of this energy transfer depends primarily upon the extent of the overlap between D’s emission and A’s absorption spectra, the relative orientation of the D and A transition dipoles, and the distance between D and A. Donor emission intensity is reduced by FRET and the magnitude of this decrease is used to measure the extent of energy transfer. FRET has been primarily used to measure point-to-point distances between two sites within a molecule or between two molecules (e.g. Johnson et al., 1982; Watson et al., 1995; Woolhead et al., 2004).

A variation of the FRET technique allows one to measure the distance between two parallel planes. Such an experimental situation is created when a protein binds to a membrane surface. The membrane or vesicle surface therefore provides one plane, and for large vesicles with low curvature, this surface approximates an infinite plane. If all bound proteins adopt the same conformation, then a site (amino acid or a probe) on the protein constitutes the second infinite plane because the site will be located at the same height above the membrane for all proteins. Covalently attaching a D dye (here, BODIPY) to a single site in each protein molecule and then binding these proteins to a vesicle that contains a phospholipid with a charged A dye covalently attached to the headgroup (here, Rh-PE) to localize it at the surface therefore allows one to determine the height of D above the membrane. Since the Rh-PE molecules freely diffuse laterally in the membrane, quantification of the height requires using analytical expressions that assume a random and uniform distribution of A on the membrane surface. We have used this approach to determine the locations above the membrane surface, of the active sites of several membrane-bound blood coagulation enzymes, and to quantify coagulation cofactor-dependent alterations in those locations that appear to be functionally important

(Isaacs et al., 1986; Husten et al., 1987; Lu et al., 1989; Armstrong et al., 1990; Mutucumarana et al., 1992; McCallum et al., 1996; McCallum et al., 1997; Yegneswaran et al., 1997; Yegneswaran et al., 1999).

PFO derivatives trapped at different stages of pore formation

We have previously shown that an intramolecular disulfide bond engineered between Cys residues substituted at positions 319 (T319C) and 334 (V334C) in D3 traps PFO as a membrane-bound monomer in the absence of reducing agent (Ramachandran et al., 2004). Hereafter, rPFO(T319C V334C) will be referred to as rPFO^{DS} to denote the presence of the intramolecular disulfide bond. To determine the locations of D1 and D3 relative to the membrane surface at the membrane-bound monomer stage of pore formation, we introduced into rPFO^{DS} a third Cys residue located either at position 167 in D1 or position 215 in D3 TMH1 (Figure 28) and labeled this third free Cys with BODIPY to yield rPFO^{DS}(E167C-BODIPY) or rPFO^{DS}(A215C-BODIPY), respectively. In the presence of the reducing agent DTT, these intramolecularly disulfide-bonded molecules readily formed pores in cholesterol-containing membranes, and hence were fully functional after being released to accomplish the monomer-to-oligomer transition by removing the disulfide bond.

To block PFO insertion at the prepore stage of pore formation, we used a point mutant in PFO (F318A) that prevented TMH insertion and thereby arrested the PFO oligomer in the prepore state (Ramachandran et al., 2004). In the F318A background, a single Cys was introduced at either position 167 or at position 215 in two separate rPFO mutants and labeled with BODIPY to yield rPFO(F318A, E167C-BODIPY) and rPFO(F318A, A215C-BODIPY), respectively.

Spectral properties of BODIPY-labeled rPFO derivatives

The quantum yields of rPFO derivatives labeled at either position 167 or position 215 were determined experimentally to be 0.65 and 0.74, respectively, using soluble, unreduced rPFO^{DS}(E167C-BODIPY) and rPFO^{DS}(A215C-BODIPY). Since the fluorescence lifetimes of the BODIPY-labeled rPFO derivatives (5.0 ± 0.2 ns) did not change appreciably after incubation with cholesterol-containing membranes (data not shown), we conclude that the quantum yields of the BODIPY dyes attached to these positions do not change as the protein progresses through all stages of pore formation.

Interestingly, however, significant differences were observed in the steady-state anisotropy values of the BODIPY dye attached to position 167 in D1 of rPFO derivatives trapped at different stages of pore formation. Anisotropy values of 0.20, 0.15, and 0.12 were determined for oxidized rPFO^{DS}(E167C-BODIPY), rPFO(F318A E167C-BODIPY), and reduced rPFO^{DS}(E167C-BODIPY), respectively, after incubation with cholesterol-containing membranes (see below). These data indicate that the rotational freedom of the BODIPY dye in D1 increases during pore formation, though the exact nature of this change remains undefined. In contrast, very little change was seen in the anisotropy of the BODIPY dye (0.21 ± 0.01) attached to position 215 in D3 at different stages of pore formation (see below). Hence, the rotational freedom of the BODIPY dye in D3 is essentially the same before and after membrane insertion.

Topography of PFO as a membrane-bound monomer

To determine whether the PFO monomer initially binds to the membrane in an 'end-on' or a 'flat' orientation (Figure 29i or 29ii), we measured FRET between Rh-PE molecules located at the membrane surface and rPFO^{DS}(E167C-BODIPY) that was trapped in the monomeric state after binding to the membrane. When this mutant was bound to Rh-PE-containing membranes in the absence of DTT, essentially no energy transfer was observed from position 167 in D1 to Rh-PE at the membrane surface even at high acceptor density (Figure 30A), thereby demonstrating that the PFO molecule is stably bound to the membrane surface as a monomer in an 'end-on' orientation (Figure 29i). A 'flat' orientation (Figure 29ii) would have positioned the BODIPY dye in D1 much closer to the membrane surface and significant energy transfer would have been observed. The distance of closest approach or height of the BODIPY probe above the membrane surface, L, must therefore be >110 Å.

We then determined the location of the D3 TMH segments in membrane-bound monomeric PFO relative to the membrane surface. Data from collisional quenching experiments indicate that the TMH residues do not come into contact with the hydrophobic core of the bilayer even at the prepore stage of pore formation (Heuck et al., 2003; Czajkowsky et al., 2004). Yet very little is known about the positioning of these TMH segments relative to the membrane surface prior to their insertion into the bilayer. To ascertain the location of the TMH segments prior to membrane insertion, we chose a location (A215C) that would ultimately place the donor probe on the hydrophobic side of the TM β-barrel in the inserted pore complex. We then measured

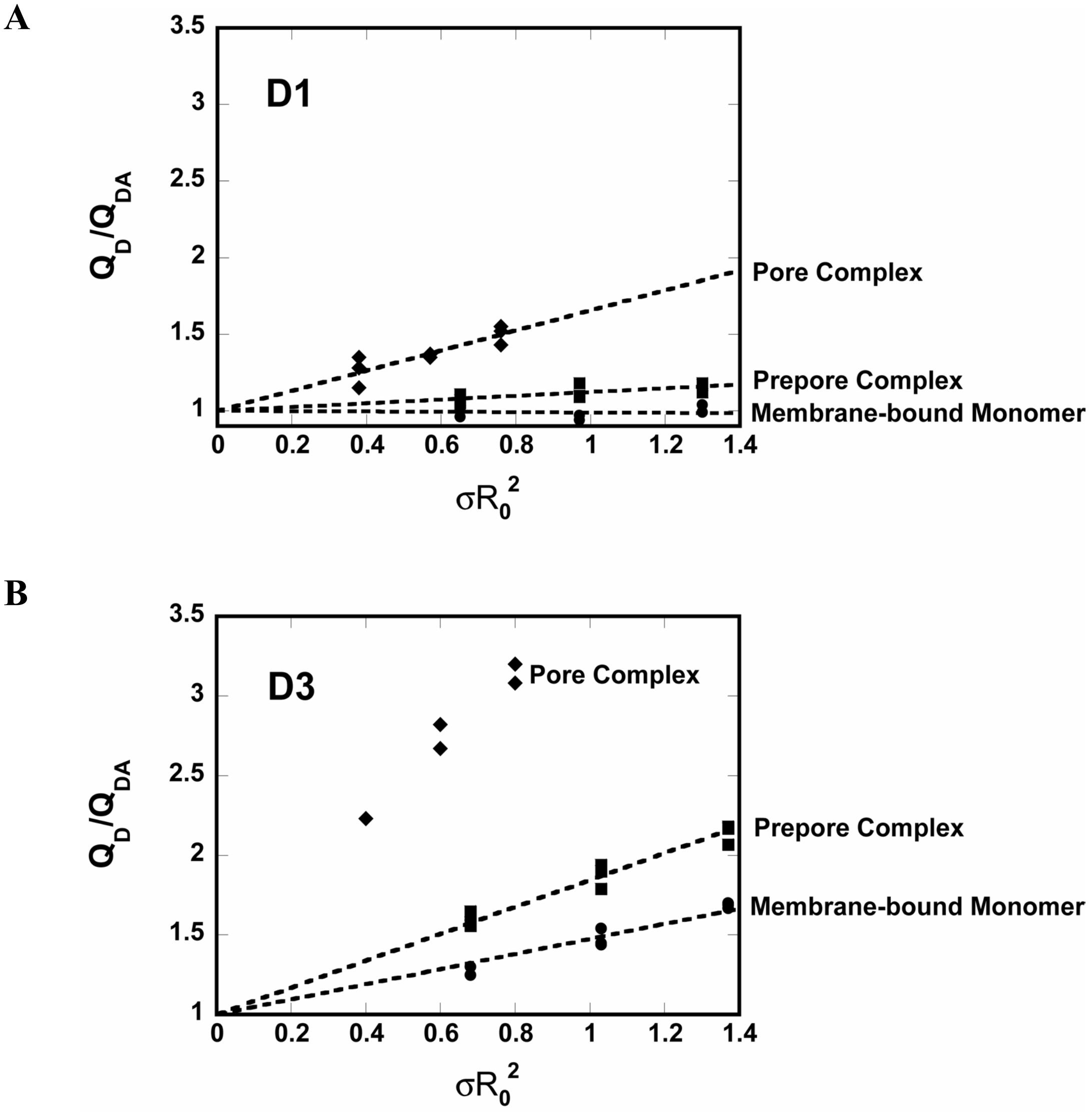

Figure 30. Dependence of energy transfer upon acceptor density. Q_D/Q_{DA} values for energy transfer between either D1 (A) or D3 (B) of each stage-trapped mutant and the membrane surface at 3 different acceptor densities (σ). The *lines* shown are the best-fit lines determined by linear regression as described under Experimental Procedures and have been required to go through position (0, 1).

the extent of energy transfer between unreduced rPFO^{DS}(A215C-BODIPY) and Rh-PE. Significant energy transfer was observed for rPFO^{DS}(A215C-BODIPY) (Figure 30B), and the height of this residue in TMH1 above the membrane surface was determined to be 72 ± 1 Å in the membrane-bound monomer. Since Q_D/Q_{DA} was found to be directly proportional to σR_0^2 over a range of σ values, as indicated by linear plots in Figures 30A and 30B, the approximation of Dewey and Hammes (1980) (eq. 6) can be used to calculate L. Thus, the TMHs are located far from the membrane surface at the initial stage of pore formation.

Topography of PFO in the prepore complex

To ascertain whether the topography of the membrane-bound PFO monomer changes significantly upon association with other monomers to form a prepore complex, we next measured the extent of energy transfer between Rh-PE and rPFO(F318A E167C-BODIPY) trapped at the prepore stage of pore formation. In this case, a small amount of energy transfer was observed (Figure 30A), indicating that the location and/or orientation of D1 and its probe relative to the membrane surface had changed somewhat upon forming an oligomeric prepore complex. The increased FRET efficiency could also be explained wholly or in part either by a translational movement by D1 towards the membrane surface or by a rotation of D1 and the BODIPY probe relative to the membrane surface that changes κ^2 (see below). The possibility of a rotational movement is supported by the fact that the rotational freedom of the donor dye significantly increases (anisotropy decreases from 0.20 to 0.15) upon monomer-monomer association. Yet whether or not D1 rotates upon monomer association, the data indicate that the PFO molecule is still oriented in a largely “end-on” orientation (Figure 29i) since the height of the BODIPY probe in D1 relative to the membrane surface is about 100 Å even in the prepore complex.

To determine whether monomer association and prepore formation cause the D3 TMH1 segment to move relative to the membrane surface, we measured the extent of energy transfer between rPFO(F318A A215C-BODIPY) and Rh-PE, and found that rPFO(F318A A215C-BODIPY) had a higher FRET efficiency in the prepore oligomer than did rPFO^{DS}(A215C-BODIPY) in the monomeric membrane-bound state (Figure 30B). Using eq. 6, the probe in TMH1 was determined to be 62 ± 1 Å above the membrane surface in the prepore complex.

The increased FRET efficiency observed for the D3 probe upon PFO association to form the oligomeric prepore complex can most likely be attributed largely or solely to a translational movement of the D3 TMHs towards the membrane surface since the anisotropy values for the BODIPY dye do not change significantly (0.21 vs. 0.20) between the membrane-bound monomer and the prepore complex. Thus, in the prepore complex, the D3 TMH1 segment is located closer to the membrane surface than in the membrane-bound monomeric form.

Topography of PFO in the pore complex

To estimate the location of D1 in the pore complex, we then measured the extent of energy transfer between Rh-PE and rPFO^{DS}(E167C-BODIPY) under reducing conditions (+ DTT) that readily allowed pore formation (Ramachandran et al., 2004). Under these conditions, a high FRET efficiency was observed between the probes in D1 in the membrane-inserted pore complex and Rh-PE at the membrane surface (Figure 30A). Using eq. 6, L was determined to be 74 ± 2 Å**.**

However, the above L value actually underestimates the extent of D1 movement towards the membrane because the Rh-PE is no longer distributed uniformly over a parallel plane after the pore is formed and the internal lipid "plug" is somehow lost to create the pore. Instead, a donor dye in a membrane-inserted PFO ring will transfer energy only to Rh-PE molecules that are located within a radius of about 110 Å (~ $2R_0$), and no acceptor dyes will be present in the newly-created 300 Å-diameter aqueous pore (Olofsson et al., 1993). To estimate the effect that pore formation would have on the surface density of Rh-PE around a BODIPY probe in a pore complex, we calculated the fraction of the area of a circle of radius 110 Å that would overlap with a circle of radius 150 Å if the donor dye were located at the edge of the pore (i.e., the center of the smaller circle was assumed to lie on the circumference of the larger circle). The extent of overlap under these conditions was 42%. It is therefore reasonable to assume that the surface density of Rh-PE molecules around each BODIPY-rPFO in an inserted pore complex is reduced on the order of 42%. Using this corrected σ value, L turns out to be 65 ± 1 Å. While this number constitutes only an estimate because of the assumptions made in its calculation, it is clear that the probe in D1 is located far from the membrane surface in the PFO pore complex. It is also clear that there is a major change in D1 location relative to the membrane surface upon pore formation, since it appears that the D1 probe moves (assuming that the change in FRET efficiency is due solely to translational movement of D1) from about 99 Å above the membrane surface to a height of about 65 Å above the surface.

As noted earlier, the location of residue 215 in the pore complex is fixed and known (Shatursky et al., 1999). Residue 215 in TMH1 faces the hydrophobic core of the membrane bilayer in the TM β-barrel and is located near the membrane surface. Therefore, in the pore complex, the BODIPY dye attached to this position in the reduced rPFO^{DS}(A215C-BODIPY) resides within the bilayer core. In this case, $L << R_0$ and donor dyes transfer significant excitation energy to acceptor molecules located on both sides of the membrane (but not in the pore, of course). Under these circumstances, the use of eq. 6 is invalid. However, this limitation is unimportant in this case because our previous studies have determined where A215 is located in the pore complex.

Dye orientation (κ^2) effects and uncertainties in L

The accuracy of the values determined for L (summarized in Table 5) is dependent upon the accuracy of the assumption that the transition dipoles of the donor and acceptor dyes are dynamically randomized during the excited-state lifetime of the donor so that $\kappa^2 = 2/3$. Since the BODIPY dyes attached to the protein and the rhodamine dyes attached to PE (Rh-PE) and located at the membrane surface do not rotate with complete freedom (Table 5), there is uncertainty in the experimentally determined R_0 and therefore, in L. Although κ^2 cannot be determined experimentally in a non-rigid sample, the theoretical upper and lower limits of κ^2, and hence of R_0, can be calculated from the anisotropy values of the donor (r_D) and the acceptor (r_A) that indicate the freedom of rotation of the dyes in the sample (Dale et al., 1979). From the measured

Table 5. Distance of closest approach determined by FRET

Domain	Membrane-bound state	Donor	r_D	Acceptor	r_A	L[a] (Å)
D1	Monomer	Oxidized rPFO^{DS}(E167C-BODIPY)	0.20	Rh-PE	0.26	–[b]
D1	Prepore	rPFO(F318A E167C-BODIPY)	0.15	Rh-PE	0.26	99 ± 2
D1	Pore	Reduced rPFO^{DS}(E167C-BODIPY)	0.12	Rh-PE	0.26	65 ± 1[c]
D3	Monomer	Oxidized rPFO^{DS}(A215C-BODIPY)	0.21	Rh-PE	0.26	72 ± 2
D3	Prepore	rPFO(F318A A215C-BODIPY)	0.20	Rh-PE	0.26	62 ± 1
D3	Pore	Reduced rPFO^{DS}(A215C-BODIPY)	0.22	Rh-PE	0.26	N.D.

[a] L was calculated using Equation 6 as described under "Experimental Procedures". Average values and standard deviations for 6 to 9 independent experiments are shown. The errors indicate experimental uncertainty of measurements and not uncertainties in κ^2 or R_0.

[b] No energy transfer was observed.

[c] This L value was determined using a reduced σ as discussed in the text.

N.D. not determined.

steady-state anisotropies of vesicle-bound BODIPY-labeled rPFO and Rh-PE (Table 5), the maximum uncertainty in R_0 due to orientation effects (κ^2) was calculated to range from -22% to +27%. However, assuming a value of $\kappa^2 = 2/3$ usually yields distances that differ by 10 % from those determined by crystallography when such comparisons can be made. This is true for both point-to-point (e.g. Stryer, 1978; Wu and Brand, 1992; also compare Johnson et al., 1982, with the structure of Yusupov et al., 2001) and plane-to-plane (compare McCallum et al., 1996, with Banner et al., 1996, and Yegneswaran et al., 1997 and 1999, with Adams et al., 2004) FRET measurements. Furthermore, because Rh-PE is oriented randomly in the plane of the membrane in the plane-to-plane FRET measurements done here, the uncertainty in R_0 due to orientation effects is further reduced.

Discussion

Our FRET measurements have provided four important insights into the topography of membrane-bound PFO at different stages of pore formation. First, in the membrane-bound monomeric state, the PFO molecule is anchored to the membrane in an 'end-on' orientation, with the long axis of the molecule nearly perpendicular to the plane of the bilayer. Second, monomer-monomer association and the formation of a prepore complex do not greatly alter the domain arrangement of individual PFO molecules relative to the membrane surface. Third, the D3 polypeptide segments that constitute the TMHs are far above the membrane surface even in the prepore complex, prior to insertion. Fourth, major changes in the overall topography and domain arrangement of the PFO molecule occur only during the prepore-to-pore transition of the oligomer.

FRET measurements between D1 of membrane-bound monomeric PFO and the membrane surface show conclusively that the elongated monomer is bound to the membrane in an ‘end-on’ orientation. Despite the fact that PFO is anchored to the bilayer by only a few residues at the tip of D4 that are located at one end of the molecule (Heuck et al., 2000; Ramachandran et al., 2002), D1 is stably positioned at the opposite end of the molecule more than 100 Å above the membrane surface. In addition, FRET measurements between D3 of membrane-bound monomeric PFO and the membrane surface show that TMH1 is ~ 72 Å above the membrane (Table 5). Thus, in the membrane-bound monomer stage of pore formation, the PFO molecule projects nearly perpendicularly from the plane of the membrane bilayer.

How do these distances relate to the dimensions of crystallized PFO (Rossjohn et al., 1997)? In the crystal structure, the longest dimension of the PFO monomer from the top of D1 to the tip of D4 is 115 Å (Figure 28; Rossjohn et al., 1997). If the PFO monomer initially binds to the membrane in a perpendicular orientation (Figure 29i), then the closest distance between the top of D1 and a phospholipid headgroup, after the insertion of the D4 loops into the bilayer core (Ramachandran et al., 2002), would be ~ 110 Å. If one then takes into account the lengths of the short tethers (~ 5 Å) that attach the BODIPY and the rhodamine dyes to the Cys residue and the phospholipid headgroup, respectively, then our FRET-determined distance of ≥ 100 Å between a BODIPY dye attached to the top of D1 to a rhodamine dye located at the membrane surface agrees well with an ‘end-on’ topography.

Also, in the ‘end-on’ orientation, the distance between residue 215 in D3 TMH1 and the membrane surface would be ~ 50 Å based on the crystal structure (Figure 28). However, this distance does not agree well with the FRET-determined height of 72 Å for the membrane-bound monomer (Table 5). This apparent discrepancy may be explained by the fact that D3 is poorly packed against D2 in the PFO crystal structure, and this induces a marked bend in the core β-sheet that connects D1 and D3 (Rossjohn et al., 1997), suggesting that D3 is capable of flexing away from the rest of the molecule. If such dynamic conformational flexibility does exist in solution, then it would not be surprising if D3 is, on average, positioned somewhat farther away from the membrane than is indicated by the solid-state structure and its crystal packing forces.

This structural arrangement, with an elongated protein projecting stably from a small 'footprint' on the membrane surface, is unusual. However, it is not unprecedented. Proteins involved in effecting and regulating blood coagulation are elongated, bind reversibly to appropriate membranes with small footprints, and extend approximately perpendicularly from the membrane with the enzyme active sites located 70-95 Å above the surface (Isaacs et al., 1986; Husten et al., 1987; Armstrong et al., 1990; Mutucumarana et al., 1992; McCallum et al., 1996; Yegneswaran et al., 1997). Intriguingly, these FRET studies revealed that the active site heights and/or orientations were altered in all but one case when the enzymes associated with the non-enzymatic protein cofactors that are required to achieve physiologically-significant reaction rates to either promote or prevent blood clot formation (Husten et al., 1987; Armstrong et al., 1990; McCallum et al., 1996; Yegneswaran et al., 1997). Since we later showed directly by protein engineering that the cofactor requirement for enzyme activity could be eliminated in one case by lowering the enzyme’s active site above the membrane surface (Yegneswaran et al., 1999), it appears that the cofactors regulate blood coagulation, at least in part, by positioning the enzyme active sites at the proper height and orientation above the phospholipid surface to cleave their membrane-bound substrates. It therefore seems reasonable to suggest that the unusual 'end-on' binding of PFO to the membrane may have evolved to provide a topographical mechanism for ensuring that protein-protein interactions occur in the proper sequence and thereby regulating the movement of PFO through the different stages of pore formation.

In the prepore complex, the height of D1 above the membrane surface was determined to be about 100 Å (Table 5). Since no energy transfer was observed between D1 and the membrane surface in membrane-bound monomeric PFO, and since the BODIPY dye in the prepore complex was found to rotate more freely than that in membrane-bound monomeric PFO (Table 5), the increased FRET may be due to a more favorable alignment of the donor and acceptor transition dipoles. Whatever the case, the small magnitude of the FRET efficiency demonstrates that even at the prepore stage of pore formation, D1 is still located far above the membrane surface and PFO is bound in an ‘end-on’ orientation in the prepore complex (Figure 29i).

Since PFO is presumably poised in this obligatory prepore intermediate (Heuck et al., 2003) to insert into the bilayer, an interesting and important structural question is where the D3 TMHs are located in the prepore complex. Are they positioned near or at the membrane surface just prior to insertion? Heuck et al. (2003) showed that residues in the TMHs were not exposed to the nonpolar interior of the membrane, but they did not further characterize TMH positioning. Here we have used the FRET approach to demonstrate that the height of the D3 TMH1 above the membrane surface is ~ 62 Å. This substantial height above the surface reveals that the TMHs in the prepore complex, supposedly 'poised' to insert into the bilayer, must still move a substantial distance to enter the membrane. For example, the fluorophore attached to TMH1 at position 215 must move from 62 Å above the membrane surface to a position located within the hydrophobic core of the bilayer. This major change in topography may explain, in part, why the prepore-to-pore conversion involves a substantial transition energy barrier that cannot be surmounted at low temperature (Heuck et al., 2003) or with some PFO mutants (Hotze et al., 2002; Ramachandran et al., 2004). The energy is presumably necessary to power the large conformational rearrangements that move the D3 TMHs to the membrane surface and then into the bilayer during the prepore-to-pore transition.

Also, the 10 Å reduction in TMH1 height above the membrane surface during the monomer-to-oligomer transition is not surprising because we have previously shown that D4 binding to the membrane triggers appreciable conformational changes in the spatially-distant D3 that expose an interface required for PFO oligomerization (Ramachandran et al., 2004). In unreduced rPFO^{DS} trapped in the membrane-bound monomeric state, these conformational changes are not elicited due to the presence of the intramolecular disulfide bond (Ramachandran et al., 2004). It therefore appears that one structural ramification of D4 binding to the membrane is a long-range conformational change in D3 that not only exposes the monomer-monomer interface surface (Ramachandran et al., 2004), but also moves D3 closer to the membrane surface by about 10 Å.

While TMH1 moves more than 60 Å during the prepore-to-pore transition, D1 appears to move about 34 Å closer to the membrane surface (Table 5). This number is only an estimate since the loss of acceptor dyes during pore formation complicates the determination of σ in the latter case. However, the FRET measurements agree very well with the heights of the prepore and pore complexes determined using AFM. Czajkowsky et al. (2004) reported a distance of 73 ± 5 Å between the top of the PFO pore complex and the membrane surface, which agrees well with the 65 ± 1 Å distance of closest approach between the D1 fluorophore and the acceptor dyes at the membrane surface (Table 5). The observed changes in the height of the PFO complex during the prepore-to-pore transition were also similar: ~ 40 Å for the AFM study (Czajkowsky et al., 2004) and ~ 34 Å (Table 5). Thus, two independent approaches agree on the magnitude of the structural change in the height of the PFO complex during pore formation. In addition, the FRET approach reveals that some PFO domain movements are even larger than indicated by monitoring the overall structure of the complex.

In summary, the water-soluble PFO monomer (Figure 31i) initially anchors itself to a cholesterol-containing target membrane in an ‘end-on’ orientation, with its long axis perpendicular to the plane of the membrane bilayer (Figure 31ii). At this stage, TMH-forming D3 segments are located ~ 72 Å above the membrane surface (Figure 31ii). Monomer-monomer association and subsequent prepore formation slightly lowers the

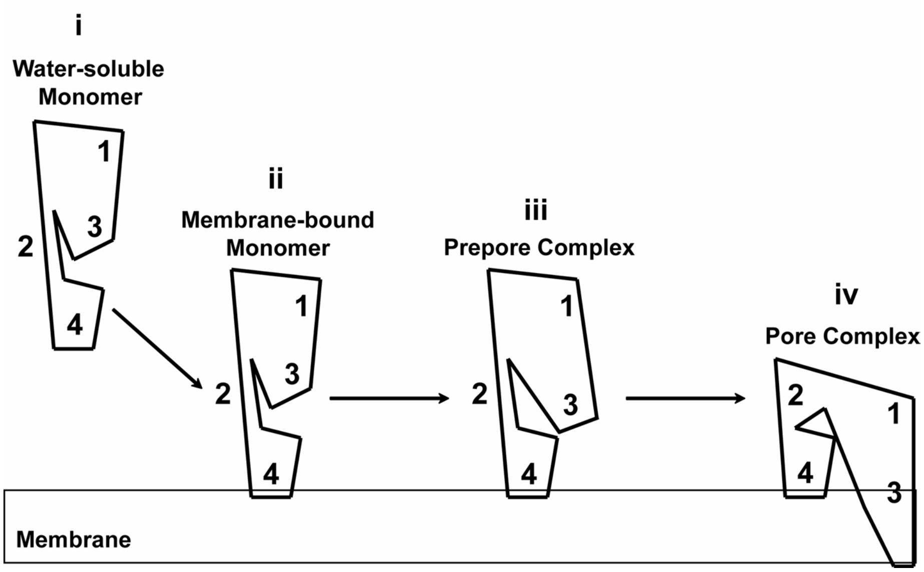

Figure 31. Model of the FRET-detected changes in PFO topography. A cartoon representation of the pathway of PFO pore formation depicting the orientation of membrane-bound PFO at different stages prior to membrane insertion is shown. Our FRET experiments reveal that water soluble PFO monomer (i) anchors itself to the membrane surface in an 'end-on' orientation with the long axis of the molecule nearly perpendicular to the plane of the membrane bilayer (ii). At this stage, the TMHs are located far (~ 70 Å) above the membrane bilayer. Prepore formation slightly reduces the height of the molecule above the membrane surface (iii), as well as the height of TMH1 in D3 above the membrane surface. During the prepore-to-pore transition, the molecule experiences a significant reduction in height (from ~ 100 Å to 65 Å) that brings D1 closer to the membrane surface, while TMH1 in D3 is inserted into the nonpolar core of the bilayer as part of the TM β-barrel. For simplicity, only one monomer in the prepore (iii) and pore (iv) complexes are shown.

heights of both D1 and D3 above the membrane surface (Figure 31iii). Concomitant with the prepore-to-pore transition, the molecule experiences a marked reduction in height above the membrane surface from ~ 100 Å in the prepore complex to ~ 65 Å in the membrane-inserted pore complex (Figure 31iv). Since D4 projects perpendicularly from the membrane even in the pore complex (Ramachandran et al., 2002), the reduction in height is presumably caused by a downward collapse of D2, as suggested by Czajkowsky et al. (2004). Thus, major topographical changes in PFO structure accompany pore formation as depicted in Figure 31.

In general, the changes in protein conformation that accompany the transition of several pore-forming toxins from one stably-folded state in water to a differently-folded membrane-inserted state within the target bilayer have been noted to be relatively modest (Montoya et al., 2003; Collier and Young, 2003). For example, in the case of the *S. aureus* α-HL, the TM β-hairpin that each monomer contributes to the 14-stranded β-barrel originates simply as an extension of its core β-sheet with minimal changes to either the secondary structure or the topography of its oligomeric prepore complex on the membrane surface (Song et al., 1996; Olson et al., 1999; Montoya et al., 2003). However, as described here, the changes in both PFO secondary structure and topography are substantial during pore formation, thereby demonstrating that the mechanisms of pore formation differ for CDCs and other toxins.

CHAPTER VI

SUMMARY

Using multiple independent fluorescence techniques as primary tools, the research presented in this dissertation has elucidated the mechanisms by which, the pore-forming toxin PFO from *C. perfringens*, binds to, and oligomerizes on the surface of, cholesterol-containing membranes. In addition, the topography of the molecule relative to the membrane surface at each stage of pore formation has been determined.

In summary, D4, the domain that first interacts with the target membrane anchors PFO to the membrane surface via the short hydrophobic loops at the tip of its β-sandwich. Only these loops are exposed to the nonpolar core of the bilayer, while the remainder of D4 is surrounded by water. D4 projects vertically from the membrane surface and its orientation relative to the membrane surface remains unaltered even after pore formation. Moreover, D4 makes little or no contact with neighboring monomers in the oligomer. Thus, initial binding of PFO to the target membrane is accomplished. The impact of these findings and the role of D4 in pore formation have been discussed in detail in Chapter III.

Membrane binding elicits multiple structural rearrangements in PFO that initiate and regulate its oligomerization. D4-membrane interactions trigger the movement of a loop in the spatially-distant D3 that exposes the edge of a previously-hidden β-strand. This β-strand interacts with an already-exposed β-strand of an adjacent monomer to form the monomer-monomer interface. The exposure of this β-strand is necessary for productive collisional encounters between membrane-bound PFO monomers on the membrane surface and the formation of a large, circular prepore complex. Remarkably, the β-strands that form the interface each contain a single aromatic residue, and these aromatics appear to stack to align the TMHs of adjacent monomers in the proper register for insertion. Thus, membrane-dependent conformational changes initiate and regulate oligomerization and pore formation. The significance of these fndings is discussed in Chapter IV.

FRET measurements revealed the topography of PFO relative to the membrane surface at each stage of pore formation. The elongated PFO monomer is initially anchored to the membrane surface in an ‘end-on’ orientation with its long axis nearly perpendicular to the plane of the membrane bilayer. This orientation remains relatively unaltered even upon monomer-monomer association and prepore complex formation. However, the oligomeric complex undergoes a significant collapse in height concomitant with membrane insertion and pore formation. Furthermore, the polypeptide segments that constitute the TMHs are located far above the membrane surface even at the prepore complex stage of pore formation, thereby indicating that the major topographical changes in PFO occur during the prepore-to-pore transition of the oligomer. The importance of these findings is discussed in Chapter V.

The results from this study have thus helped bridge many of the gaps that exist in our current knowledge of CDC pore formation. However, many intriguing questions still remain. For example, the trigger for the helix-to-sheet conversion in D3 is unknown. It is tempting to believe that exposure of the TMH-forming α-helices to the low dielectric constant environment of the lipid-water interface (White and Wimley, 1999) triggers this event. However, till date, no experiments have been targeted at addressing this issue. How are the lipids in the middle of the circular, oligomeric prepore complex displaced to create the large aqueous pore? This poses a conceptual problem because creation of a 300 Å pore requires the displacement of more than a 1000 lipid molecules from the middle of the oligomeric complex. How this is accomplished concomitant with TMH insertion remains obscure and demands further experimentation. Finally, and most important, the exact role of cholesterol in the pore formation process is still unclear. Do CDCs have a specific binding site for cholesterol? If so, what is the stoichiometry of the PFO:cholesterol complex? Answers to these questions have been hard to come by and demand ingenuity and creativity in experimental design.

REFERENCES

Adams, T.E., Hockin, M.F., Mann, K.G., and Everse, S.J. (2004). The crystal structure of activated protein C-inactivated bovine factor Va: implications for cofactor function. Proc. Natl. Acad. Sci. *101*, 8918-8923.

Alouf, J.E. (1999). Introduction to the family of the structurally related cholesterol-binding cytolysins (‘sulfhydryl-activated’ toxins). In The Comprehensive Sourcebook of Bacterial Protein Toxins, J. E. Alouf and J. H. Freer, eds. (London: Academic Press), 443-456.

Alouf, J.E. (2000). Cholesterol-binding cytolytic protein toxins. Int. J. Med. Microbiol. *290*, 351-6.

Alouf, J.E. (2001). Pore-forming bacterial protein toxins: an overview. Curr. Top. Microbiol. Immunol. *257*, 1-14.

Alouf, J.E., and Freer, J.H., eds. (1999). The Comprehensive Sourcebook of Bacterial Protein Toxins. Second edition. (London: Academic Press).

Armstrong, S.A., Husten, E.J., Esmon, C.T., and Johnson, A.E. (1990). The active site of membrane-bound meizothrombin. A fluorescence determination of its distance from the phospholipid surface and its conformational sensitivity to calcium and factor Va. J. Biol. Chem. *265*, 6210-6218.

Baird, B., and Holowka, D. (1985). Structural mapping of Fc receptor bound immunoglobulin E: proximity to the membrane surface of the antibody combining site and another site in the Fab segments. Biochemistry *24*, 6252-6259.

Banner, D.W., D'Arcy, A., Chene, C., Winkler, F.K., Guha, A., Konigsberg, W.H., Nemerson, Y., and Kirchhofer, D. (1996). The crystal structure of the complex of blood coagulation factor VIIa with soluble tissue factor. Nature *380*, 41-46.

Billington, S.J., Jost, B.H., and Songer, J.G. (2000). Thiol-activated cytolysins: structure, function and role in pathogenesis. FEMS Microbiol. Lett. *182*, 197-205.

Buchanan, S.K. (1999). β-barrel proteins from bacterial outer membranes: structure, function and refolding. Curr. Opin. Struct. Biol. *9*, 455-461.

Buckley, J.T. (1999). The channel-forming toxin aerolysin. In The Comprehensive Sourcebook of Bacterial Protein Toxins, J. E. Alouf and J. H. Freer, eds. (London: Academic Press), 362-372.

Choe, S., Bennett, M.J., Fujii, G., Curmi, P.M.G., Kantardjieff, A.K., Collier, R.J., and Eisenberg, D. (1992). The crystal structure of diphtheria toxin. Nature *357*, 216-222.

Collier, R.J., and Young, J.A. (2003). Anthrax toxin. Annu. Rev. Cell Dev. Biol. *19*, 45-70.

Crowley, K.S., Reinhart, G.D., and Johnson, A.E. (1993). The signal sequence moves through a ribosomal tunnel into a noncytoplasmic aqueous environment at the ER membrane early in translocation. Cell *73*, 1101-1115.

Crowley, K.S., Liao, S., Worrell, V.E., Reinhart, G.D., and Johnson, A.E. (1994). Secretory proteins move through the endoplasmic reticulum membrane via an aqueous, gated pore. Cell *78*, 461-471.

Czajkowsky, D.M., Hotze, E.M., Shao, Z., and Tweten, R.K. (2004). Vertical collapse of a cytolysin prepore moves its transmembrane β-hairpins to the membrane. EMBO J. *23*, 3206-3215.

Dale, R.E., Eisinger, J., and Blumberg, W.E. (1979). The orientational freedom of molecular probes. The orientation factor in intramolecular energy transfer. Biophys. J. *26*, 161-194.

Dewey, T.G., and Hammes, G.G. (1980). Calculation of fluorescence resonance energy transfer on surfaces. Biophys. J. *32*, 1023-1036.

Dufourcq, J., Castano, S., and Talbot, J. (1999). δ-toxin, related haemolytic toxins and peptidic analogues. In The Comprehensive Sourcebook of Bacterial Protein Toxins, J. E. Alouf and J. H. Freer, eds. (London: Academic Press), 386-401.

Fivaz, M., Abrami, L., Tsitrin, Y., and van der Goot, F.G. (2001). Aerolysin from *Aeromonas hydrophila* and related toxins. Curr. Top. Microbiol. Immunol. *257*, 35-52.

Gabriel, K., Buchanan, S.K., and Lithgow, T. (2001). The alpha and the beta: protein translocation across mitochondrial and plastid outer membranes. Trends Biochem. Sci. *26*, 36-40.

Gazit, E. (2002). A possible role for π-stacking in the self-assembly of amyloid fibrils. FASEB J. *16*, 77-83.

Giddings, K.S., Johnson, A.E., and Tweten, R.K. (2003). Redefining cholesterol's role in the mechanism of the cholesterol-dependent cytolysins. Proc. Natl. Acad. Sci. USA *100*, 11315-11320.

Gilbert, R.J.C., Rossjohn, J., Parker, M.W., Tweten, R.K., Morgan, P.J., Mitchell, T.J., Errington, N., Rowe, A.J., Andrew, P.W., and Byron, O. (1998). Self-interaction of pneumolysin, the pore-forming protein toxin of *Streptococcus pneumoniae*. J. Mol. Biol. *284*, 1223-1237.

Gordon, V.M., Nelson, K.L., Buckley, J.T., Stevens, V.L., Tweten, R.K., Elwood, P.C., and Leppla, S.H. (1999). *Clostridium septicum* alpha toxin uses glycosylphosphatidylinositol-anchored protein receptors. J. Biol. Chem. *274*, 27274-27280.

Gouaux, E. (1997). Channel-forming toxins: tales of transformation. Curr. Opin. Struct. Biol. *7*, 566-573.

Hamman, B.D., Hendershot, L.M., and Johnson, A.E. (1998). BiP maintains the permeability barrier of the ER membrane by sealing the lumenal end of the translocon pore before and early in translocation. Cell *92*, 747-758.

Heuck, A.P., Hotze, E.M., Tweten, R.K., and Johnson, A.E. (2000). Mechanism of membrane insertion of a multimeric beta-barrel protein: perfringolysin O creates a pore using ordered and coupled conformational changes. Mol. Cell *6*, 1233-1242.

Heuck, A.P., Tweten, R.K., and Johnson, A.E. (2001). β-barrel pore-forming toxins: intriguing dimorphic proteins. Biochemistry *40*, 9065-9073.

Heuck, A.P., and Johnson, A.E. (2002). Pore-forming protein structure analysis in membranes using multiple independent fluorescence techniques. Cell Biochem. Biophys. *36*, 89-101.

Heuck, A.P., Tweten, R.K., and Johnson, A.E. (2003). Assembly and topography of the prepore complex in cholesterol-dependent cytolysins. J. Biol. Chem. *278*, 31218-31225.

Hirst, T.R. (1999). Cholera toxin and *Escherichia coli* heat-labile enterotoxin. In The Comprehensive Sourcebook of Bacterial Protein Toxins, J. E. Alouf and J. H. Freer, eds. (London: Academic Press), pp. 104-129.

Hotze, E.M., Wilson-Kubalek, E.M., Rossjohn, J., Parker, M.W., Johnson, A.E., and Tweten, R.K. (2001). Arresting pore formation of a cholesterol-dependent cytolysin by disulfide trapping synchronizes the insertion of the transmembrane beta-sheet from a prepore intermediate. J. Biol. Chem. *276*, 8261-8268.

Hotze, E.M., Heuck, A.P., Czajkowsky, D.M., Shao, Z., Johnson, A.E., and Tweten, R.K. (2002). Monomer-monomer interactions drive the prepore to pore conversion of a beta-barrel-forming cholesterol-dependent cytolysin. J. Biol. Chem. *277*, 11597-11605.

Husten, E.J., Esmon, C.T., and Johnson, A.E. (1987). The active site of blood coagulation factor Xa. Its distance from the phospholipid surface and its conformational sensitivity to components of the prothrombinase complex. J. Biol. Chem. *262*, 12953-12961.

Isaacs, B.S., Husten, E.J., Esmon, C.T., and Johnson, A.E. (1986). A domain of membrane-bound blood coagulation factor Va is located far from the phospholipid surface. A fluorescence energy transfer measurement. Biochemistry *25*, 4958-4969.

Iwamoto, M., Ohno-Iwashita, Y., and Ando, S. (1987). Role of the essential thiol group in the thiol-activated cytolysin from *Clostridium perfringens*. Eur. J. Biochem. *167*, 425-430.

Iwamoto, M., Ohno-Iwashita, Y., and Ando, S. (1990). Effect of the isolated C-terminal fragment of theta-toxin (perfringolysin O) on toxin assembly and membrane lysis. Eur. J. Biochem. *194*, 25-31.

Jacobs, T., Cima-Cabal, M.D., Darji, A., Mendez, F.J., Vazquez, F., Jacobs, A.A., Shimada, Y., Ohno-Iwashita, Y., Weiss, S., and de los Toyos, J.R. (1999). The conserved undecapeptide shared by thiol-activated cytolysins is involved in membrane binding. FEBS Lett. *459*, 463-466.

Johnson, A.E., Adkins, H.J., Matthews, E.A., and Cantor, C.R. (1982). Distance moved by transfer RNA during translocation from the A site to the P site on the ribosome. J. Mol. Biol. *156*, 113-140.

Johnson, I.D., Kang, H.C., and Haugland, R.P. (1991). Fluorescent membrane probes incorporating dipyrrometheneboron difluoride fluorophores. Anal. Biochem. *198*, 228-37.

Karolin, J., Johansson, L.B.A., Strandberg, L., and Ny, T. (1994). Fluorescence and absorption properties of dipyrrometheneboron difluoride (BODIPY) derivatives in liquids, lipid membranes, and proteins. J. Am. Chem. Soc. *116*, 7801-7806.

Koronakis, V., Sharff, A., Koronakis, E., Luisi, B., and Hughes, C. (2000). Crystal structure of the bacterial membrane protein TolC central to multidrug efflux and protein export. Nature *405*, 914-919.

Kraulis, P.J. (1991). MOLSCRIPT: a program to produce both detailed and schematic plots of protein structures. J. Appl. Crystallogr. *24*, 946-950.

Lacy, D.B., and Stevens, R.C. (1998). Unraveling the structures and modes of action of bacterial toxins. Curr. Opin. Struct. Biol. *8*, 778-784.

Lakey, J.H., and Slatin, S.L. (2001). Pore-forming colicins and their relatives. Curr. Top. Microbiol. Immunol. *257*, 131-61.

Lecuyer, H., and Dervichian, D.G. (1969). Structure of aqueous mixtures of lecithin and cholesterol. J. Mol. Biol. *45*, 39-57.

Lehrer, S.S. (1997). Intramolecular pyrene excimer fluorescence: a probe of proximity and protein conformational change. Methods Enzymol. *278*, 286-295.

Locht, C., and Antoine, R. (1999). *Bordetella pertussis* protein toxins. In The Comprehensive Sourcebook of Bacterial Protein Toxins, J. E. Alouf and J. H. Freer, eds. (London: Academic Press), 130-146.

Lu, R.L., Esmon, N.L., Esmon, C.T., and Johnson, A.E. (1989). The active site of the thrombin-thrombomodulin complex. A fluorescence energy transfer measurement of its distance above the membrane surface. J. Biol. Chem. *264*, 12956-12962.

Madden, J.C., Ruiz, N., and Caparon, M. (2001). Cytolysin-mediated translocation (CMT): a functional equivalent of type III secretion in gram-positive bacteria. Cell *104*, 143-152.

Malovrh, P., Viero, G., Serra, M.D., Podlesek, Z., Lakey, J.H., Macek, P., Menestrina, G., and Anderluh, G. (2003). A novel mechanism of pore formation: membrane penetration by the N-terminal amphipathic region of equinatoxin. J. Biol. Chem. *278*, 22678-22685.

McCallum, C.D., Hapak, R.C., Neuenschwander, P.F., Morrissey, J.H., and Johnson, A.E. (1996). The location of the active site of blood coagulation factor VIIa above the membrane surface and its reorientation upon association with tissue factor. A fluorescence energy transfer study. J. Biol. Chem. *271*, 28168-28175.

McCallum, C.D., Su, B., Neuenschwander, P.F., Morrissey, J.H., and Johnson, A.E. (1997). Tissue factor positions and maintains the factor VIIa active site far above the membrane surface even in the absence of the factor VIIa Gla domain. A fluorescence resonance energy transfer study. J. Biol. Chem. *272*, 30160-30166.

Merritt, E.A., and Bacon, D.J. (1997). Raster3D photorealistic molecular graphics. Methods Enzymol. *277*, 505-524.

Montoya, M., and Gouaux, E. (2003). Beta-barrel membrane protein folding and structure viewed through the lens of alpha-hemolysin. Biochim. Biophys. Acta *1609*, 19-27.

Mutucumarana, V.P., Duffy, E.J., Lollar, P., and Johnson, A.E. (1992). The active site of factor IXa is located far above the membrane surface and its conformation is altered upon association with factor VIIIa. A fluorescence study. J. Biol. Chem. *267*, 17012-17021.

Naglich, J.G., Metherall, J.E., Russell, D.W., and Eidels, L. (1992). Expression cloning of a diphtheria toxin receptor: identity with a heparin-binding EGF-like growth factor precursor. Cell *69*, 1051-1061.

Nakamura, M., Sekino, N., Iwamoto, M., and Ohno-Iwashita, Y. (1995). Interaction of theta-toxin (perfringolysin O), a cholesterol-binding cytolysin, with liposomal membranes: change in the aromatic side chains upon binding and insertion. Biochemistry *34*, 6513-6520.

Nakamura, M., Sekino-Suzuki, N., Mitsui, K., and Ohno-Iwashita, Y. (1998). Contribution of tryptophan residues to the structural changes in perfringolysin O during interaction with liposomal membranes. J. Biochem. (Tokyo) *123*, 1145-1155.

Olofsson, A., Hebert, H., and Thelestam, M. (1993). The projection structure of perfringolysin O (Clostridium perfringens theta-toxin). FEBS Lett. *319*, 125-127.

Olson, R., Nariya, H., Yokota, K., Kamio, Y., and Gouaux, E.(1999). Crystal structure of staphylococcal LukF delineates conformational changes accompanying formation of a transmembrane channel. Nat. Struct. Biol. *6*, 134-140.

Palmer, M., Saweljew, P., Vulicevic, I., Valeva, A., Kehoe, M., and Bhakdi, S. (1996). Membrane-penetrating domain of streptolysin O identified by cysteine scanning mutagenesis. J. Biol. Chem. *271*, 26664-26667.

Palmer, M., Harris, R., Freytag, C., Kehoe, M., Tranum-Jensen, J., and Bhakdi, S. (1998). Assembly mechanism of the oligomeric streptolysin O pore: the early membrane lesion is lined by a free edge of the lipid membrane and is extended gradually during oligomerization. EMBO J. *17*, 1598-1605.

Petit, L., Gibert, M., and Popoff, M.R. (1999). *Clostridium perfringens*: toxinotype and genotype. Trends Microbiol. *7*, 104-110.

Pinkney, M., Beachey, E., and Kehoe, M. (1989). The thiol-activated toxin streptolysin O does not require a thiol group for activity. Infect. Immun. *57*, 2553-2558.

Portnoy, D.A., Auerbuch, V., and Glomski, I.J. (2002). The cell biology of *Listeria monocytogenes* infection: the intersection of bacterial pathogenesis and cell-mediated immunity. J. Cell Biol. *158*, 409-414.

Prevost, G., Mourey, L., Colin, D.A., and Menestrina, G. (2001). Staphylococcal pore-forming toxins. Curr. Top. Microbiol. Immunol. *257*, 53-83.

Ramachandran, R., Heuck, A.P., Tweten, R.K., and Johnson, A.E. (2002). Structural insights into the membrane-anchoring mechanism of a cholesterol-dependent cytolysin. Nat. Struct. Biol. *9*, 823-827.

Ramachandran, R., Tweten, R.K., and Johnson, A.E. (2004). Membrane-dependent conformational changes initiate cholesterol-dependent cytolysin oligomerization and intersubunit β-strand alignment. Nat. Struct. Mol. Biol. *11*, 697-705.

Richardson, J.S., and Richardson, D.C. (2002). Natural β-sheet proteins use negative design to avoid edge-to-edge aggregation. Proc. Natl. Acad. Sci. USA *99*, 2754-2759.

Rossjohn, J., Feil, S.C., McKinstry, W.J., Tweten, R.K., and Parker, M.W. (1997). Structure of a cholesterol-binding, thiol-activated cytolysin and a model of its membrane form. Cell *89*, 685-692.

Saunders, K.F., Mitchell, T.J., Walker, J.A., Andrew, P.W., and Boulnois, G.J. (1989). Pneumolysin, the thiol-activated toxin of *Streptococcus pneumoniae*, does not require a thiol group for in vitro activity. Infect. Immun. *57*, 2547-2552.

Schmitt, C.K., Meysick, K.C., and O'Brien, A.D. (1999). Bacterial toxins: friends or foes? Emerging Infectious Diseases *5*, 224-234.

Schulz, G.E. (2000). β-barrel membrane proteins. Curr. Opin. Struct. Biol. *10*, 443-447.

Sekino-Suzuki, N., Nakamura, M., Mitsui, K.I., and Ohno-Iwashita, Y. (1996). Contribution of individual tryptophan residues to the structure and activity of theta-toxin (perfringolysin O), a cholesterol-binding cytolysin. Eur. J. Biochem. *241*, 941-947.

Shatursky, O., Heuck, A.P., Shepard, L.A., Rossjohn, J., Parker, M.W., Johnson, A.E., and Tweten, R.K. (1999). The mechanism of membrane insertion for a cholesterol dependent cytolysin: a novel paradigm for pore forming toxins. Cell *99*, 293-299.

Shepard, L.A., Heuck, A.P., Hamman, B.D., Rossjohn, J., Parker, M.W., Ryan, K.R., Johnson, A.E., and Tweten, R.K. (1998). Identification of a membrane-spanning domain of the thiol-activated pore-forming toxin *Clostridium perfringens* perfringolysin O: an α-helical to β-sheet transition identified by fluorescence spectroscopy. Biochemistry *37*, 14563-14574.

Shepard, L.A., Shatursky, O., Johnson, A.E., and Tweten, R.K. (2000). The mechanism of assembly and insertion of the membrane complex of the cholesterol-dependent cytolysin perfringolysin O: formation of a large prepore complex. Biochemistry *39*, 10284-10293.

Song, L.Z., Hobaugh, M.R., Shustak, C., Cheley, S., Bayley, H., and Gouaux, J.E. (1996). Structure of staphylococcal alpha-hemolysin, a heptameric transmembrane pore. Science *274*, 1859-1866.

Spencer, R.D., and Weber, G. (1969). Measurements of subnanosecond fluorescence lifetimes with a cross-correlation phase fluorometer. Ann. New York Acad. Sci. *158*, 361-376.

Spencer, R.D., and Weber, G. (1970). Influence of brownian rotations and energy transfer upon measurements of fluorescence lifetime. J. Chem. Phys. *52*, 1654-1663.

Stevens, D.L., and Bryant, A.E. (1999). The pathogenesis of shock and tissue injury in *Clostridia* gas gangrene. In The Comprehensive Sourcebook of Bacterial Protein Toxins, J. E. Alouf and J. H. Freer, eds. (London: Academic Press), 623-636.

Stryer, L. (1978). Fluorescence energy transfer as a spectroscopic ruler. Annu. Rev. Biochem. *47*, 819-846.

Titball, R.W. (1999). Membrane-damaging and cytotoxic phospholipases. In The Comprehensive Sourcebook of Bacterial Protein Toxins, J. E. Alouf and J. H. Freer, eds. (London: Academic Press), 310-329.

Tweten, R.K., Harris, R.W., and Sims, P.J. (1991). Isolation of a tryptic fragment from *Clostridium perfringens* Θ-toxin that contains sites for membrane binding and self-aggregation. J. Biol. Chem. *266*, 12449-12454.

Tweten, R.K., Parker, M.W., and Johnson, A.E. (2001). The cholesterol-dependent cytolysins. Curr. Top. Microbiol. Immunol. *257*, 15-33.

Walker, B., Krishnasastry, M., Zorn, L., and Bayley, H. (1992). Assembly of the oligomeric membrane pore formed by staphylococcal alpha-haemolysin examined by truncation mutagenesis. J. Biol. Chem. *267*, 21782-21786.

Walker, B., Braha, O., Cheley, S., and Bayley, H. (1995). An intermediate in the assembly of a pore-forming protein trapped with a genetically-engineered switch. Chem. Biol. *2*, 99-105.

Watson, B.S., Hazlett, T.L., Eccleston, J.F., Davis, C., Jameson, D.M., and Johnson, A.E. (1995). Macromolecular arrangement in the aminoacyl-tRNA.elongation factor Tu.GTP ternary complex. A fluorescence energy transfer study. Biochemistry *34*, 7904-7912.

Weber, G., and Teale, F.W.J. (1956). Determination of the absolute quantum yield of fluorescent solutions. Trans. Faraday Soc. *53*, 646-655.

Weis, S., and Palmer, M. (2001). Streptolysin O: the C-terminal tryptophan-rich domain carries functional sites for both membrane binding and self-interaction but not for stable oligomerization. Biochim. Biophys. Acta *1510*, 292-299.

White, S.H., and Wimley, W.C. (1999). Membrane protein folding and stability: physical principles. Annu. Rev. Biophys. Biomol. Struct. *28*, 319-365.

Wimley, W.C. (2003). The versatile beta-barrel membrane protein. Curr. Opin. Struct. Biol. *13*, 404-411.

Woolhead, C.A., McCormick, P.J., and Johnson, A.E. (2004). Nascent membrane and secretory proteins differ in FRET-detected folding far inside the ribosome and in their exposure to ribosomal proteins. Cell *116*, 725-736.

Wu, P., and Brand, L. (1992). Orientation factor in steady-state and time-resolved resonance energy transfer measurements. Biochemistry *31*, 7939-7947.

Yegneswaran, S., Wood, G.M., Esmon, C.T., and Johnson, A.E. (1997). Protein S alters the active site location of activated protein C above the membrane surface. A fluorescence resonance energy transfer study of topography. J. Biol. Chem. *272*, 25013-25021.

Yegneswaran, S., Smirnov, M.D., Safa, O., Esmon, N.L., Esmon, C.T., and Johnson, A.E. (1999). Relocating the active site of activated protein C eliminates the need for its protein S cofactor. J. Biol. Chem. *274*, 5462-5468.

Yusupov, M.M., Yusupova, G.Z., Baucom, A., Lieberman, K., Earnest, T.N., Cate, J.H., and Noller, H.F. (2001). Crystal structure of the ribosome at 5.5 Å resolution. Science *292,* 883-896.

APPENDIX

SUPPORTING FIGURES

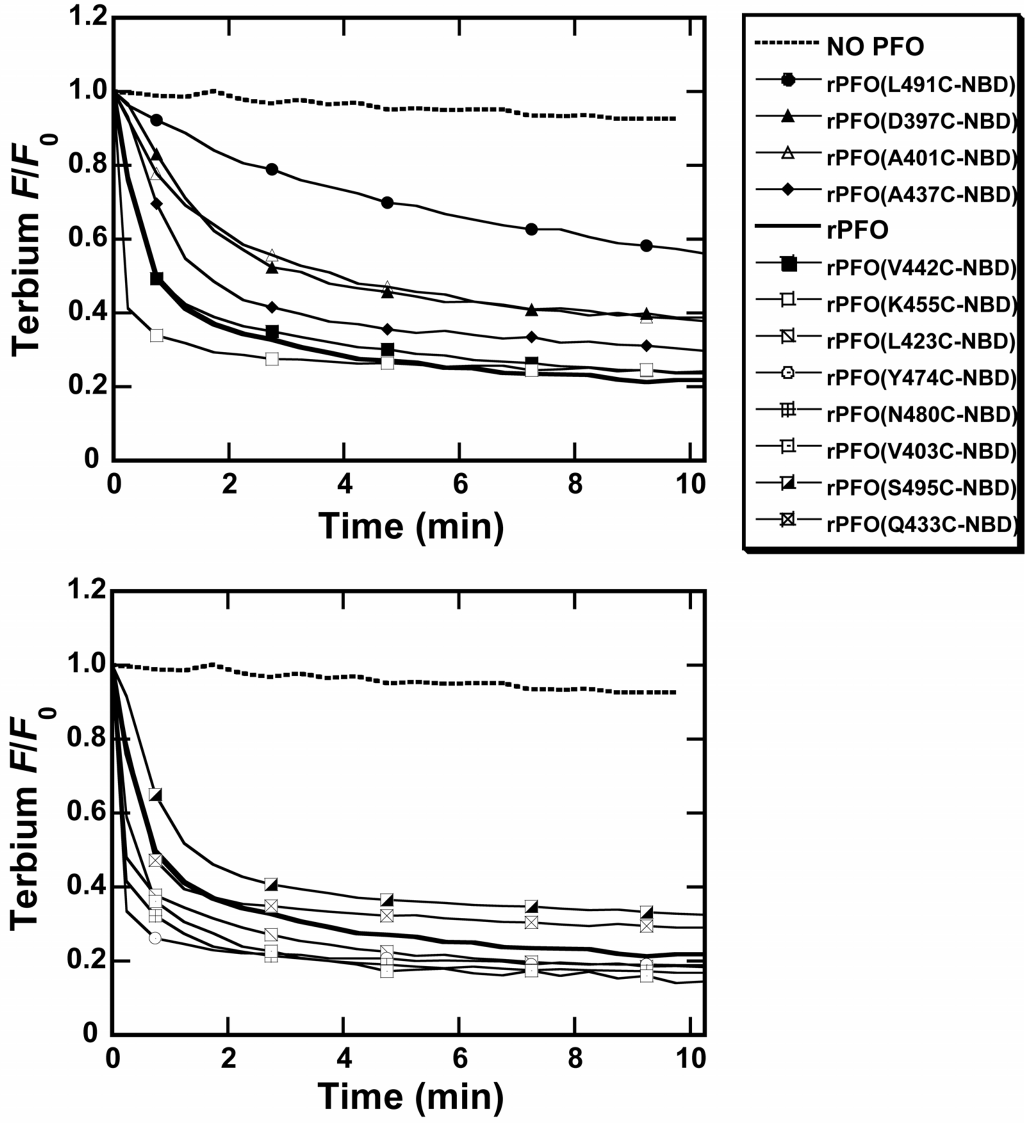

Figure 32. Pore formation by NBD-labeled D4 mutants. Time-dependent emission intensity profiles for liposome-encapsulated $[Tb(DPA)_3]^{3-}$ (50 μM total lipid) when incubated with 50 nM of a NBD-labeled rPFO mutant (see key) at 37°C in buffer D containing 5 mM EDTA. The release of liposome-encapsulated $[Tb(DPA)_3]^{3-}$ was monitored as described in Experimental Procedures. For comparison, profile for rPFO is also shown.

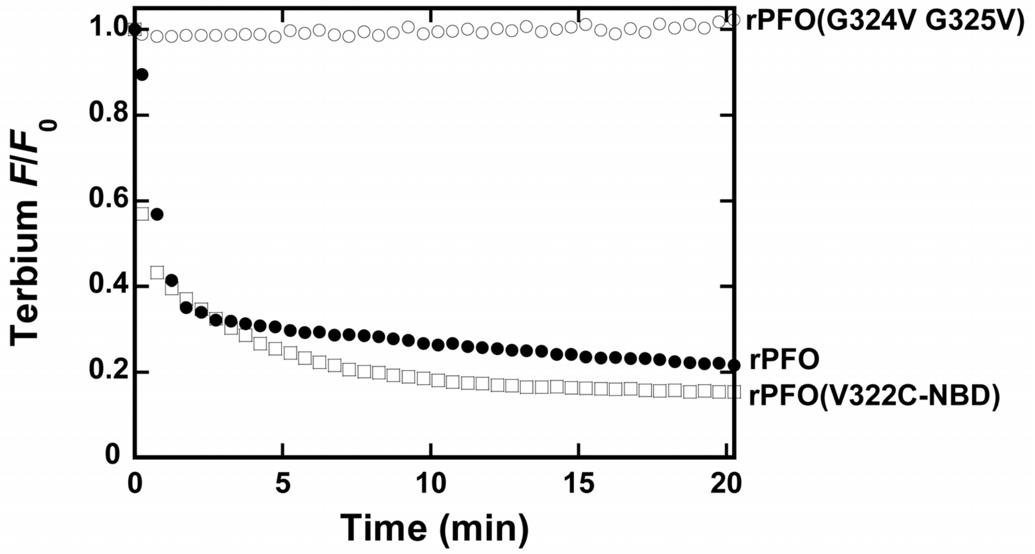

Figure 33. Pore-formation assay for rPFO(V322C-NBD) and rPFO(G324V G325V). Time-dependent emission intensity profiles for liposome-encapsulated $[Tb(DPA)_3]^{3-}$ (50 μM total lipid) when incubated with 50 nM of the indicated rPFO mutant at 37°C in buffer D containing 5 mM EDTA. The release of liposome-encapsulated $[Tb(DPA)_3]^{3-}$ was monitored as described in Experimental Procedures. For comparison, profile for rPFO is also shown.

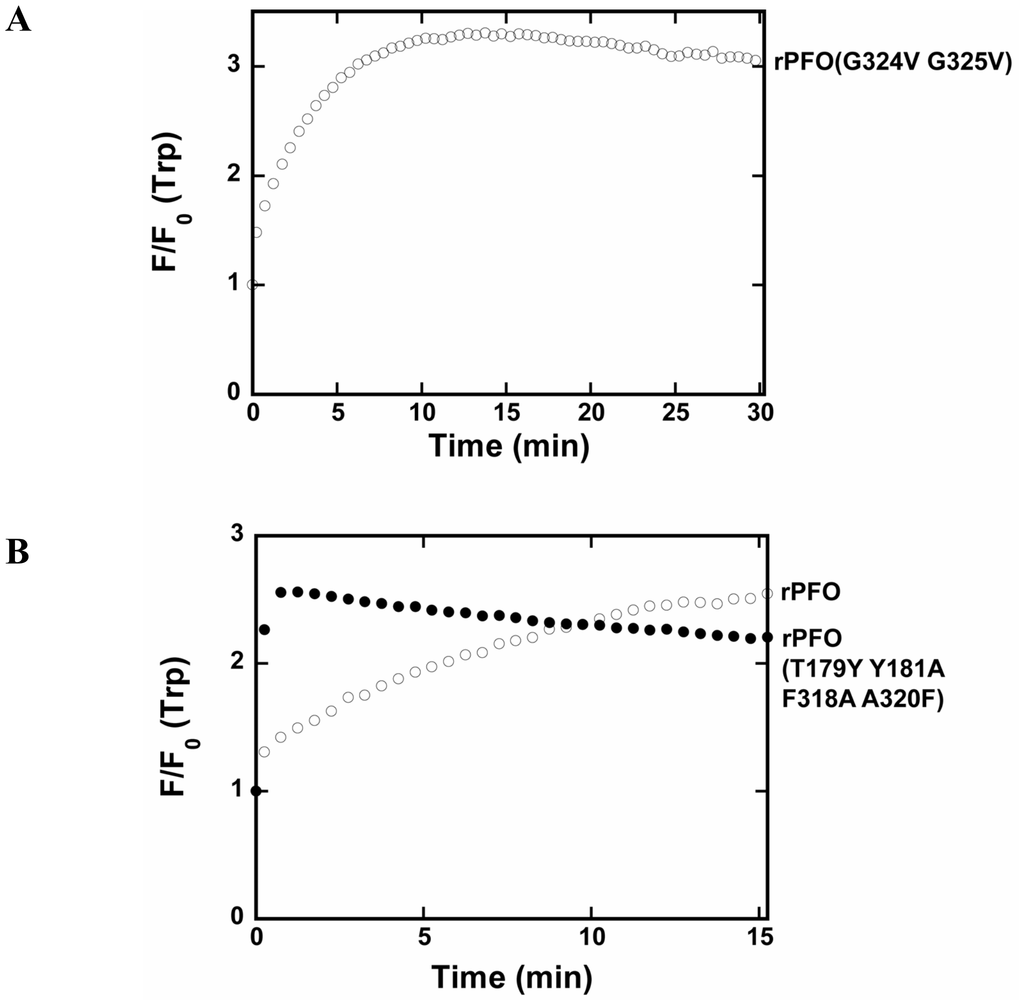

Figure 34. Trp emission intensity time traces for rPFO mutants. Time-dependent Trp emission intensity was measured after addition of cholesterol-containing liposomes (50 μM) to 50 nM of (A) rPFO(G324V G325V) or (B) rPFO(T179Y Y181A F318A A320F) (iv in Figure 24) as described in Experimental Procedures. For comparison, profile for rPFO is shown.

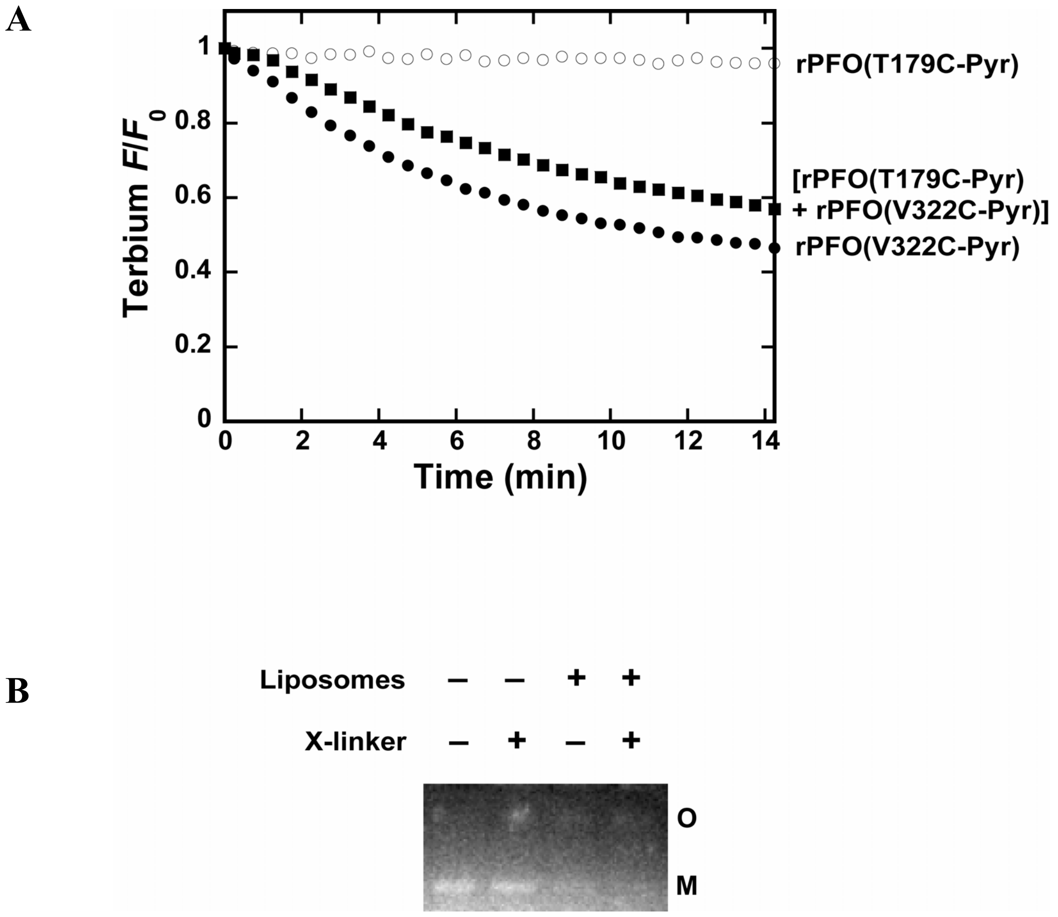

Figure 35. Characterization of pyrene-labeled rPFO mutants. (A) Time-dependent emission intensity profiles for liposome-encapsulated $[Tb(DPA)_3]^{3-}$ (50 μM total lipid) when incubated with an equimolar mixture of rPFO(T179C-Pyr) and rPFO(V322C-Pyr) (50 nM total), 50 nM rPFO(T179C-Pyr), and 50 nM rPFO(V322C-Pyr) at 37°C in buffer D containing 5 mM EDTA. The release of liposome-encapsulated $[Tb(DPA)_3]^{3-}$ was monitored as described in Experimental Procedures. (B) SDS-AGE analysis of an equimolar mixture of rPFO(T179C-Pyr) and rPFO (4.0 μM total) in the presence or absence of liposomes (1 mM total lipid) and in the presence or absence of the cross-linker glutaraldehyde as indicated. The bands were visualized by pyrene emission by exciting the gel on an UV transilluminator. M represents the monomer and O, the oligomer.

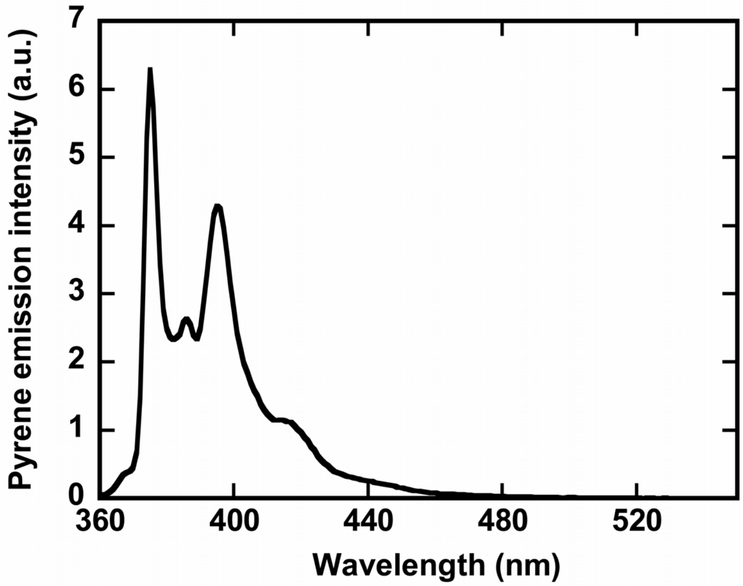

Figure 36. Pyrene-excimer formation is dependent on the proximity of pyrenes. Pyrene emission spectrum for an equimolar mixture of rPFO(Y181C-Pyr) and rPFO(V322C-Pyr) (100 nM total) in the presence of cholesterol-containing liposomes (100 μM lipid) was measured as described under Experimental procedures. Lack of excimer formation indicates that the pyrenes attached to these residues are not in close proximity to stack in the mixed PFO oligomer.

VITA

Name: Rajesh Ramachandran

Permanent Address: 173/3 Lake View Road,
West Mambalam,
Chennai – 600 033,
India

Education: B.S., Zoology (1996)
University of Madras
Chennai, India

M.S., Molecular Biology (1998)
University of Madras
Chennai, India

Ph.D., Biochemistry (2004)
Texas A&M University
College Station, Texas

E-mail: rajesh28@gmail.com